UNIVERSIDADE TÉCNICA DE LISBOA

INSTITUTO SUPERIOR TÉCNICO

Čerenkov Ring Acceptance in the RICH Detector of the AMS Experiment

Optimization of a Dual Radiator Configuration

Maria Luísa Ferreira da Gama Velho Arruda

(Licenciada)

Dissertação para obtenção do Grau de Mestre em Física

Orientador: Doutor Fernando José de Carvalho Barão

Constituição do Júri:

Presidente:

Doutor Mário João Martins Pimenta

Vogais:

Doutor Michel Buenerd

Doutora Ana Maria Vergueiro Monteiro Cidade Mourão

Doutor Fernando José de Carvalho Barão

Lisboa, Junho de 2003

"Study and in general the pursuit of truth and beauty,
is a sphere of activity in which we are permited to remain
children all of our lives."

Albert Einstein

Resumo

O Espectrómetro Magnético Alfa (AMS), a ser instalado na Estação Espacial Internacional (ISS) em 2006, visa medir os fluxos de elementos presentes nos raios cósmicos até ao Ferro, numa gama de rigidez de 1 GV a 1 TV, durante pelo menos três anos. Os seus objectivos são a procura de antimatéria cósmica, através da detecção de antinúcleos com $|Z| \geqslant 2$; a procura de matéria escura não bariónica e o estudo da origem e composição isotópica dos raios cósmicos. AMS é um espectrómetro de larga aceitância angular composto por diferentes subdetectores; em particular, haverá um detector de Čerenkov de imagem anelar de focagem aproximada (RICH). Este terá um radiador de composição mista, aerogel e um quadrado central de Fluoreto de Sódio, um espelho cónico lateral e um plano de detecção com 680 fotomultiplicadores e guias de luz. O detector RICH permite medir a carga eléctrica até ao Ferro e a velocidade das partículas que o atravessam, tendo esta última uma resolução de 0.1% para protões.

Quando uma partícula carregada atravessa um meio dieléctrico (o radiador), com uma velocidade superior à da luz naquele meio, ocorre emissão de fotões de Čerenkov. Estes são distribuídos numa superfície cónica com um certo semi-ângulo de abertura (ângulo de Čerenkov) que se relaciona com a velocidade da partícula que o gerou. O cone, ao atingir a base de fotomultiplicadores, define um anel com uma certa aceitância geométrica, sendo este usado para reconstruir o ângulo de Čerenkov e consequentemente a velocidade da partícula.

A implementação de uma configuração mista para o radiador, feita de Aerogel e Fluoreto de Sódio, por um lado aumenta a aceitância do RICH e por outro, alarga, diminuindo o limiar inferior, a região de momentos linear a que o detector é sensível. Desta forma aumenta-se o constrangimento dos modelos de propagação de raios cósmicos, baseados na medida das razões isotópicas ^{3}He/^{4}He e ^{10}Be/^{9}Be.

Palavras Chave: AMS, RICH, Ângulo/Anel/Padrão de Čerenkov, Aceitância do Anel de Čerenkov, Radiator Misto, Separação Isotópica de Massas

Abstract

The Alpha Magnetic Spectrometer (AMS) to be installed on the International Space Station (ISS), in 2006, will measure cosmic ray fluxes of elements up to Iron, in the rigidity range from 1 GV to 1 TV, for at least three years. Its aims are the search for cosmic antimatter, through the detection of antinuclei with $|Z| \geqslant 2$; the search of non-baryonic dark matter and the study of the origin and isotopic composition of cosmic rays. AMS is a large angular acceptance spectrometer composed of different subdetectors; in particular, there will be a proximity focusing Ring Imaging Čerenkov detector (RICH). This will be equipped with a mixed radiator of aerogel and a square of sodium fluoride in the center, a lateral conical mirror and a detection plane made of 680 photomultipliers and light guides. The RICH detector allows the measurement of particle electric charge, up to the iron, and velocity of the particle, the last one with a resolution of 0.1% for protons.

When a charged particle traverses a dielectric medium (radiator), with a speed greater than the speed of light in that medium, emission of Čerenkov photons occurs. These photons are distributed in a conical surface of a precise semi-aperture angle. This photon's angle (Čerenkov angle) is well related to the velocity of its mother's particle. The cone hits the photomultipliers basis and draws a ring with a certain geometrical acceptance. It is used to reconstruct the Čerenkov angle and therefore the particle velocity.

An implementation of a double radiator configuration, made of aerogel and sodium fluoride, on one hand allows to increase the RICH acceptance and on the other hand extends the linear momentum region covered by the detector to lower values. Therefore there are more constraints on the propagation models of cosmic rays, based on a measurement of the ratios ^{3}He/^{4}He and ^{10}Be/^{9}Be.

Keywords: AMS, RICH, Čerenkov Angle/Pattern/Ring, Čerenkov Ring Accep-

tance, Mixed Radiator, Isotopic Mass Separation

Acknowledgments

The work presented in this thesis corresponds a joint effort in the context of the participation of LIP (Laboratório de Instrumentção e Física Experimental de Partículas) in the AMS experiment. The contributions from many made its accomplishment possible. In some lines I would like to thank everyone involved in the development of this work, helping me in this enterprise.

Firstly, I would like to thank Professor Fernando Barão, my supervisor, for all the support and availability for all the fruitful discussions and for having introduced me to this challenging area: Astroparticle Physics.

A very special thanks to João for the daily brainstormings, for all the sincerely availability and friendship developed day by day.

Thanks to Patrícia for the knowledge and scientific attitude she transferred me in such an enthusiastic way. Thanks for all the good times after the most stressful tasks overcome.

I am very grateful to Professor Mário Pimenta for the all the suggestions, for the enthusiastic way he conducted all our discussions and encouraged me.

I also express my acknowledgments to Ana Keating for her co-operation at the the beginning always in an energetic way. Thanks to Fernando Carmo for the fruitful discussions on Physics, in general, for his friendship and thrilling interest in learning on this field. Thanks also to Pedro Silva for his availability for several fertile discussions.

I would like to thank Professor Ilda Perez from Faculty of Science whose work gave me the first boost in most of the calculations presented in this thesis.

I also thank Catarina, Gonçalo, Pedro and Andreia for the friendship and help offered to overcome technical questions. Thanks for the pleasant lunch times and refreshing coffee breaks. Thanks also to Laura for the friendship and good moments.

To Professor Luís Peralta, who still as my Professor at Faculty, strengthened my interest in this field and introduced me LIP as the good research institute it is.

I would like to express my extreme gratitude to my parents and grandparents for all the unconditional love, support and constant attention in all the steps of this new stage of my life. My sincere thanks to Ana, my beloved sister, for her company, interest showed and witty questions.

Thanks to Rui whose constant presence, love and tenderness, helped me to endure such a demanding task.

To my friends Paula, Sofia, Alberto and Bruno I would like to thank for the thrilling discussions on Physics and sincere friendship. Thanks also to Sónia for the friendship and contagious good mood.

Finally I express my recognition to all the people in LIP and people from the AMS collaboration that in any way contributed to the birth of this work, a very grateful experience. Thanks to LIP which embraced me in such a good way!

Contents

List of Figures

List of Tables

Introduction

In this thesis a method to calculate the geometrical acceptance of the Čerenkov photon pattern is presented, together with the application of this study to the optimization of a possible final setup for the **R**ing **I**maging **CH**erenkov (RICH) detector of the **A**lpha **M**agnetic **S**pectrometer (AMS) Experiment. The optimized radiator configuration for the RICH will allow to extend the detector capability of performing isotopic separation of ^{3}He/^{4}He and ^{10}Be/^{9}Be to lower values of energy from $\sim$0.5 GeV/nucleon up to $\sim$10 GeV/nucleon.

As the first magnetic spectrometer in space, AMS will collect information from cosmic sources emanating from stars and galaxies millions of light year away from the Milky Way. There was a precursor flight on board of the U.S. Space Shuttle Discovery, STS-91, in June 1998 for a 10 days period, at a mean altitude of 370 km, completing 152 orbits at $\pm 52^o$ of latitude, in order to test the design principles. Not only it was achieved but also about 100 million cosmic ray events were collected enabling precise measurements of the spectra of high energy protons, electrons, positrons and helium nuclei [1], [2]. This first stage of the experiment is known as AMS-01.

The Alpha Magnetic Spectrometer (AMS-02) will be installed, in 2006, for a period at least three years on the International Space Station (ISS), with the inclusion of new subdetectors and completion those of the experimental flight. The detector was designed and constructed by an international team of physicists and engineers from 37 universities and research institutes located in Switzerland, France, Russia, China, Taiwan, Italy, Germany, Spain, Portugal, Romania, Finland and the United States. There were technical challenges to build such a detector for use in space in accordance with strict space qualification standards and safety parameters requested by **N**ational **A**eronautics and **S**pace **A**dministration (NASA). Not only the interna-

tional support of the experiment but also the joint effort of the U.S. **D**epartment **o**f **E**nergy (DOE) and the NASA are making it become true.

Specifically, AMS has been designed to study the origin and structure of dark matter which is believed to constitute 70% of the Universe composed of matter; to probe the existence or absence of antimatter and to understand the overwhelming majority of matter over antimatter in the visible Universe through the detection of anti-carbon, anti-helium or heavier nuclei with a sensitivity $\sim 10^4$ better then the current experimental limits, for helium nuclei $\overline{\mathrm{He}}/\mathrm{He} < 10^{-9}$; and the origin and composition of cosmic rays. These characteristics overwhelm the capacity of previous stratospheric balloon experiments which have been limited by their short duration, resulting in low statistics, and affected by the absorption power of Earth's atmosphere.

AMS is also intended to study other issues in astrophysics with high statistics data. Cosmic rays are energetic particles that constantly reach the Earth. They have been studied by a wide number of ground based and subatmospheric experiments. AMS, contrarily to those, will be able to detect the original cosmic rays in space before they collide with the Earth's atmosphere. AMS will also be able to detect cosmic rays with kinetic energies in the range ∼0.3-0.5 GeV to ∼1 TeV.

It is believed that cosmic ray particles from beyond our local galactic cluster are only 1 in 10 billion particles that reach our atmosphere. A technique believed to provide the correct fraction of cosmic rays originated outside our local galactic cluster is to measure the ratio of two cosmic particles, $^{10}\mathrm{Be}/^{9}\mathrm{Be}$. Since ^{10}Be has a half life $\sim 1.5 \times 10^6$ [3], it can be used as a galactic chronometer. A high ratio will confirm that the majority of the cosmic rays are relatively young in astronomical terms, which means less than a million years old. Contrarily a low ratio would point to a majority of ^{10}Be already decayed due to having been traveled a longer distance inside the galaxy. The measurements performed by AMS will enable an accurate determination of the cosmic ray confinement time in the galaxy and an evaluation of the mean density of interstellar material (ISM) traversed by cosmic rays. The measurement of the momentum dependence of the $^{10}\mathrm{Be}/^{9}\mathrm{Be}$ ratio will provide a determination of important transport parameters and galactic variables present in different models of cosmic rays propagation, for instance: the mean interstellar

matter density in the Leaky Box model [4] or size of the confinement halo in the diffusion model [4]. The propagation history of helium can be probed by measuring the isotopic ratio ^{3}He/^{4}He. ^{3}He is essentially secondary coming from the spallation of ^{4}He, it also contributes to the determination of the mean density of interstellar material crossed, indicating the amount of time cosmic rays spend in the halo of the galaxy [4].

This thesis is organised in six chapters. In the first, there are exposed some topics in cosmic rays physics: present knowledge about their origin, acceleration mechanisms and propagation. Some considerations on their use as cosmic clocks are also described. The matter-antimatter problem with its theoretical and experimental features is established, with an emphasis on the observational part: its manifestations, difficulties in detection and the recent experimental efforts, in particular AMS-01 results. The dark matter problem is also approached.

The next chapter is dedicated to a description of the AMS-02 detector, where each subdetector is introduced. Here the aims of AMS experiment are exposed.

The third chapter starts with some brief considerations on the Čerenkov radiation, then the RICH detector, the detector in this current study, is introduced. A prototype of the RICH detector is also described. The method used to reconstruct the Čerenkov angle, developed by J. Borges [5] is explained.

In Chapter 4, a thorough description of the photon pattern tracing is presented, including the results of its application to velocity reconstruction [5], and charge reconstruction [6], among other goals.

Chapter 5 focuses on a dual radiator configuration study. First a complete characterization of both radiators is done in a comparative frame. A solution is introduced for the final setup and the expected reconstruction efficiency is shown.

An applied study of isotopic masses separation for ^{3}He/^{4}He and ^{10}Be/^{9}Be is developed in the sixth chapter. First the simulation conditions are described, as well as the fit method used for the mass distributions. The influence of the presence of a plastic foil, at the basis of the radiator in mass reconstruction, is probed. Finally the reconstructed isotopic ratios, according to the models introduced in the simulation, are presented.

Chapter 1

Cosmic Rays

Cosmic ray particles hit the Earth's atmosphere at the rate of about 1000 $m^{-2}s^{-1}$ [7]. The cosmic rays are ionized nuclei, ranging from a single proton up to an iron nucleus and beyond, distinguished by their high energies. There are also electrons and a detectable flux of energetic photons and neutrinos is present. The measured cosmic ray energy spectrum (1.1) has an approximately power law of the from

$$\frac{dN}{dE} \sim E^{-\gamma} \tag{1.1}$$

being γ the spectral index, and extends up to $\sim 3 \times 10^{20}\,\mathrm{eV}$.

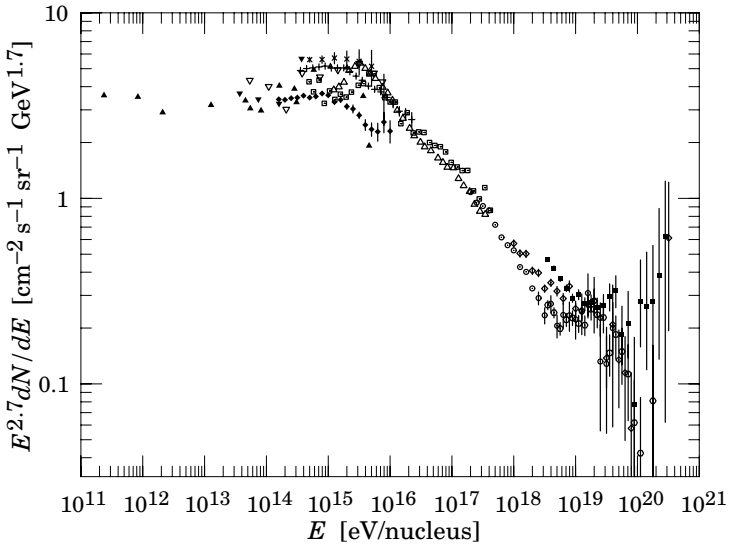

Figure 1.1: *The spectrum of cosmic radiation from* $10^{11} - 10^{20}$ *eV* [8].

Up to values around 10^{15} eV (1 PeV), $\gamma \simeq 2.7$. From here on the spectrum becomes steeper with $\gamma \simeq 3$ ('knee'), which could point to a different origin for the two regions. From around 10^{18} eV the spectrum becomes less steep again ('ankle'). The behaviour at 10^{20} eV has been an important issue. The questions are: if an energy maximum has been reached at 5×10^{19} eV because of the interaction of cosmic rays with the cosmic background radiation (Greisen-Zatsepin-Kuzmin cut-off), or if a plateau is forming, or whether the flux simply becomes too small to be reliably measured. The observation of events at energies higher than 10^{20} eV has given rise to speculative ideas about their origin [9].

The changes in the spectral index reflects the different origin and the propagation history of cosmic rays with different energy: below the 'knee' their curvature radius is smaller than the galactic disk thickness, hence their sources must belong to our Galaxy. Above the 'knee' the curvature radius becomes greater than the disk thickness, and Cosmic Rays (CR) may escape into the galactic halo.

The discovery of cosmic rays is due to V. Hess, in 1912, through a series of pioneering balloon-flights up to altitudes of 5-9 Km. Since then, a lot of detailed information on their arrival direction, energy spectrum, elemental and isotopic composition, at different energies, has been collected by direct measurements on balloons, satellites and indirect ground-based measurements like air shower detectors.

Cosmic Rays are divided in three different categories: Galactic Cosmic Rays (GCR), Solar Cosmic Rays (SCR) and Anomalous Cosmic Rays (ACR).

Galactic Cosmic Rays are originated and accelerated outside our solar system, composed of 90% protons, 9% α particles, 1% electrons and heavier nuclei fully ionized, as well as, antiprotons and positrons essentially produced in secondary reactions. GCR are the most typical cosmic rays.

Solar Cosmic Rays or Solar Energetic Particles (SEP) have their origin in the Sun mostly from solar flares, coronal mass ejections and shocks in the interplanetary medium. They are mostly protons and have energies up to several hundred MeV/nucleon.

Anomalous cosmic rays [10] are mainly singly charged low energy particles ($<$100 MeV/nucleon) resulting from interstellar neutral particles that are ionized when they penetrate the heliosphere and are carried by the solar wind: by pho-

toionization by solar UV photons or by charge-exchange collisions with solar wind protons. The composition of ACR is much different from GCR and SCR. They have more helium than protons and much more oxygen than carbon. This unusual composition reflects the fact that only atoms with high first-ionization potentials (above 13.6 eV) are abundant as interstellar neutrals. These cosmic rays are below the detection range of AMS. AMS will detect cosmic rays in the energy range above few hundred MeV and below few TeV and these cosmic rays particles are thought to be originated by galactic sources.

However, the two fundamental questions of cosmic ray physics are: "Where do they come from?" and "How are they accelerated to such high energies?".

1.1 Origin and Acceleration of Cosmic Rays

1.1.1 Stellar nucleosynthesis

Primordial nucleosynthesis is able to explain the formation of light elements up to ^{7}Li in the early Universe, but it doesn't explain the existence of heavier elements in nature. These are supposed to be produced in the stellar nuclear reactions at different stages of their lives. The condensation of interstellar gas, specially hydrogen and helium gives birth to a star. This gas is heated up by the conversion of gravitational energy to thermal energy starting the reaction when the temperature and pressure in its center are sufficiently high. As long as hydrogen is available, thermal pressure and gravitational force are in equilibrium, stabilizing the star to a particular temperature. In the first step, when the star is essentially composed of hydrogen, the reactions in question are the $p-p$ reactions, which are established in Table 1.1 [11]. The fusion of hydrogen into helium fuels the enourmous amount of energy dissipated by stars in form of radiation for the greatest part of their life. The first step in each chain is a weak process so the stars consume the protons very slowly and thus continue to exist today. Here four protons are converted into a helium nucleus.

CHAIN I	CHAIN II	CHAIN III
$p(p, e^+\nu)$D	$p(p, e^+\nu)$D	$p(p, e^+\nu)$D
D(p, γ) ^{3}He	D(p, γ) ^{3}He	D(p, γ) ^{3}He
^{3}He$(^3$He$, 2p)$ ^{4}He	^{3}He(α, γ) ^{7}Be	^{3}He(α, γ) ^{7}Be
	^{7}Be(e^-, ν) ^{7}Li	^{7}Be(p, γ) ^{8}B
	^{7}Li(p, α) ^{4}He	^{8}B$(, e^+\nu)$ ^{8}Be*
		^{8}Be$^*(, \alpha)$ ^{4}He

Table 1.1: *The three possible nuclear reaction chains which produce helium nuclei using four protons.*

After the running out of hydrogen the star contracts further until the temperature and pressure become sufficient to ignite the next element, the helium. This happens for stars with $M > M_\odot$ which provides a high enough temperature. Now the star's core is very dense and so the short-lived product of the reaction $\alpha + \alpha \rightarrow ^8$Be, with $\tau(\ ^8\text{Be}) \sim 10^{-16}$ s, can originate ^{12}C. This reaction is the triple-α process and bridges the gap towards the production of heavier nuclei which was not produced during primordial nucleosynthesis. By additional α capture, nuclei like ^{16}O, ^{16}O, ^{24}Mg, ^{28}Si can be created with rates of production limited by the available equilibrium conditions of pressure and temperature.

Capture of α particles may form nuclei with a even number of neutrons and protons, up to ^{40}Ca, known as the α *process*.

At very high temperatures, around 5×10^9 K, typically found in the supernovae stage of a massive star, all types of nuclear reactions can occur. The system should be treated statistically. The abundances of nuclei in the range $50 \leq A \leq 62$, peaking at ^{56}Fe, the most tightly bound, are well explained with this *e process*.

The *s process* is a slow process (compared with β decay lifetime) occurring in thermal equilibrium. This is a process where nuclei with $23 \leq$ A ≤ 46 and $63 \leq$ A ≤ 209 are produced by neutron capture. It explains the characteristic peak structure observed in the abundance of isotopes. The additional neutrons are available from prior (α,n) processes on ^{13}C and ^{22}Ne [9].

A second set of peaks, shifted to more neutron-rich isotopes, suggests the existence of a second important process, the *r process*, a rapid process, where more

neutron-rich nuclei are produced because a huge flux of neutrons is available. This is usually associated to a supernovae explosion, where all the elements are synthesized in a very short time. Light isotopes, like D, Li, Be and B are generated by proton capture at low temperatures in stars. D, ^{3}He,^{4}He and some ^{7}Li are produced during primordial nucleosynthesis.

The L elements: ^{7}Li, Be and B are produced by the called *x process*. These elements are destroyed in the interior of star at temperatures ranging from 2 to 5×10^6 K, with the exception of ^{7}Li.

The variety of isotopes that are synthesized during the different star stages is supposed to be injected into interstellar space through supernovae explosions. The onion-like structure of a supernovae allows the different processes explained above to be started in different shells. Further enrichment of interstellar matter can come from emission of stellar atmospheres or red giants.

1.1.2 The light elements Li-Be-B

Lithium, beryllium and boron are known as the L elements or group LiBeB. It is evident from first observation of Figure 1.2 that galactic cosmic rays are exceptionally rich in these L elements with a ratio LiBeB/CNO ~ 0.25 compared to the local solar system matter (LiBeB/CNO $\sim 10^{-6}$).

The L elements are believed to be produced by a non-thermal mechanism: calculations based on spallation processes of energetic light galactic cosmic rays (p and α) breaking up C, N, O and heavier nuclei in the interstellar medium (ISM) reproduce the general isotopic abundances of Li, Be, B. Spectroscopic analysis and meteoric material point to further processes involved. The "LiBeB-problem" consists in the fact that it is observed a linear correlation between the abundances of LiBeB and the metalicity in metal poor halo stars. However if the spallation rates are proportional to the Interstellar Abundances of C, N, O and if the main energy source of the energetic particles is provided by supernovae explosions, a quadratic correlation is expected. The fact that L elements might be produced via fragmentation of C and O nuclei when they collide with interstellar hydrogen and helium is a possible solution.

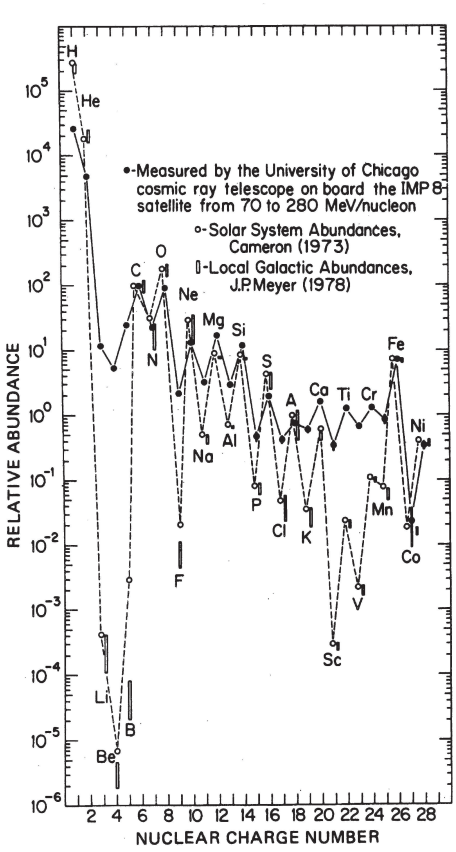

Figure 1.2: *The cosmic ray elemental abundance (H-Ni) measured on board of the cosmic-ray satellite (closed circles) compared to the solar system abundances (open circles) and to the local Galactic abundances (open boxes), all relative to carbon* [12].

1.1.3 Cosmic ray sources and acceleration mechanisms

The principal sources of cosmic rays in the Galaxy are supernovae and supernovae remnants, pulsars, compact accreting systems, stars and stellar winds. It is commonly assumed that cosmic rays with the highest detected energies, E $>10^{19}$ eV, have an extragalactic origin. They might be generated in active galactic nuclei, relativistic jets, interacting galaxies, or result from the decays of hypothetical topological defects [13].

Concerning the acceleration, the main question here is whether the major acceleration processes occur on large scales in the Galaxy or near certain point sources. On the small scale of the Solar System it is known that both happen. Spacecraft experiments have detected evidence of particle acceleration to supra thermal energies of KeV to MeV by interplanetary shock waves, for example at the Earth's bow shock and with solar wind shocks. In solar flares particles are also accelerated to GeV.

For GCR, the only way to trace the cosmic rays is to look for stable, neutral secondaries resulting from the collisions of the accelerated charged particles. Those collisions can occur either in the interstellar gas or in the vicinity of the sources. The charged particles don't point back to their sources because of their diffusion in the Galactic magnetic fields. Consequently the spectrum is perfectly isotropic, except the slight anisotropies observed for the ultra-high energy (UHE) cosmic rays.

Concerning the energy, supernovae with its remnants, which may include neutron stars, are the most probable cosmic ray sources in the Galaxy [14]. The total power of galactic cosmic ray sources necessary to maintain the observed cosmic ray density is estimated as $L_{cr} = 5 \times 10^{40}$ erg/s that implies the release of energy in the form of cosmic rays of approximately 5×10^{49} erg per supernovae if the supernovae rate in the Galaxy is 1 every 30 years [13]. This value comes to about 5% of the kinetic energy of the ejects which is according to the prediction of the theory of diffusive shock acceleration for supernovae [15].

This is the most generally accepted process for the investigations of cosmic ray acceleration in the Galaxy. In this, particles are accelerated while they repeatedly interact with the strong shock formed at the supernovae remnant shells as they sweep through the ISM. A particularly attractive feature of supernovae shock acceleration

is that the power spectrum, as it is observed, can be explained up to energies of 10^{15} eV. The rotational energy of a young pulsar with period T seconds, which remains after the supernovae, is estimated to be 2×10^{46} T^{-2} erg and may also provide another energy reservoir for particle acceleration.

1.2 Propagation Models

The propagation of Cosmic Rays in the Galaxy can be basically described by two different models: the "Leaky Box Model" and the "Flat Halo Model". Both establish a certain source distribution and boundary conditions for all cosmic rays species. Although each have simple geometry, they reflect the most essential features of the real system uncertainties in the measured fluxes and the relevant nuclear cross sections do not permit to determine which model is to be preferred.

1.2.1 "Flat Halo" model

The Flat Halo model [4] assumes that the propagation of cosmic rays is closely related to the structure of our Galaxy. A possible model will be briefly established. Our Galaxy can be described as a flat disk with radius r=15 kpc and height H=200 pc, with a mean density of 1 hydrogen atom per cm^3. The solar system rotates around the dense center at a distance d=8.5 kpc. Optical observations of nearby galaxies point to the existence of a gaseous halo with lower density (about 10^{-2} the Galactic density) extending several kpc away from the Galactic plane. The Galactic magnetic field is within the range 1-3 μG, which implies that cosmic rays in the GeV region closely follow the field lines. The configuration of the magnetic field is barely known. In the solar surroundings the field lines tend to be parallel to the galactic plane with great scale fluctuations and also with small regions with highly nonuniform orientations [11].

The cosmic-ray sources are distributed within an inner disk with the characteristic thickness of $2h(\sim 300)$ pc. The diffusion of cosmic rays averaged over the scale of few hundred parsec is isotropic. The particles escape freely through the halo boundaries into intergalactic space where the density of cosmic rays is negligible. Consequently, the *Flat Halo* model assume a gradient in the density of cosmic rays

with a maximum value in the Galactic Disk decreasing as a function of distance from the Galactic plane; the escape of particles from the halo to the intergalactic space is done by diffusion and the equation of transport comes:

$$\frac{\partial N_i}{\partial t} - \vec{\nabla} \cdot (D\vec{\nabla} N_i - \vec{u} N_i) + \frac{\partial}{\partial E}(b(E) N_i) + \frac{N_i}{\tau_{int}(i)} + \frac{N_i}{\tau_{dec}(i)} - \sum_{j>i} \frac{P_{ji}}{\tau(j)} N_j - \sum \frac{N_j}{\tau_{ij}} = Q_i(\vec{r}, E, t) \quad (1.2)$$

where $N_i \equiv N_i(\vec{r}, E, t)$ is the density of element nuclei i with energy E, at a point $\vec{r}$ and time t, D is the diffusion coefficient, $\vec{u}$ is the velocity of convective particle transport in the Galaxy by the hypothetical galactic wind; $b(E) \equiv dE/dt$ is the energy loss rate; τ_{int} is the mean time of interaction of the nuclei; τ_{dec} is the mean time of decay of the same nuclei; $\sum_{j>i} \frac{P_{ji}}{\tau(j)} N_j$ is the nuclear spallation term; $\sum \frac{N_j}{\tau_{ij}}$ describes the appearance of nuclei i due to decays of other nuclei, $Q_i(\vec{r}, E, t)$ is the density of sources of the particles per unit interval of energy.

The analytical and numerical solutions for this model show that in the first approximation the cosmic ray propagation for not very heavy stable primary and secondary nuclei is characterized by only one main parameter, the escape length, X_e g/cm^2 [16]. For an observer in the Galactic disk the relation between the parameters of diffusion model and the escape length is $X_e = \mu v H/(2D)$, where μ is the surface gas density of the Galactic disk ($\mu = 2.4$ mg/cm^2, at the Sun location in the Galaxy), v the particle velocity, H the scale height of the cosmic-ray halo, and D the cosmic-ray diffusion coefficient. The previous expression for the escape length is valid for nuclei with the total spallation cross sections $\sigma \ll (mH)/(X_e h_g)$ where m is the average mass of an atom in the interstellar gas, h_g is the characteristic height of the gas distribution above the Galactic plane. The path length distribution (PLD) in this case is approximated by the exponential form $G = exp(-x/X_e)$ with the mean matter thickness, X_e. This is a probability distribution for particles observed at energy E to have passed through an amount of material x.

1.2.2 "Leaky Box" model

In this model [4], the cosmic rays are assumed to propagate freely in a containment volume: the halo or the disk of the Galaxy. At each edge of the volume they have

a constant and energy independent probability of escaping into extragalactic space. The density is assumed to be constant throughout the volume of confinement and the cosmic rays are isotropically and homogeneously distributed inside. Consequently the gradient term in the density of cosmic rays and diffusion disappear, and appears a substitute term τ_{esc} which is the mean escape time from the Galaxy. The equation comes:

$$\frac{\partial N_i}{\partial t} + \frac{\partial}{\partial E}(b(E)N_i) + \frac{N_i}{\tau_{esc}(i)} + \frac{N_i}{\tau_{int}(i)} + \frac{N_i}{\tau_{dec}(i)} - \sum_{j>i} \frac{P_{ji}}{\tau(j)} N_j - \sum \frac{N_j}{\tau_{ij}} = Q_i(\vec{r}, E, t) \quad (1.3)$$

1.3 Cosmic Ray Clocks

After leaving the sources and propagating in the interstellar medium, primary relativistic nuclei experience fragmentation in interstellar gas and give rise to secondary nuclei in cosmic rays. The composition of these stable radioactive secondary isotopes reflects the conditions of cosmic-ray propagation in the Galaxy [17].

This study allows to determine the ratio H/D [13]. The incorporation of radioactive secondaries helps to find the diffusion coefficient, D and the cosmic halo size, H separately. For this study are used radioactive isotopes with a decay lifetime that is comparable to the age of cosmic rays in the Galaxy. The isotope ^{10}Be (with a decay lifetime at rest 1.6×10^6 yr) is most commonly used. Other isotopes are ^{26}Al (1.3×10^6 yr), ^{36}Cl (4.3×10^5 yr), ^{54}Mn ($6\times \sim 10^6$ yr) and ^{14}C (8.2×10^3 yr).

The interpretation of the measurements depends on the model of propagation considered. Using the Leaky Box model or the Flat Halo model is quite different for decay times $< \mathrm{H}^2/\mathrm{D}$. Having a characteristic decay time $\tau \sim 1$ Myr these isotopes may diffuse to the observer from distances not larger than $(\mathrm{D}\tau)^{1/2} \sim 300$ pc.

Knowing the number density of primary nuclei from the ground-based observation, the cross section of production from the experiments performed at laboratory, and the gas distribution from the astronomical observations, it is straightforward to calculate the production rate of the secondaries. The observed abundance allows to calculate the diffusion coefficient [17]. At energy E= 400 MeV/nucleon, in the interstellar space, are achieved the values D=(2-5)$\times 10^{28}$ cm^2/s and the size of cos-

mic ray halo H$\sim$ 4 kpc. The typical time of cosmic ray diffusion from the Galaxy is $H^2/2D \sim 7 \times 10^7$ yr.

1.4 Solar Modulation

The continuous expansion of the solar corona produces drift of the interstellar plasma with a velocity around 300 Km/s which conducts 10 protons per cm^3 to the terrestrial orbit. This is the solar wind which transports the lines of the solar magnetic field producing the interplanetary magnetic field. Due to the solar rotation, with a period of 27 days, the strength lines get a spiral form with the radial direction and making 45^o with the terrestrial orbit. At distances from the sun greater than the astronomical unit, the field becomes more disordered due to the thermal anisotropy of the medium and due to irregular expansions of the solar corona.

The terrestrial magnetic field offers a barrier to the solar wind, see Figure 1.3.

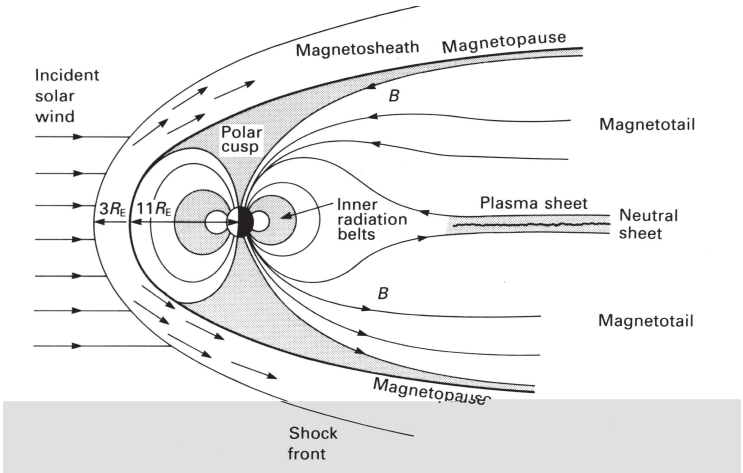

Figure 1.3: *The interaction of the solar wind with the Earth's magnetosphere* [18].

In 1967 Glesson and Axford [19] proved that the influence of the solar flux in the cosmic rays could be parametrized with only one parameter: the modulated flux of a particle with energy E_k is obtained considering the interstellar flux of cosmic rays with energy E_k, plus the energy lost when they reach the Earth ($Ze\Phi$), multiplied by a factor less than 1, which only depends on the initial energy $E_k + Ze\Phi$ and the

final E_k. The parameter Φ only depends on the solar activity and has the dimension of a potential (usually measured in MV):

$$\phi(E_k) = \frac{E_k^2 + 2mE_k}{(E_k + Ze\Phi)^2 + 2m(E_k + Ze\Phi)}\phi(E_k + Ze\Phi) \tag{1.4}$$

where Φ ranges from 350 MV up to 1500 MV in the maximum of solar activity. So the flux is maximal when the solar activity is minimal. The Φ value predicted for the second part of AMS experiment is around 1000 MV.

1.5 The Geomagnetic Field and Geomagnetic cut-off

The magnetic field of Earth can be approximated by a dipole, whose orientation and strength are chosen in agreement with experimental data. A more detailed model is given by the International Geomagnetic Reference Field (IGRF) [20].

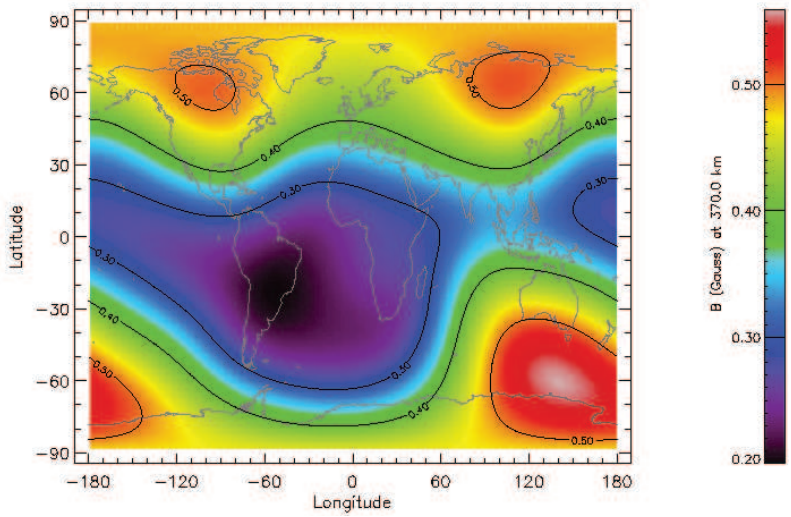

Figure 1.4: *Isointensity of geomagnetic field lines (in Gauss units) at an altitude of 370 Km* [20].

The geomagnetic latitude (λ) is the angle measured from the geomagnetic equator, defined as the plane normal to the dipole axis, to the point considered and containing the Earth's center. Figure 1.4 shows the geomagnetic field at an Earth altitude of 370 Km, the altitude of the first AMS flight (AMS-01) and the mean

altitude of the ISS. The region close to the South America where the magnetic field sinks is known as the South Atlantic anomaly. Here, high fluxes of low energy particles are observed.

The geomagnetic cut-off is the minimal rigidity a charged cosmic ray should have to reach a point located at an altitude h above the surface and at the geomagnetic latitude λ. This cut-off will also depend on the polar angle θ between the direction of arrival of the particle and the tangent to circle of latitude. It is given by the following expression:

$$R_{cut} = \frac{60}{\left(1 + \frac{h}{R_E}\right)^2} \frac{\cos^4 \lambda}{\left[(1 + \cos\theta \cos^3 \lambda)^{1/2} + 1\right]^2} \; [GV] \tag{1.5}$$

where R_E is the Earth radius.

Another side effect of the geomagnetic field is the existence of charged particles trapped in the field. These particles follow a spiral motion along the field lines, bouncing between two mirror points and drifting east-west (see Figure 1.5). Positive particles will drift to West and negative to East.

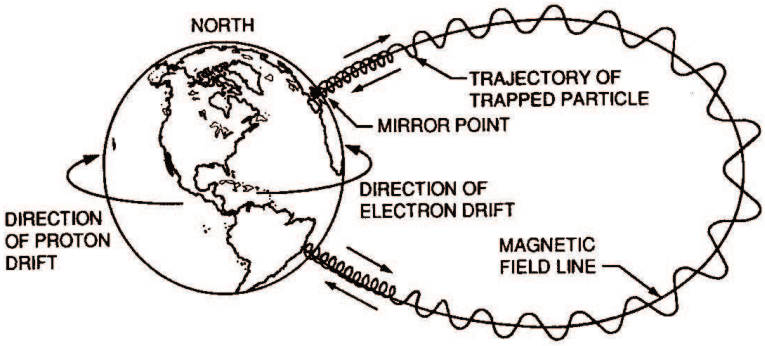

Figure 1.5: *Particle motion in geomagnetic field* [21].

1.6 Cosmic Rays near Earth

The elemental composition of Cosmic Rays can be measured at energies ranging from MeV to TeV and is similar in good approach to the solar system values (see Figure 1.2). This points to a similarity in the production processes, i.e. both of stellar nature (see Subsection 1.1.1).

There is a pronounced odd-Z vs even-Z variation in the abundance and there is an abundance peak at iron for both.

Nevertheless, differences are observed, especially for the most abundant nuclei: H and He, which are relatively less abundant in Cosmic Rays. This is either due to their ionization potential and consequently to the greater difficulty in accelerating those particles or due to a different birth mechanism. The spallation products of C and O (Li,Be,B) and those of Fe (Sc, Ti, V, Cr, Mn) are more abundant in cosmic rays since they are not produced in stellar nucleosynthesis. An estimate of the amount of matter traversed, based on ratios of secondary spallative products gives a value ranging from 5 to 10 g/cm^2 between the injection and the observation. Being the average density in the Galaxy of 1 proton/cm^3, the amount of matter traversed comes several times the thickness of the Galaxy which proves that the propagation is by diffusion [7].

1.7 Antimatter

1.7.1 Antimatter in astroparticle physics

Proving that exists antimatter in cosmic rays is part of a wider problem of the matter-antimatter symmetry of the Universe. This issue and more generally the antimatter problem in space has become apparent after Dirac (1928) has predicted the existence of positron, and Anderson has experimentally confirmed it. In fact, Dirac put forward the idea of the matter-antimatter symmetric universe, the existence of anti-stars made of antiprotons and positrons.

The Big-Bang model assumes that at the first instants of creation, half of the Universe was made out of antimatter. The validity of this model is based on three main experimental observations: the recession of galaxies (Hubble expansion), the highly isotropic **C**osmic **M**icrowave **B**ackground (CMB) and the relative abundance of light isotopes. However, the presence of cosmological antimatter somewhere is missing.

Particle-antiparticle symmetry means that not only parity (P) and electric charge (C) are conserved but also the baryon number, B, which distinguishes baryons (e.g. protons and neutrons) from leptons (e.g. electrons, μ -mesons and neutrinos), and

the lepton number, L, which is a principal lepton characteristic. This means that particles are always produced in pairs of particle and anti-particle, being produced from neutral states (B=0, C=0, L=0). According to the Big-Bang theory an equal number of particles and antiparticles should be produced in the Universe. However, no trace of antimatter has been observed so far. How did particle-antiparticle symmetric interactions end up in the strongly asymmetric Universe known today? There are three main directions which intend to provide an answer:

(a) *Observations:* Cosmic rays are the most promising objects for the antimatter search: antimatter may manifest through annihilation products which would contribute to the diffused γ-ray spectrum.

(b)*A Symmetric Universe*: Theorists have come up with the idea that matter and antimatter have been separated at an early stage of the Universe and formed domains out of either one of them. However, observations don't support this and more complicated and consequently less elegant, symmetric Universe models are introduced. In fact, if the current theoretical estimates of the expected diffuse γ-ray (CDG) spectrum are not incorrect by an order of magnitude, the model of a baryon symmetric Universe is neither in agreement with the observed uniformity of the CMB nor with the measured diffuse γ-ray spectrum [22].

(c) *Theory-antimatter-free Universe :* An initially symmetric Universe evolved dynamically to a completely asymmetric one where all the antimatter disappeared by some 'annihilation catastrophe', which was inevitable when the Universe cooled down. The barions that had survived formed the Universe as it is known. This is called Baryogenesis. This is the most reliable theory until now, despite the absence of an explanation for the way the baryon asymmetry had survived within the inflation scenario, and for complications like *preheating* and *reheating* after the inflation.

1.7.2 Experimental search for antimatter

Direct Antimatter Search: observation of antinuclei in cosmic rays.

Antimatter does not exist on Earth in macroscopic amounts, otherwise it would

have been annihilated releasing tremendous amounts of energy. The constant flux of charged particles emitted by the Sun and propagated throughout the Solar System (the Solar wind) allows to exclude antimatter planets since they would constantly emit very bright γ-rays. Photons emitted by other stars don't probe directly the sign of the baryon number of the object from where they are emitted. Fortunately cosmic rays do!

Some distant antimatter objects (anti-stars, anti-galaxies) would provide space with cosmic antimatter particles, primarily antiprotons and positrons but also antinuclei. The antimatter particles would diffuse through space and eventually reach the vicinity of the Earth.

Positrons and antiprotons are measured in cosmic rays , but they do not provide an evidence for such existence of antimatter in the Universe. The measured flux is compatible with secondary production. Antiprotons can be produced in interactions of primary cosmic rays protons with the Interstellar Medium by the reaction:

$$p + p \rightarrow p + p + p + \bar{p}. \tag{1.6}$$

The energy spectrum of these secondary $\bar{p}$s should have a peak around 2 GeV, with a sharp decrease of the flux below and above the peak, as consequence of the reaction kinematics, which is visible in Figure 1.6. Further measurements reported a $\bar{p}/p$ flux above the expected for a purely secondary process (see [23], [24]). Different explanations are considered:

- antimatter reaching the Galaxy from antimatter galaxies in a baryon-antibaryon symmetric Universe [25], [26];
- production by dark matter particle annihilation (see eq. 1.7);
- production by primordial black holes evaporation [27].

A lot of experiments were done in the energy range 100 MeV to 10 GeV which show a good agreement in the peak. The discrepancy observed at low energy can not be related with primordial antimatter because of the solar modulation effect which shifts the energy spectrum towards lower energy values. So the present data is not clear to search primordial antimatter in the Universe.

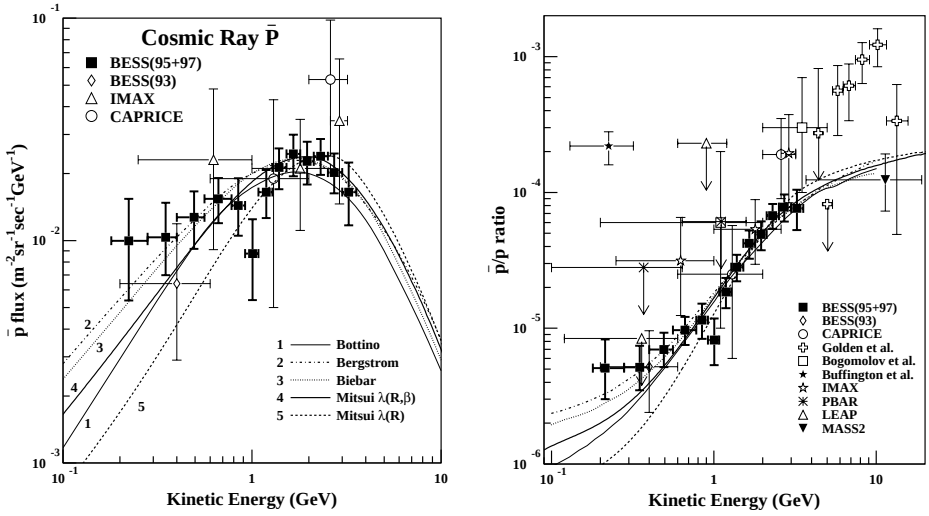

Figure 1.6: *Cosmic rays $\bar{p}$ flux in the energy spectrum from 0.1 GeV to 10 GeV, different models and the flux measurements by different balloon experiments* (left). *$\bar{p}/p$ ratio for the same energies as expected by different models and with the corresponding measurements by different experiments* (right) [28].

A few years ago, the BESS ballon experiment detected antiprotons at low energies below 1 GeV [29]. The size of the signal was slightly above the expected calculations available at the time, from the interaction of cosmic rays with interstellar gas. Bergström, Edsjö and Ullio [30], [31], and Bieber et al [32] in 1999, have evaluated the effect of helium interactions, as well as collective nuclear effects and proton and antiproton secondary interactions. The consequences were an increase of the expectations of antiprotons in the energy range below 1 GeV, with the main uncertainty coming from the parametrization of the primary proton spectrum. In parallel, the BESS experiment also improved its measurements, and the measured antiproton yields are now smaller. With those developments, there is today no indication for new physics in the antiproton signal.

Other experiments have been carried out on balloons or satellites for direct search of antinuclei in cosmic rays. The most promising is antihelium, once it is expected to be the most abundant antinuclei. It would constitute an evidence for cosmologically significant amounts of antimatter. Heavier antinuclei, like $\bar{C}$, would have even more profound consequences because it points to an antinucleosynthesis and consequently

to the existence of antistars which burned antihelium.

Indirect Antimatter Search:

It can be performed by observation of the γ-ray spectrum. Hadronic matter and antimatter when interact, annihilate mainly by the processes:

$$N + \bar{N} \rightarrow \begin{cases} \pi^0 \rightarrow \gamma + \gamma \\ \pi^{\pm} \rightarrow \mu^{\pm} + \upsilon_{\mu}(\bar{\upsilon_{\mu}}) \end{cases} \quad \mu^{\pm} \rightarrow e^{\pm} + \bar{\upsilon_{\mu}}(\upsilon_{\mu}).$$

In such processes both neutral and charged pions would be produced with similar multiplicities and energy distributions. Half of the total energy would be carried away by the neutrinos and consequently possibly not measured due to the difficulty in detecting neutrinos.

The annihilation photons, whose spectrum is peaked around E $\sim$ 70 MeV, have an average energy of 180 MeV and could be detected at a somewhat redshifted value in the cosmic diffuse gamma (CDG) spectrum. In 1971, Stecker *et al* came up with the idea of using distant redshift annihilations, z $\sim$100, to explain the γ spectra at $\sim$1 MeV as originated from the decay of π^o's produced in baryon-antibaryon annihilations. The diffuse γ-ray spectra was recently measured on-board the satellite-borne Compton Gamma Ray Observatory (CGRO) by two groups: the Compton telescope (COMPTEL) [33] and the Energetic Gamma Ray-Experiment Telescope (EGRET) [34]. The COMPTEL measurements covered the energy range from 0.8 to 30 MeV and EGRET the energy range from 30 MeV to 100 GeV. Taking into account the contributions to this spectrum from different astrophysical objects (quasars, supernovae, blazars, etc), the spectrum can be consistently reproduced and no sign of annihilation was found.

A sharp spectral line in the X-rays at 0.36 keV observed by the ROSAT satellite was recently ascribed to the highly redshifted products from direct leptonic annihilations [35]. It is necessary more powerful detectors to explore this region.

Studying the possibility of an universal matter-antimatter symmetry, it was concluded that the electrons produced in the annihilation of different baryonic signed particles should induce a distortion of the Cosmic Microwave Background (CMB) spectrum: photons would suffer scattering to higher energies due to the Compton effect, and electrons could heat the ambient plasma [22]. The predicted signal is yet

lower than the limit established by COBE on departures from a thermal spectrum.

Difficulties in the observation of antimatter

Antinuclei from distant sources necessarily pass through extragalactic magnetic fields. If the fields are too high, they limit the distance from which the antinuclei could approach the Earth. However, with a poor knowledge of the magnetic fields of the Universe [36], the estimation of the distance the antinuclei are from Earth is not very accurate: the range would vary from a fraction of Mpc to the distance of the horizon of the Universe.

After an antinuclei reached our planet the problem would be to detect it. A ground-based detection techniques are not very efficient:

- There is the atmosphere shielding and the consequent several interactions;

- At the time the shower is detected the information about the nature of the primary particle is practically lost.

Balloon detectors are still affected by the residual atmosphere, and they have low statistics once they normally last a couple of days or for few weeks. A more efficient measure would be to install detectors on space for some years. The detector should be equipped with a system to clearly identify the negative charge of the detected particle. This implies a magnetic spectrometer with the capacity to minimize any background imitating the antinuclei.

Until now, the conclusions are that at least within our local supercluster of galaxies (tens of Mpc) there is no antimatter. There were several balloon flights of an instrument called BESS [37] as well as the AMS-01 flight Figure 1.7. Both were magnetic spectrometers and used technologies developed for particle physics accelerator experiments. The upper limit for antihelium search with AMS-01 was obtained assuming that the He and $\overline{\text{He}}$ energy spectrum were identical: $\overline{\text{He}}/\text{He} < 1.1 \times 10^{-6}$. The antihelium search result is illustrated in Figure 1.7.

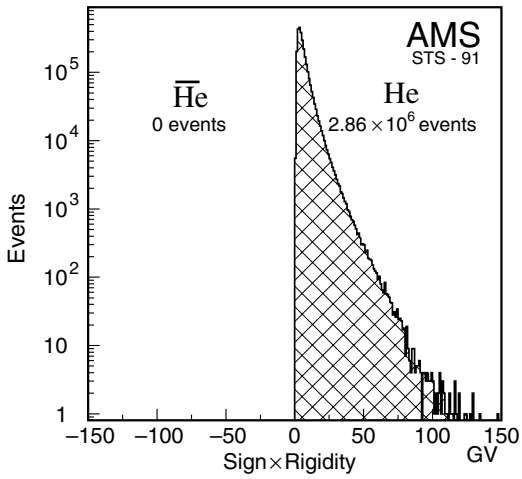

Figure 1.7: *Distribution of rigidity times sign of charge for |Z|=2 particles in AMS-01. No antihelium candidates were found in the range 1-140 GV* [38].

The AMS-02 results for the search of $\overline{\text{He}}$ on the ISS is illustrated in Figure 1.8. The expected upper limit after 3 years of exposure is $\overline{\text{He}}/\text{He} < 10^{-9}$. If no antimatter is found with AMS-02 it can be concluded that there is no antimatter to the edge of 1000 Mpc in the Universe. A comparison between experiments on the limits of

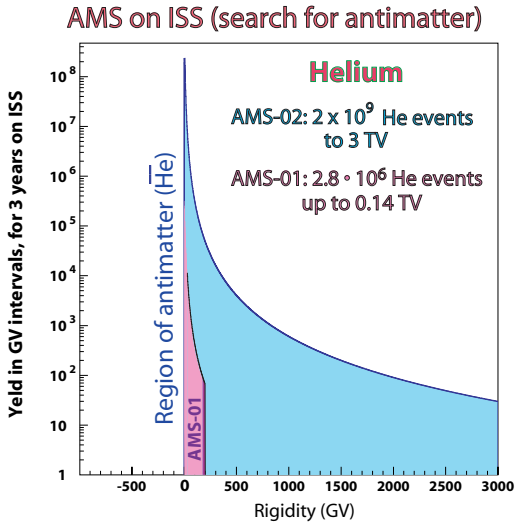

Figure 1.8: *Monte Carlo simulation of the three-year exposure of the AMS detector on the ISS to search for antihelium. The region studied by AMS-01 is also illustrated* [36].

antimatter detection are presented in Figure 1.9.

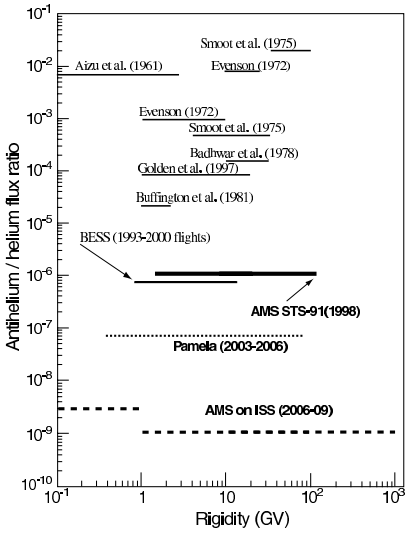

Figure 1.9: *Antimatter limits for different experiments before AMS-02 including AMS-02* [39].

1.8 Dark Matter

Rotational velocities in spiral galaxies and dynamical effects in galactic clusters provide convincing evidence that, either Newton laws completely fail at scales of galaxies or, more likely, most ($\sim 70\%$ calculated from the second kind of measurements) of our matter Universe, that is $\sim 30\%$ of the Universe, is made of non-luminous (dark) matter (the others $\sim 70\%$ of the Universe are believed to be composed of dark energy, identified with the vacuum energy and represented by the cosmological constant Λ).

From the Newton theory of gravitation the orbital velocity of star in the borders of a group of galaxies, at a distance R would be $v = \sqrt{G\frac{M}{R}}$, where M is the mass within the orbit of radius R, and G is the Gravitational Constant. The velocity doesn't depend on the mass of the star, but only on the mass of the Galaxies in the interior of the orbit and on its radius. To have a velocity independent of R, as the astronomical measures point to, it's necessary that the mass M grows linearly with R. The luminosity of galaxies doesn't behave like this with R. If it is only considered the mass corresponding to the luminosity, the stars in the extreme would have an

orbital velocity much lower than the one observed. To explain this observations, it's necessary to evoke the existence of a quantity of dark matter ten or twenty times more abundant than the visible matter [40].

A similar value is supported by the measure of the abundance of deuterium in the Universe. Deuterium, ^{2}H, as well as ^{4}He, were produced during the primordial nucleosynthesis, although in small quantities. As a nucleus relatively instable, the amount produced is highly dependent of the ratio photon/nucleon. From the fraction of deuterium such estimation is obtained and, knowing the density of photons in the CMB, the density of nucleons is inferred. This is a value lower than the expected one.

By different ways, around 70% of the Universe composed of matter turned out to be composed of dark matter.

There are several dark matter candidates [41], [42]:

Baryonic matter:

- Neutrons and protons;
- White dwarfs, which represent the final stage of a star in the main sequence, with a mass between 0.1 and $3M_\odot$[1];
- Brown Dwarfs, that are compact objects with a mass below the ignition threshold (mass $\approx 0.08\ M_\odot$), that is the minimum mass needed to start the full thermonuclear fusion cycle in the core of the object;
- Jupiters, which are hypothetical big planets with a mass of the order of the Jupiter mass.
- Neutron stars, that are the final states of core collapse of Supernovae;
- Cold H_2 gas, a halo surrounding the Spiral Galaxies, is another candidate.

Non-Baryonic matter:

- Thermal Relics: "hot" and "cold" dark matter, depending on their relativistic properties at the time of decoupling from normal matter in the Early Universe,

[1] $M_\odot$ is the Solar mass.

which means particles that, in a first stage were in thermal equilibrium with radiation and then decoupled and were relativistic particles (Hot Dark Matter), from particles which have never been in the same equilibrium, and were not relativistic (Cold Dark Matter).

  - "Hot" Dark Matter (HDM) is required to explain the formation of big structures (cluster of galaxies and so on). Light neutrinos (≈ few tens of eV) are obvious candidates.
  - "Cold" Dark Matter (CDM) is required to explain the formation of small structures (galaxies). Candidates are Weakly Interacting Massive Particles (WIMPs): these can be massive neutrinos of either Dirac or Majorana (m≥20 GeV); supersymmetric (SUSY) particles: s-neutrino, neutralino χ.

- Non-Thermal relics: axions, that are bosons coupled to photons with mass $\approx 10^{-5}$ eV; monopoles, that are topological defects of very large mass $\approx 10^{16}$ GeV predicted by Grand Unified Theories (GUTs).

1.8.1 AMS detection of dark matter

First AMS intended to search for dark matter by high statistics precision measurements of $\bar{p}$, e^+ and γ spectra. These are the different products of WIMP's decay in the galactic halo, by the following modes:

$$\bar{\chi} + \chi \rightarrow \bar{p} + X, e^+ + X, 2\gamma \tag{1.7}$$

$$\chi, \bar{\chi} \rightarrow \gamma\upsilon \tag{1.8}$$

For AMS-01 data, the separation of positrons from large background of protons is limited by the poor performance of the aerogel Čerenkov counter (a Čerenkov detector which allows the mass separation of particles). The energy range is only up to 3 GeV. The AMS fluxes of positron and electron [43], and the positron fraction, $e^+/(e^+ + e^-)$ are consistent with most previous measurement, see Figure 1.10.

AMS-01 can not identify the possible positron signal from annihilation of WIMP at higher energy. AMS-02 with the RICH and the electromagnetic calorimeter (see Subsection 2.2.6) will improve the capabilities of detecting such Dark Matter signal.

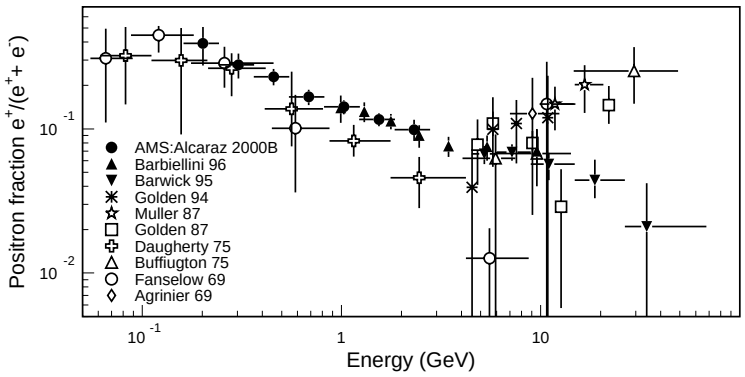

Figure 1.10: *The fraction of positrons of primary cosmic rays measured by AMS-01 and some previous measurements. At energy* $< 3GeV$*, AMS and CAPRICE show consistent observations* [44].

However, as explained before for the antimatter case, extracting a signal from the spectrum of antiprotons is a very difficult task. It was realized that a few processes add up together to flatten out, at low energy the spectrum of secondary antiprotons. The antiproton signal of supersymmetric dark matter is masked.

Searches for low-energy antideuterons appear in the meantime as a plausible alternative, worth being explored [45]. They form when an antiproton and an antineutron merge together. The two antinucleons must be almost at rest with respect to each other in order to happen fusion. For kinematic reasons, a spallation reaction creates few low-energy particles. Low-energy secondary antideuterons are even further suppressed. Energy loss mechanisms are also less efficient in shifting the antideuteron energy spectrum towards low energies. A maximum of 2-5 $\times 10^{-8} \bar{\mathrm{D}}\mathrm{m}^{-2}\mathrm{sr}^{-1}\mathrm{GeV}^{-1}$ appeares for a kinetic energy of $\sim$4 GeV/nucleon. AMS-02 should collect a dozen of secondary antideuterons.

On the other hand, in neutralino annihilations are produced antinucleons with low energies. Subsequently happens the fusion into antideuterons, giving origin to a fairly flat spectrum for supersymmetric antideuterium nuclei. Below a few GeV/nucleon, secondary antideuterons are quite suppressed with respect to their supersymmetric partners. This low-energy suppression is orders of magnitude more effective for antideuterons than for antiprotons which makes formers a much more promising probe of SUSY dark matter than the latters. Unfortunately, the an-

tideuterons fluxes are quite small with respect to the antiprotons.

AMS should reach a sensitivity of 4.8×10^{-8} $\bar{\mathrm{D}}\mathrm{m}^{-2}\mathrm{sr}^{-1}\mathrm{GeV}^{-1}$ at solar minimum activity, pushing it down to 3.2×10^{-8} $\bar{\mathrm{D}}\mathrm{m}^{-2}\mathrm{sr}^{-1}\mathrm{GeV}^{-1}$ at solar maximum, for a modulated energy of 0.24 GeV/nucleon. AMS-02, in 2006, will flight at a maximum of solar activity (1000 MV).

In the case of high energy γ rays the spectral deformation due to χ annihilation is expected to have a strong spatial dependence, imitating the dark matter halo structure which might have more than one clump in the Galaxy. These γ's can be detected by different experiments, with different sensitivities (see Figure 1.11).

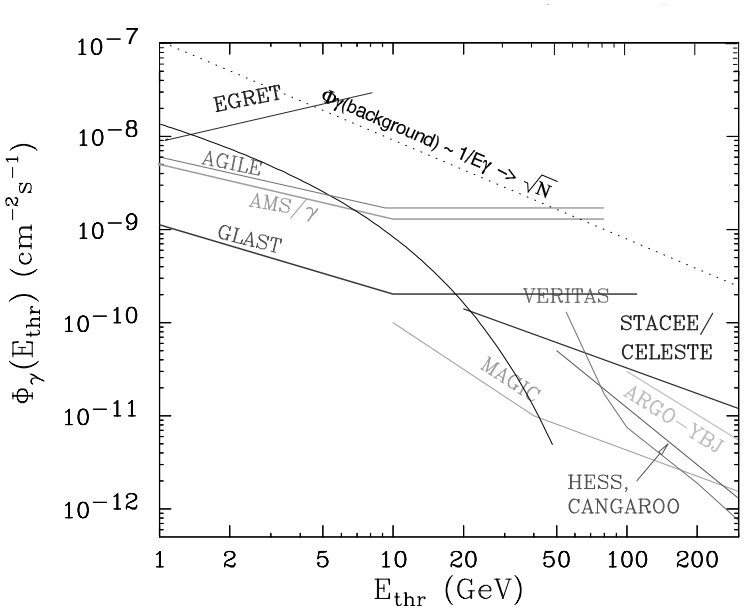

Figure 1.11: *Sensitivity to SUSY dark matter for different γ-ray experiment. Vertical axis: γ rays integral flux above a energy threshold E_{thr}. The dotted line represents the integral flux from known sources, which are a source of background* [39].

Chapter 2

The Alpha Magnetic Spectrometer

2.1 Physics Goals

The **A**lpha **M**agnetic **S**pectrometer (AMS) is a particle detector that will be installed on the **I**nternational **S**pace **S**tation (ISS), in 2006 to measure cosmic ray fluxes for at least three years, at an altitude of 430 Km, on a 51^o degree orbit (see Figure 2.1).

Summarizing the physical aims of AMS, already explored in the last chapter, they will be:

- Search for cosmic antimatter, through the detection of antinuclei with $|Z| \geqslant 2.$;
- Search for non-baryonic dark matter;
- Measurement of primary cosmic-ray spectra below 1 TeV:
  - hydrogen and helium isotopes;
  - beryllium isotopes: by studying the ratio of the radioactive isotope ^{10}Be to the stable isotope ^{9}Be, it is possible to determine the time that cosmic rays are confined to the Galaxy [7];
  - precise measurements of electron and positron spectra;
  - cosmic gamma-rays spectrum.

Figure 2.1: *Artistic view of the International Space Station* [12].

2.2 The AMS-02 Detector

The spectrometer design includes a superconducting magnet, a Time of Flight (TOF), a silicon microstrip Tracker, Veto Counters, a Transition Radiation Detector (TRD), an Electromagnetic Calorimeter (ECAL) and a Ring Imaging Čerenkov Detector (RICH). It will be capable of measuring the rigidity ($R \equiv pc/|Z|e$), the charge (Z), the velocity (β) and the energy (E) of cosmic rays within a geometrical acceptance of $\sim 0.5\ m^2.sr$. A schematic view of all the subdetectors is shown in Figure 2.2.

2.2.1 Transition Radiation Detector

For cosmic particle spectroscopy the AMS will be equipped, at the top of the spectrometer, with a Transition Radiation Detector (TRD) to improve proton background supression from positrons up to 300 GeV.

As a transition radiation detector it is sensitive to a measure of ultra-high energy particles' γ factor through the detection of transition radiation in the X-rays energy range ($\sim$ 1 KeV). This occurs whenever charged particles with $\gamma \gtrsim 1000$ traverse the interface between substances with different dielectric properties. The TRD has 20 layers of fleece radiator with Xe/CO_2 proprotional-mode straw-tube chambers where transition radiation is detected. They are supported in a conically shaped octagon structure [47].

2.2.2 Time of Flight

The Time of Flight (TOF) system of the AMS detector gives the fast trigger to the read out electronics and measures the velocity by the measurement of the time it takes for an incoming particle to traverse the detector and by the measurement of the traversal direction. It also gives an estimation of the charge by measuring the energy deposition.

It will consist of 4 planes of 8, 8, 10, 8 scintillator counters respectively placed at the magnet end-caps: two planes above and the other two below. Its time resolution will be $\sim$ 140 ps for protons and better for higher charges [48].

2.2.3 Superconducting Magnet

Part of the analyzing power of the detector is provided by a superconducting magnet whose design was mainly influenced by the constrains of the maximum weight allowed, while providing the largest possible geometrical acceptance and bending power.

The magnetic dipole field is achieved by an arrangement of 14 superconducting coils. The magnet system consists of a pair of large Helmholtz coils together with two series of six racetrack coils, circumferentially distributed between them. This is the arrangement that minimizes the stray field outside of the magnet and reduces

the magnetic torque, $\vec{N} = \vec{p} \times \vec{B}$, on the ISS resulting from the interaction between the external field of the magnet system and the Earth's field. The magnetic field in the center is of 0.87 T and it is perpendicular to the axis of the cylinder. The magnet has a bending power BL^2=0.78 Tm^2.

All superconducting coils are situated inside a vacuum tank and operated at 1.8 K with superfluid helium. The magnet system will operate in the persistent mode, using a unique phenomenon of superconductors, namely to conduct a constant electrical current without any energy dissipation, which means that once established, it will continue to flow forever without any measurable attenuation [49].

2.2.4 Tracker

The tracking system has a cylindrical shape and is made of 8 double sided silicon planes embedded inside a magnetic field of about 0.87 Tesla and will provide charge measurement and the rigidity measurement (from around 300 MV up to 3 TV), therefore obtaining momentum measurement with an average resolution $\Delta p/p$ of 2%, for protons with energy until 100 GeV/c/nucleon. It uses a large detection area of 7 m^2 [50].

2.2.5 Ring Imaging Čerenkov detector

The **R**ing **I**maging **Č**erenkov detector (RICH) will operate between the TOF and ECAL subdetectors. It was designed to measure the velocity of unitary charges with a resolution $\Delta\beta/\beta = 0.1\%$, to extend the electric charge separation until iron and to provide more information on albedo rejection (particles that enter from the down part). A more detailed description of this subdetector is given in the next chapter.

2.2.6 Electromagnetic Calorimeter

The Electromagnetic Calorimeter (ECAL) is a lead scintillating fibers sampling calorimeter characterized by high granularity that allows to image the longitudinal and lateral development of the shower, which means imaging the shower development in 3D. It allows to discriminate between hadronic and electromagnetic cascades

and also to detect photons. It is prepared to operate over a wide energy range from few GeV up to 1 TeV with a resolution of 2% for 30 GeV [51].

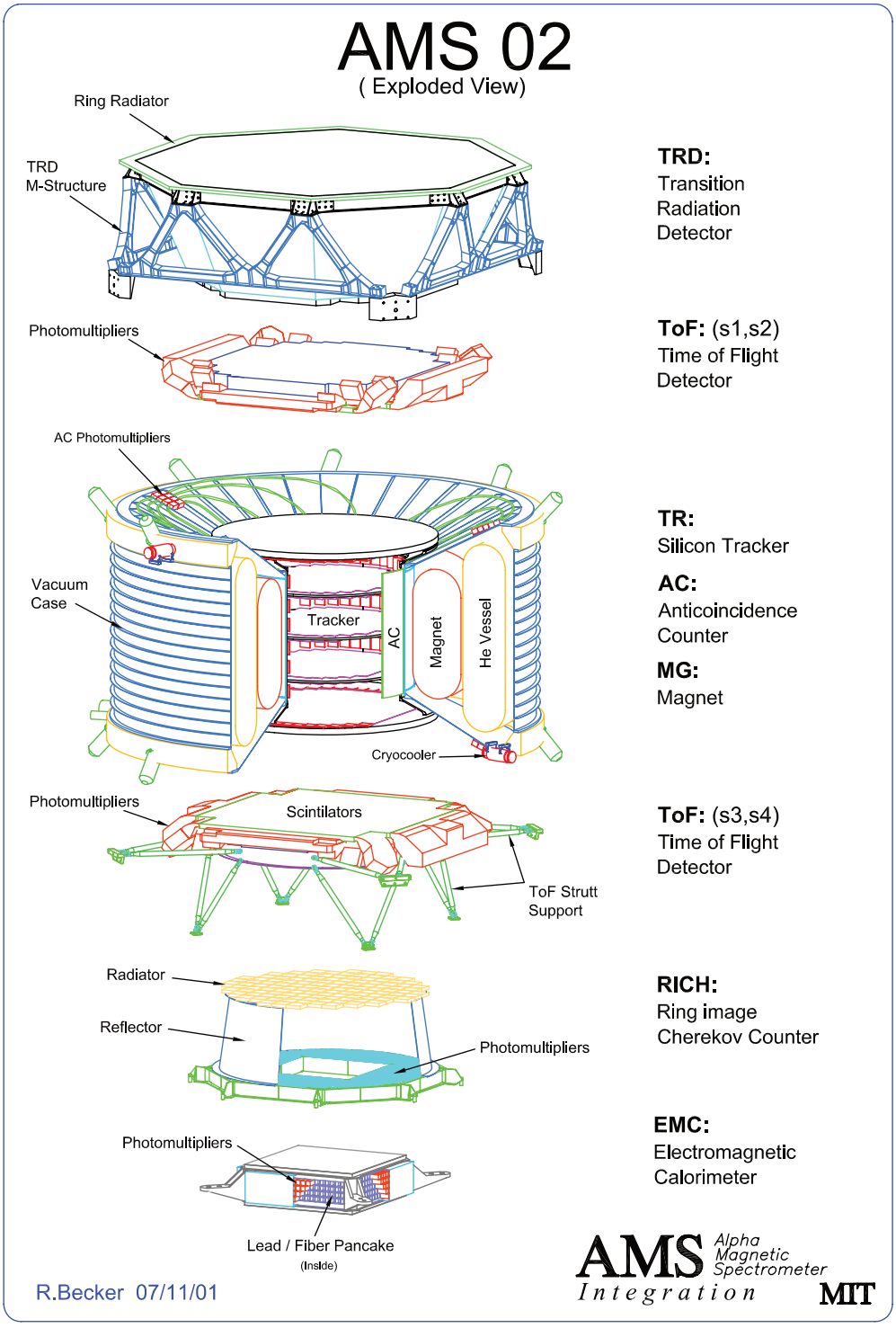

Figure 2.2: *A whole expanded view of the AMS spectrometer* [46].

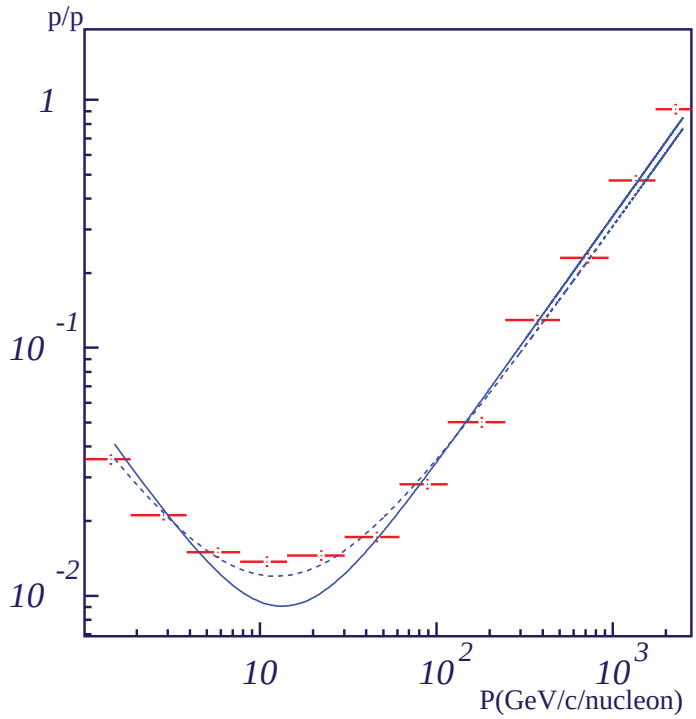

Figure 2.3: *Tracker resolution. There are represented 2 fits: a 2 parameters fit (continuous line)* ($\ln\left(\frac{\Delta p}{p}\right) = \ln\left(\frac{c_1}{p} + c_2 p\right)$ *with* c_1*=0.0606,* c_2*=3.396*$\times 10^{-4}$) *and a 3 parameters fit (dashed line)* ($\ln\left(\frac{\Delta p}{p}\right) = \ln\left(\frac{c_1}{p} + c_2 p + c_3\right)$ *with* c_1*=0.046,* c_2*=3.05*$\times 10^{-4}$, c_3*=4.5*$\times 10^{-3}$*)). By courtesy of P. Gonçalves.*

Chapter 3

The RICH Detector of the AMS Experiment

The **R**ing **I**maging **Č**erenkov detector (RICH) was designed to perform velocity measurements, measuring the velocity of singly charged particles with a resolution $\Delta\beta/\beta = 0.1\%$ and to extend the electric charge separation up to the iron element (Z=26). The RICH will also contribute to the $e^-/\bar{p}$ and e^+/p discrimination and to the albedo particle rejection.

The high accuracy obtained with the RICH on the velocity measurement allows to discriminate isotopes, such as heliums and berylliums, up to a kinetic energy per nucleon of ∼10 GeV.

The RICH geometrical acceptance is of $\sim 0.4\ m^2.sr$, which is around 80% of the AMS acceptance. Figure 3.1 compares the polar angle distribution for a simulated set of events passing through AMS and the RICH detector.

As the name says, it is a detector using the Čerenkov effect to recognize charged particles that cross its radiator and emit photons by the same effect.

3.1 Čerenkov radiation

The Čerenkov radiation effect was identified and characterized, in 1934, by Vavilov and Čerenkov while they were studying the effects of gamma rays on liquids and explained in 1937 in the frame of classical electrodynamics by I. M. Frank and I. E. Tamm.

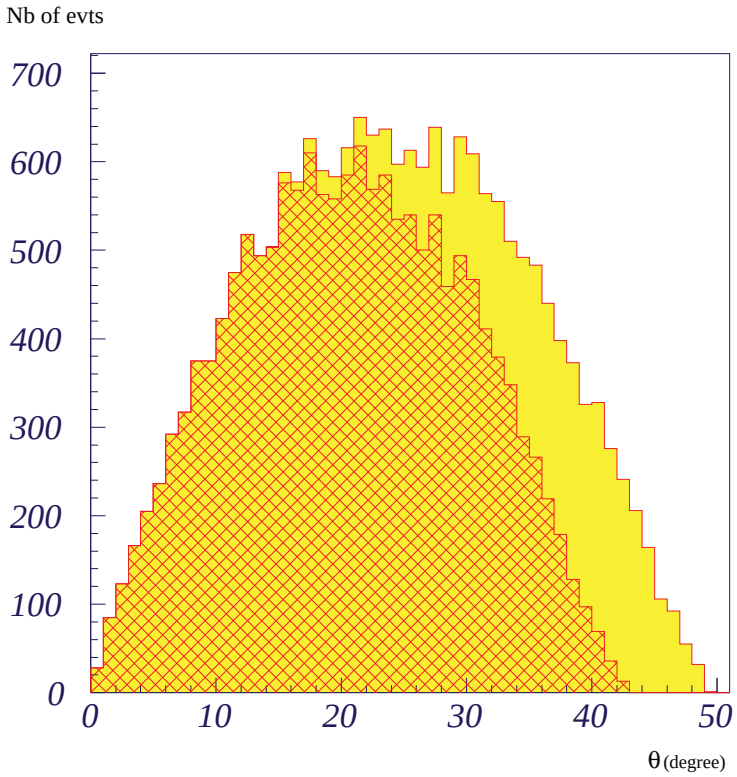

Figure 3.1: *The RICH acceptance is around 80% of the AMS acceptance. RICH accepted polar angles are represented in the shaded region and AMS accepted polar angles are in the continuous region.*

A charged particle crossing a dielectric medium, with a refractive index n, polarizes the atoms of the same medium. If the speed of the particle, $v = \beta c$, is lower than the speed of light in the medium, $c_n = c/n$, the polarization is symmetric around the trajectory points of the particle and the interference between the wavefronts doesn't occur. On the other way, if the speed is greater than the speed of light in the medium, the wavefronts generated in each point of the particle's path create a constructive interference and it is emitted coherent radiation with an angular aperture θ_c in relation the direction of motion, with the photons distributed in a surface of a cone with an aperture $2\theta_c$. This is the Čerenkov effect, and θ_c is the Čerenkov angle.

The necessary condition, $v > c/n$, implies the inequality 3.1.

$$\beta n > 1 \tag{3.1}$$

and can be understood from the Huygens's construction of Figure 3.2. The same

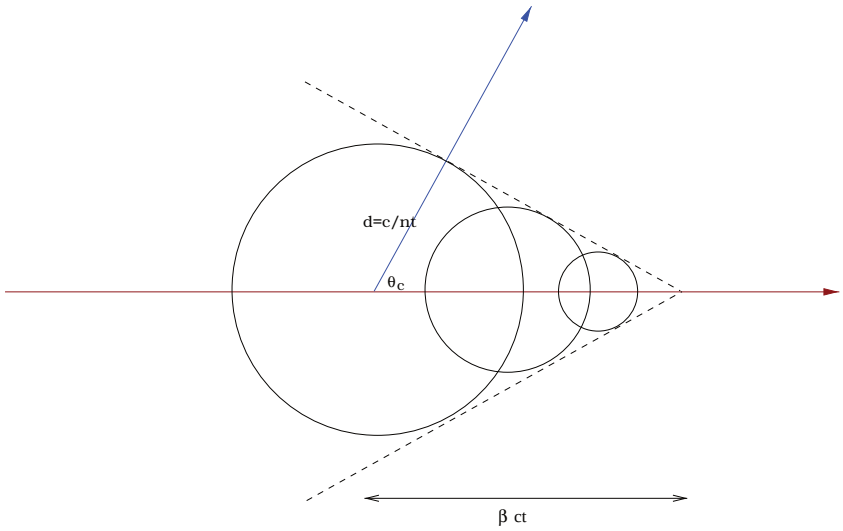

Figure 3.2: *Huygens's construction for the Čerenkov radiation emitted by a particle traveling with a speed v greater than c/n, the speed of light in the medium. The resulting wavefront is indicated by the dashed line and moves in the direction of the arrow.*

construction also implies the $\cos\theta_c$ should obey expression 3.2.

$$\cos\theta_c = \frac{c/n}{\beta c} = \frac{1}{\beta n} \tag{3.2}$$

Consequently, the determination of θ_c is a direct measurement of the velocity of the particle. The first value of β that obeys eq. 3.1 is called the *threshold* velocity.

According to eq. 3.2, the emission angle depends on the particle speed (β) and on the refractive index (n). For different refractive indexes there are different *threshold* velocities and different maximum emission angles according to the particle's velocities, as can be seen in Figure 3.3.

The energy carried off by Čerenkov radiation (E) per unit of length (dx) and range of frequency ($d\omega$) for a particle of charge Ze was calculated by Frank and Tamm and take the form:

$$\frac{d^2E}{dxd\omega} = \frac{Z^2\alpha\hbar}{c}\left(1 - \frac{1}{\beta^2 n^2}\right)\omega, \tag{3.3}$$

where $\alpha = \frac{e^2}{4\pi\epsilon_0\hbar c}$ is the fine structure constant. The radiated energy grows linearly with the frequency and with the square of the electric charge. Since the energy carried by each photon is:

$$E_\gamma = \hbar\omega \tag{3.4}$$

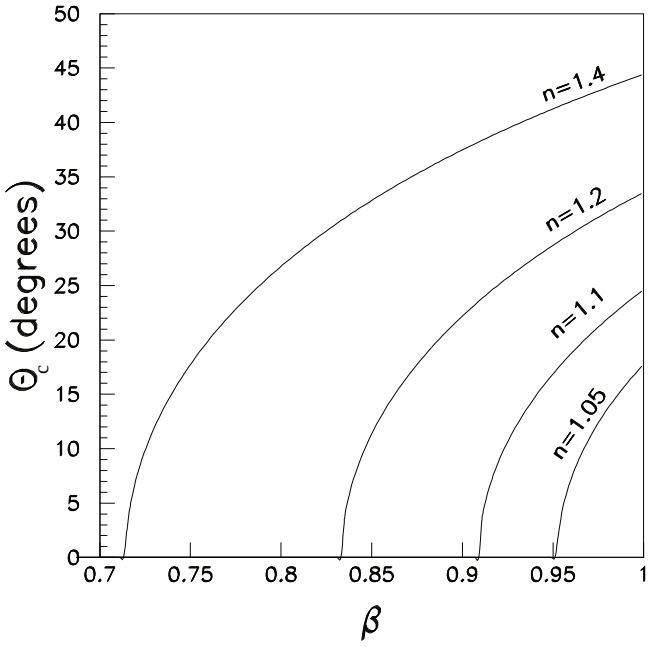

Figure 3.3: *Dependence of the emission angle (θ_c) with the particle speed (β) and with the refractive index (n).*

and being N_γ^{rad}, the total number of radiated photons, the total radiated energy, E is:

$$E = N_\gamma^{rad} E_\gamma \Rightarrow dE = E_\gamma dN_\gamma^{rad}, \tag{3.5}$$

allowing to express the number of radiated photons per unit of length and range of frequency to be expressed as:

$$\frac{d^2 N_\gamma^{rad}}{dx d\omega} = \frac{Z^2 \alpha}{c}\left(1 - \frac{1}{\beta^2 n^2}\right). \tag{3.6}$$

The total number of radiated photons per unit of length in terms of the wavelength is obtained using the following integration:

$$\frac{dN_\gamma^{rad}}{dx} = 2\pi\alpha Z^2 \int_{\lambda_1}^{\lambda_2} \left(1 - \frac{1}{\beta^2 n^2(\lambda)}\right) \frac{d\lambda}{\lambda^2}\,. \tag{3.7}$$

In practice, the total number of radiated photons per unit of length is only calculated in the range of wavelengths detectable by the photomultipliers. If the variation of $n(\lambda)$ (for a discussion of this variation, see Subsection 5.3.4) is smooth in the same range and using eq. 3.2, one can get:

$$\left\langle 1 - \frac{1}{\beta^2 n^2(\lambda)} \right\rangle = \left\langle 1 - \cos^2\theta_c \right\rangle = \left\langle \sin^2\theta_c \right\rangle. \tag{3.8}$$

The number of radiated photons per unit of length comes:

$$\frac{dN_\gamma^{rad}}{dx} = 2\pi\alpha Z^2 \left\langle \sin^2\theta_c \right\rangle \left(\frac{1}{\lambda_1} - \frac{1}{\lambda_2} \right). \tag{3.9}$$

The number of radiated photons per unit length and energy is given by:

$$\frac{d^2N_\gamma^{rad}}{dxdE} = \frac{2\pi\alpha}{hc} Z^2 \left(1 - \frac{1}{\beta^2 n^2} \right), \tag{3.10}$$

which results from substituting $d\omega$ by $dE/\hbar$ in eq. 3.3 and using 3.5.

Therefore, the light yield increases with the radiator thickness (L), the particle squared charge (Z), the particle velocity (β) and the refractive index of the medium (n). The constant term in expression 3.10 is 370 $\text{cm}^{-1}\text{eV}^{-1}$, which allows to write:

$$\frac{d^2N_\gamma^{rad}}{dxdE} = 370 Z^2 \left(1 - \frac{1}{\beta^2 n^2} \right). \tag{3.11}$$

3.2 The RICH setup

The **R**ing **I**maging **CH**erenkov detector (RICH) is a proximity focusing detector with a low refractive index radiator: aerogel n=1.030 or n=1.050 (still to be decided), a high reflectivity mirror and a basis with light guides and photomultiplier tubes. In Figure 3.4 is represented a perspective and a schematic view of the RICH detector with the corresponding dimensions, with a more detailed description in the following subsections.

The cone radiated by the Čerenkov effect, produced by the charged particles crossing the radiator with a velocity higher than the light speed in the medium, intersects the detection basis, drawing a ring, as the one represented in Figure 3.5.

It is called a proximity focusing detector because due to the radiator thickness, there are series of concentric Čerenkov rings emitted, each corresponding to a different emission point located along the particle's path. In the simple case of the vertical incidence of the particle illustrated in Figure 3.6, the focusing effect is almost achieved since the expansion height, H, is much larger than the radiator thickness, T. Consequently, the ring width, $W = T\tan\theta_c$, is negligible compared with the ring radius, R. For $\beta \sim 1$, $W \sim 0.74$ cm for an aerogel, radiator 3 cm thick.

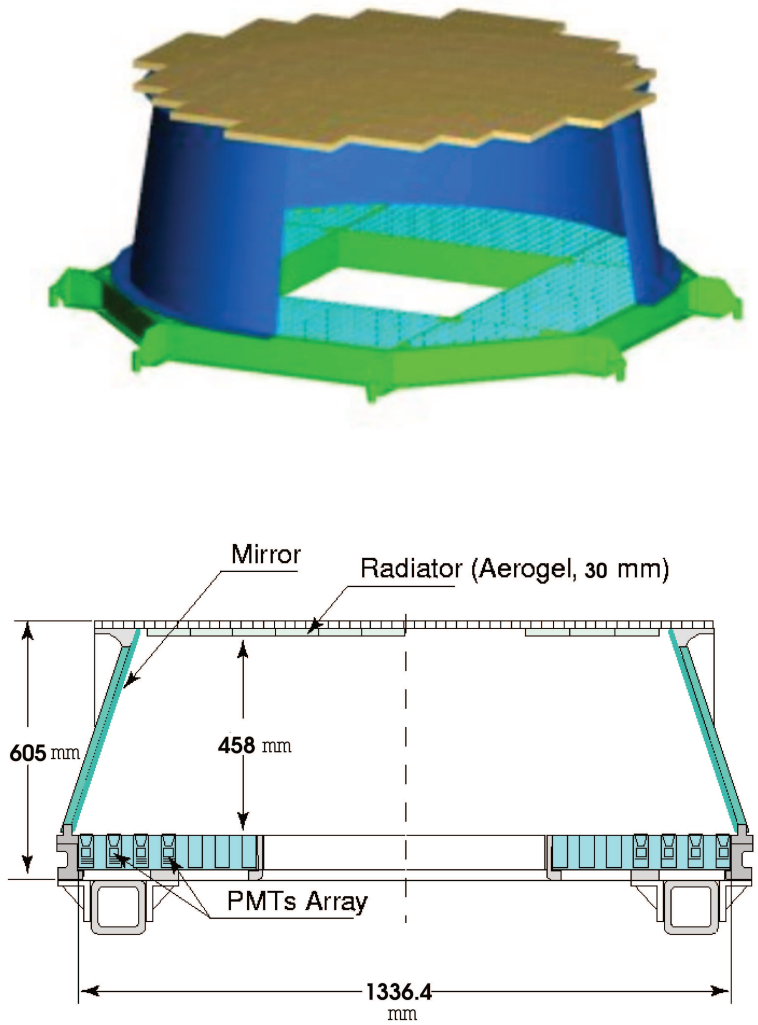

Figure 3.4: *Perspective and side-view of the RICH detector* [46].

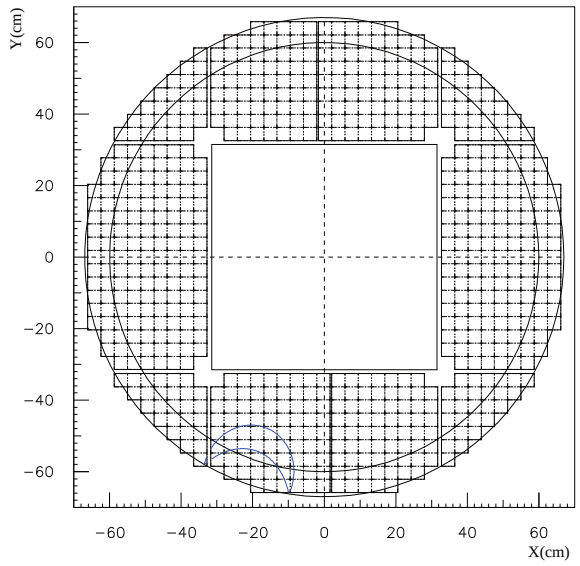

Figure 3.5: *An event detected in the PMT matrix, generated in aerogel radiator, n=1.030, 3 cm thick, together with an expansion volume height of 45.8 cm. Particle $\beta \sim 0.999$. This pattern includes reflected and non-reflected branches. The inner and outer circular lines correspond respectively to the upper and lower boundaries of the conical mirror. The square is the limit of the non-active region. The different modules of the matrix are represented and the small squares are the photomultipliers. More details of the matrix are shown in 3.14.*

For different inclinations, W will also be a function of the particle polar angle θ and of the azimuthal angle of the photon φ.

Its design was drastically constrained by: volume, weight (currently ∼190 kg), power consumption, long term reliability of components, the magnetic field in the photodetector region, which will reach close to 300 G in the photodetector volume, and the amount of matter traversed since bellow the matrix there will be an electromagnetic calorimeter [52].

3.2.1 Radiator

A low index radiator was choosen regarding the aim of a large kinematic region coverage and particle identification the highest momentum possible. The selected candidate is silica aerogel (from now on abbreviated as Agl) with a refractive index of 1.030 or 1.050 and with a thickness of 3 cm. It is composed of squared tiles with a side length of 11.5 cm.

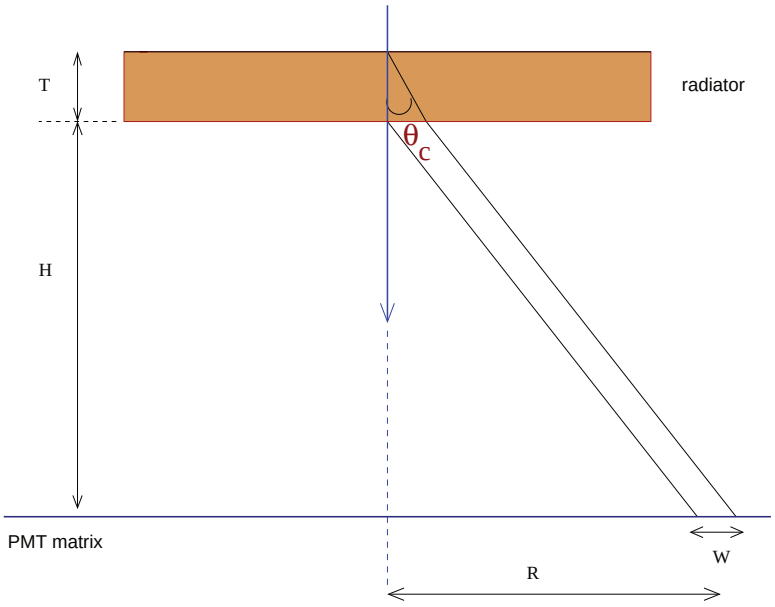

Figure 3.6: *Effect of the radiator thickness in the case of vertical incidence. Instead of a well defined ring, there are concentric rings according to the radiation emission point [5].*

Sodium fluoride (NaF) provides a more conservative choice for the radiator since it has already been used in another flights (for example CAPRICE [53]). Meanwhile, due to its higher refractive index n=1.334, it will cover lower momentum regions.

The kinetic energy per nucleon threshold is a function of the refractive index and is given by,

$$(n/\sqrt{n^2-1}-1)m$$

. For aerogel 1.030 and sodium fluoride the thresholds are respectively, 0.5 Gev/nucleon and 3 Gev/nucleon. The previous observations are shown in the left part of Figure 3.7.

For aerogel the radiation light yield is N_γ=50/cm for a unitary charge with $\beta \sim 1$ (this is obtained from integration of eq 3.10 along the path traversed by the particle and in the range of the emission energy). The right plot of Figure 3.7 is obtained from the integration of expression 3.10 along the path crossed by the particle, using the photomultiplier efficiency at the basis and integrating over the radiated energy:

$$N_{pe} \simeq 370 Z^2 L \left\langle \sin^2 \theta_c \right\rangle \frac{\int \epsilon(E) dE}{\Delta E}, \tag{3.12}$$

where N_{pe} is the number of photoelectrons detected, L is the path crossed by the

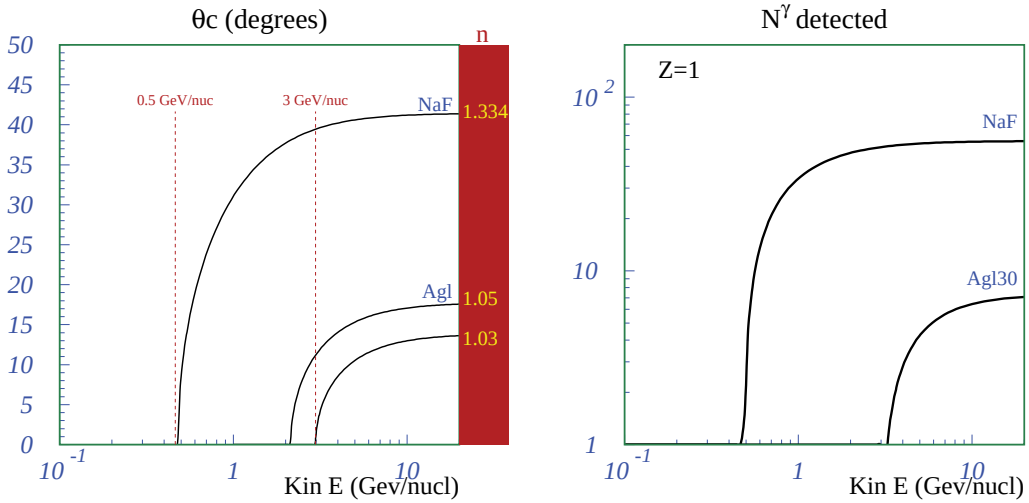

Figure 3.7: *Variation of the Čerenkov angle with the kinetic energy for different radiator materials: aerogel 1.030, 1.050 and sodium fluoride* (left).
Evolution of the number of photons emitted by a singly charged particle with the kinetic energy for aerogel 1.030 and sodium fluoride (right).

particle and $\int \epsilon(E)dE/\Delta E$ is the PMT mean efficiency. The values of energy used to integrate are the values to which the photomultipliers are sensitive (see Figure 3.13 for the corresponding wavelengths). After this the number of detected photons is ~ 7 generated by the same particle in aerogel. For sodim fluoride (NaF) radiator this value is higher: ~ 50.

Aerogel is a porous material with microscopic air pockets. Due to this structure, particles that cross the material suffer Rayleigh scattering, losing their original direction. The transmittance, t, is a measure of the fraction of unscattered photons at the exit of the radiator. It is a function of the path length crossed by the photon in the medium, according to the expression bellow:

$$t(x, \lambda) \propto exp(-Cx/\lambda^4), \tag{3.13}$$

where x is the distance crossed in the radiator and λ is the photon wavelength. The coefficient C, called the clarity coefficient is a measure of the material transmittance. The greater the clarity coefficient the lower the transmittance. The NaF has a negligible clarity coefficient and one of the samples of aerogel 1.030 that is being tested (Novosibirsk hydrophilic) has a value of 0.0074 $\mu m^4 cm^{-1}$.

Photons can also be absorbed in the radiator material. In aerogel the absorption is negligible compared with Rayleigh scattering. In NaF, absorption is the only interaction that photons can suffer.

Above the radiator there is an acrylic plastic foil, 1 mm thick, Bicron-BC800 with a refractive index of 1.49. This was included for mechanical support of the radiator tiles.

3.2.2 Mirror

In order to increase the number of collected Čerenkov photons in the photomultipliers matrix, a conical high-reflectivity mirror was included. The mirror reflectivity, ρ, is 0.85.

Figure 3.8 presents the relative quantity of the photons, coming from a particle with $\beta \sim 1$, reaching the PMT readout matrix that had suffered reflection. In the NaF case, basically half of the photons had suffered reflection due to the larger emission angle ($\theta_c \sim 40^o$). In aerogel, this quantity is much more dependent on the particle track (direction and impact point), consequently varies much more event by event. Therefore, the distribution is much more uniform.

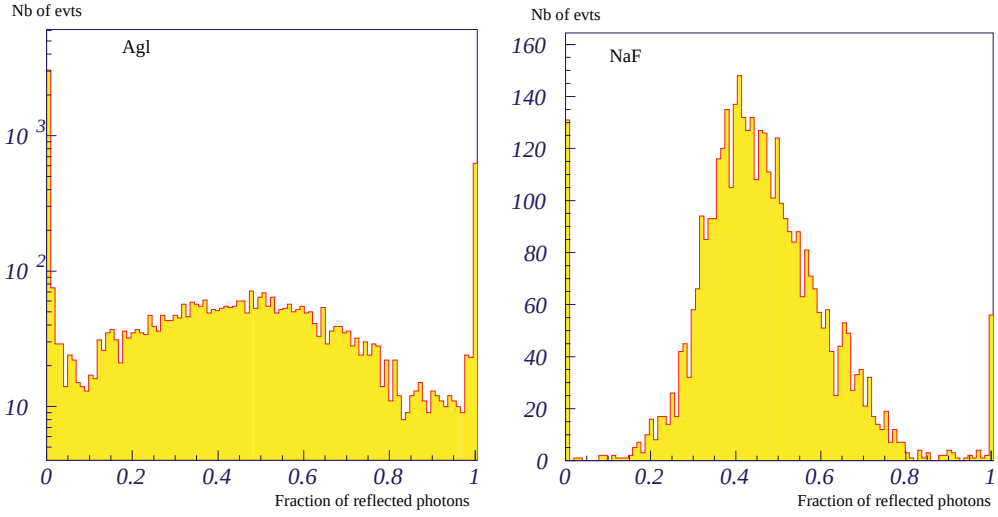

Figure 3.8: *Fraction of reflected photons at the detection matrix (at the top light guides level) generated by a sample of particles generated in the AMS acceptance, with $\beta \sim 1$ in aerogel 1.030* (left) *and sodium fluoride* (right) *together with an expansion volume height of 45.8 cm. (Mirror reflectivity=0.85).*

3.2.3 Light guides

In order to reduce dead areas between adjacent photomultipliers, an array of light guides was added, coupled to each photomultiplier (PMT). However, because of the need to shield the PMTs from the magnetic field of the superconducting magnet and consequently due to mechanical assembly reasons, there are gaps even at the top level of the light guides. A light guide unit is a pyramidal polyhedron composed of 16 solid Plexiglass pieces, with a refractive index of 1.49. A schematic insertion of the light guide with a PMT is shown in Figure 3.9 and a picture of the detection cell is presented in Figure 3.10 [52]. The cell fits inside a shielding tube that is not shown in the last picture. In the light guide, there are 16 pieces, that can be

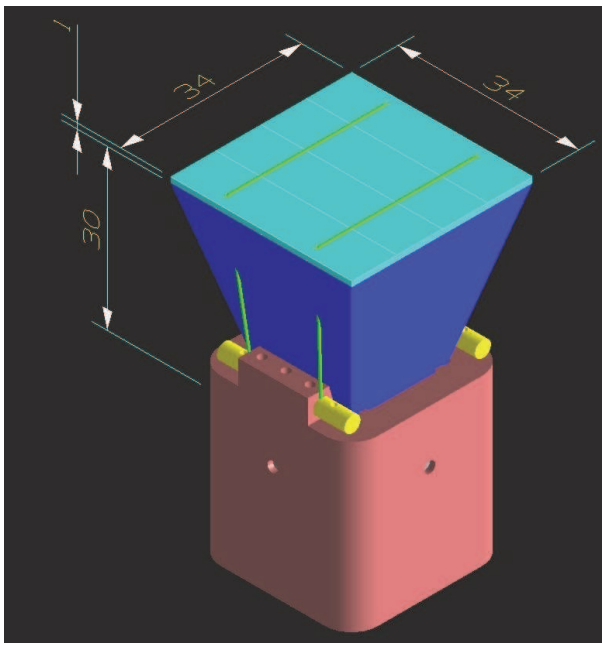

Figure 3.9: *PMT housing plus light guide* [46].

observed in Figure 3.11, because of the 16 channels per PMT. The 16 pieces are held together by a thin layer on the top. This allows the 16 pieces to be separated by air, in order to conduct light by internal reflections. The active pixel size is of 8.5 mm and the gap between successive light guides is 3 mm.

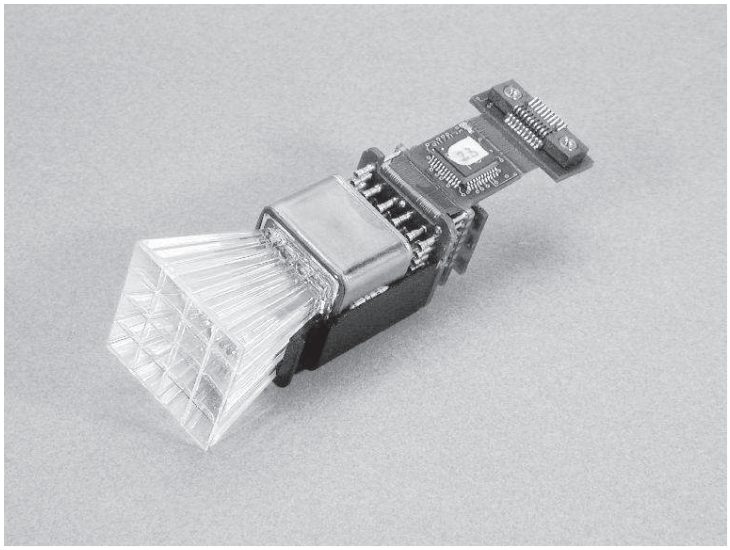

Figure 3.10: *Detection cell including PMT, front end electronics, light guide matrix and (half) housing shell* [54].

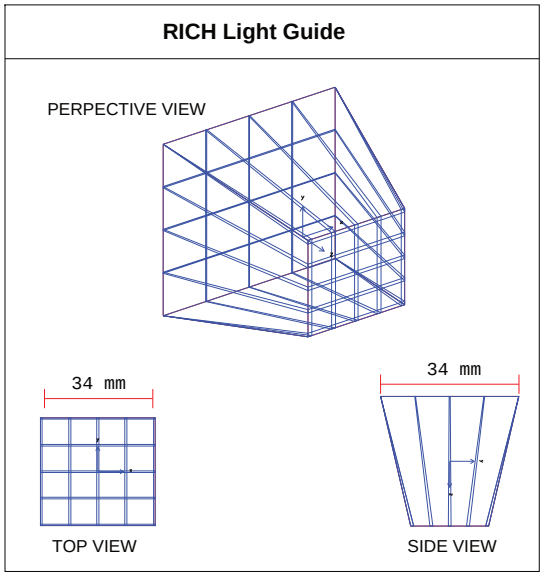

Figure 3.11: *Schematic draw of the RICH light guides.*

Light Guide Efficiency

The light guide efficiency factor depends on the incidence angle of the photons (θ_γ) on the top of the light guide. The variation is explicit in the right plot of Figure 3.12: the higher the angle (θ_γ), the lower the light efficiency to detect the same photon. The NaF radiated photons have larger angles (see left plot of

Figure 3.12) and therefore lower efficiencies.

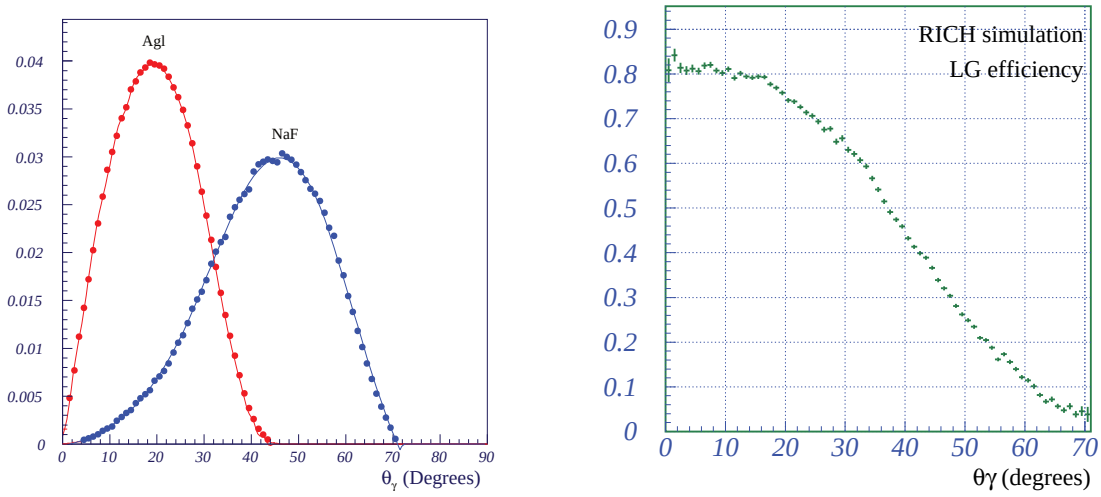

Figure 3.12: *Incidence angles at the top of light guide for Agl and NaF* (left). *Light guide efficiency as function of the incident angle at the top of the light guide* (right).

3.2.4 Photomultipliers

The detection matrix is composed of 680 photomultiplier tubes (PMTs). The photomultiplier selected is the 16-anode R7900-M16 from Hamamatsu [55], with a pixel size of 4.5 mm. The chromatic range of counter will be limited at short wavelengths by the cutoff of the Borosilicate window, being the spectral response from 300 to 650 nm, with the maximum at λ=420 nm, according to the curve shown in 3.13.

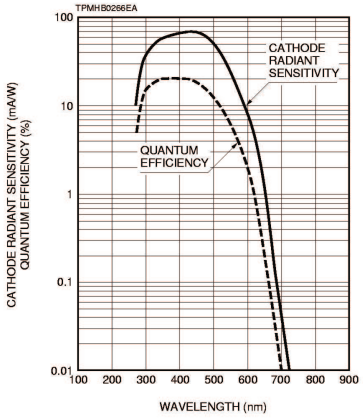

Figure 3.13: *PMT quantum efficiency* [55].

The matrix is composed of different modules with gaps between them. As it was referred before there is a non-active area at the center to insert the electromagnetic calorimeter (ECAL), which is a square with a side length of 63 cm. The detail of the matrix is represented in Figure 3.14.

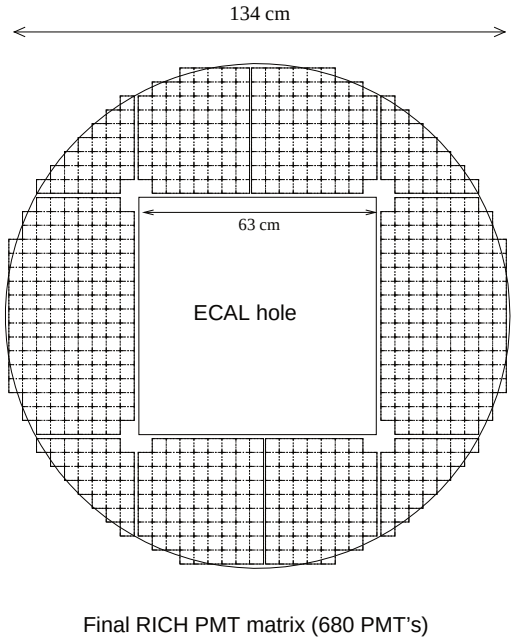

Figure 3.14: *RICH PMT matrix (680 PMTs): detail of the matrix with the active parts and the inactive ones: ECAL hole, module gaps.*

3.3 The RICH Prototype

There is a prototype of the RICH detector, since the end of 2000, which incorporates most of the final detector elements. A previous one had been constructed before and was tested. The purpose is to test the performances of the detector relating to velocity and charge measurement. It has been developed and assembled at ISN (Institut des Sciences Nucléaires), Grenoble-France. This prototsype has a simpler mechanical structure than the flight setup. Basically is a PMT matrix that represents about 1/6 of the complete matrix (see Figure 3.15) but with the same kind of photomultipliers. There isn't a mirror and the light guides are smaller with a size that equals the pitch: 31 mm.

The radiator materials in study are also aerogel (n=1.030, 1.050) and sodium

fluoride. There is a polyester foil to support the radiator, 0.75 mm thick.

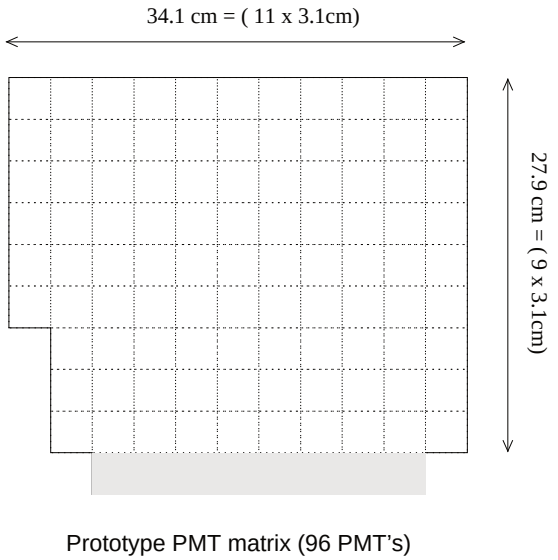

Figure 3.15: *The Prototype PMT matrix consists of an approximate module of the final setup. The shaded row doesn't contain PMTs.*

It was already tested using cosmic muon events, in a 3 days run, which corresponded to 200.000 events; and in a test beam using the beam obtained from the CERN SPS ion beam colliding on a fragmentation analyzer, covering charges up to iron.

The tests had success and the construction of the flight model is in run.

3.4 RICH Standalone Simulation

The RICH detector was fully simulated through the GEANT3 package (available in [56]). Different geometry configurations were implemented and the physical processes, namely Čerenkov radiation, photon scattering and absorption, were simulated.

The RICH simulation was used intensively on this thesis, for the dual radiator optimization and to cross-check the acceptance calculations.

The generated events, when not specifically described, are isotropically distributed on the solid angle (before applying AMS acceptance) and uniformly distributed on the primary impact plane.

The homogeneous distribution of the impact points in the radiator is visible in Figure 3.16. The accepted particles θ in RICH detector were shown in Figure 3.1.

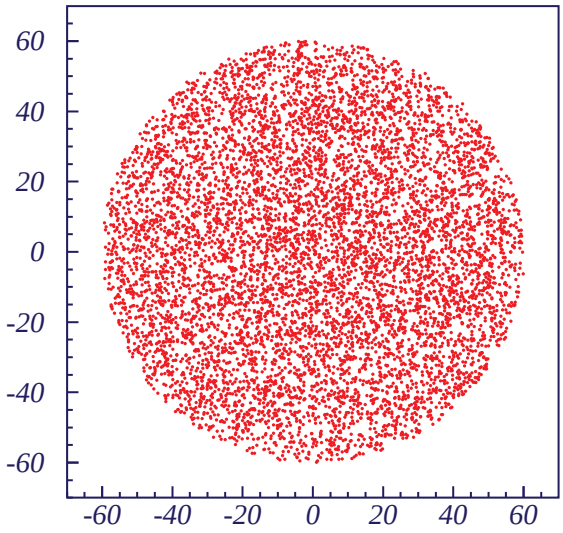

Figure 3.16: *Distribution of the impact points of the incident particles in the top of the radiator.*

The fraction of events which are generated within the AMS acceptance and pass through the RICH radiator, gives the RICH geometrical acceptance.

3.5 Čerenkov Angle Reconstruction

The Čerenkov angle reconstruction uses information of the particle direction provided by the tracker, which, extrapolated to the radiator, provides an estimation of the mean photon emission vertex, considered to be at 65% of the radiator high. The hits left in the light guides by the particle give an additional track element. There are hits from the particle and from the photons that correspond to their impact points in the pixels.

The reconstruction of the Čerenkov angle has to deal with two kinds of photons: those which are only slightly deviated from the expected photon pattern due to the pixel granularity, radiator thickness and chromaticity effects (referred in Section 5.3.4), and those which spread all over the detector due to photon scattering and are faked by the photomultipliers noise. The photons corresponding to the signal,

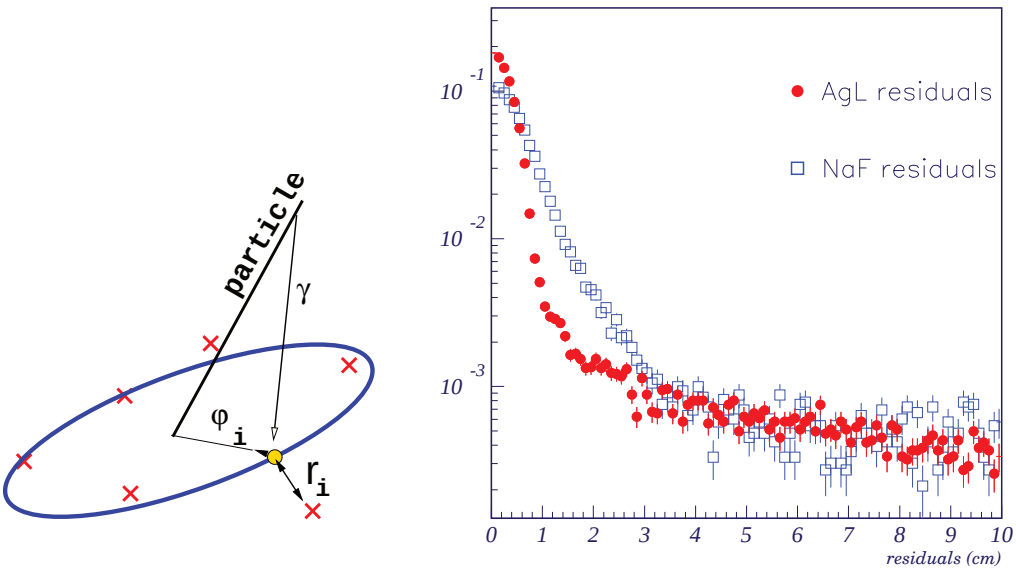

Figure 3.17: *Hits distance to the expected Čerenkov pattern* (left). *Residuals distribution for Agl and NaF, both normalized to 1* (right).

produce the Čerenkov photon pattern and their distances to the expected pattern are Gaussian distributed with a σ reflecting the previous effects.

Sodium fluoride and aerogel clearly produce different residuals distributions, which are the distribution of the hits distance to the expected pattern (see right Figure 3.17). NaF has a 4σ width of 2.4 cm, and aerogel a 4σ width of 1.2 cm. This is used to establish the selection of Čerenkov hits, which considers hits closer, than the previous distance values, to the expected pattern. The latter kind of photons constitute an essentially flat background modulated by the geometry of the detection plane.

The probability density function for a detected hit to belong to the pattern is expressed as:

$$p_i = (1-b)\frac{1}{\sigma}\sqrt{\frac{2}{\pi}} exp\left[-\frac{1}{2}\left(\frac{r_i}{\sigma}\right)^2\right] + \frac{b}{d}, \tag{3.14}$$

where b is the photon background fraction, d is the active matrix dimension, hence b/d is the background fraction per unit of distance ($\sim 10^{-3}$/cm). r_i is the closest distance from the hit i to the Čerenkov pattern (see left scheme of Figure 3.17).

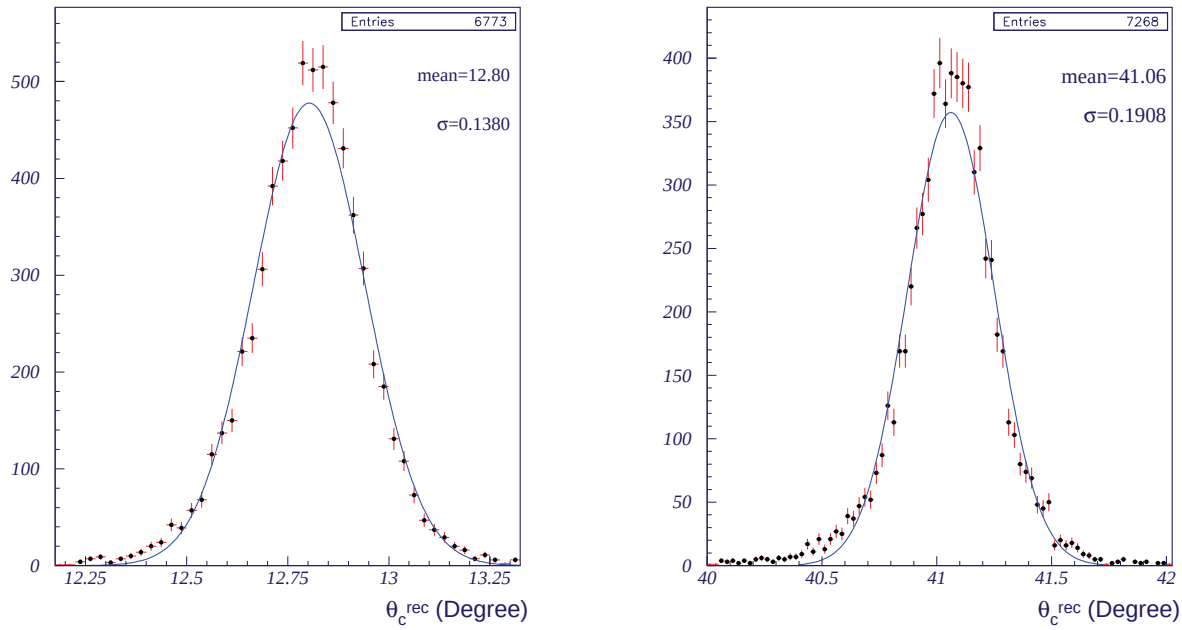

Figure 3.18: *Reconstructed θ_c distribution for heliums with a momentum per nucleon of 10 GeV/c/nucleon in AgL* (left) *and NaF* (right) [5].

The best value for θ_c will be obtained by maximizing the Likelihood function, built as the product of the probabilities that the detected hits belong to a given (hypothesis) Čerenkov ring:

$$L(\theta_c) = \prod_{i=1}^{nhits} p_i \left[r_i(\theta_c) \right] . \tag{3.15}$$

In order to trust the reconstruction, only events with at least 3 hits close to the reconstructed pattern were selected. The θ_c reconstruction results, using the simulation, for heliums with a momentum of 10 GeV/c/nucleon in aerogel and sodium fluoride are presented bellow in Figure 3.18.

For a more complete description of Čerenkov angle reconstruction method and results see J. Borges' thesis [5].

Chapter 4

Photon Ring Acceptance

When a charged particle crosses the radiator, a certain number of photons are emitted uniformly around the particle with an aperture angle θ_c. The photons are either refracted or fully reflected at the radiator's boundary, depending on their incident angle (θ_i). Those which pass the radiator can have reflections on the conical mirror and then reach the photomultiplier plane where they can be detected. Therefore, a hit pattern is produced with a geometrical ring acceptance depending on the radiator particle's impact point (I), particle's direction (θ, ϕ) and photon's aperture angle (θ_c). This is schematically represented on the following Figure 4.1.

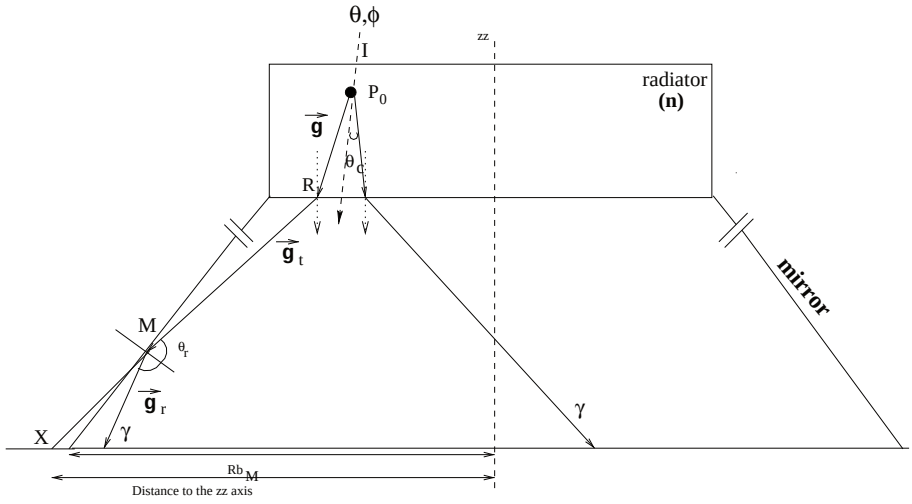

Figure 4.1: *Scheme with the photon's path length through the RICH detector. One of the photons is reflected and the other, at right, reaches directly the photomultiplier plane of the detector.*

Photons are fully characterized once is known the emission point $P_0 = (x_0, y_0, z_0)$ and the direction $\vec{g}$ defined within a frame attached to the RICH detector and named here from, *detector's frame*. The direction ($\vec{g}$) of the photons in the *detector's frame* is obtained from its direction ($\vec{g'}$) in a frame having the z-axis collinear with the particle's direction (*particle's frame*), by applying a transformation matrix (T) between the two frames.

4.1 Photon Direction in Particle's Frame

In the *particle's frame*, the photon direction is given in terms of the Čerenkov angle θ_c and the azimuthal angle φ, by the following terms:

$$\vec{g'}(\theta_c, \varphi) = (\sin\theta_c \cos\varphi, \sin\theta_c \sin\varphi, \cos\theta_c) \tag{4.1}$$

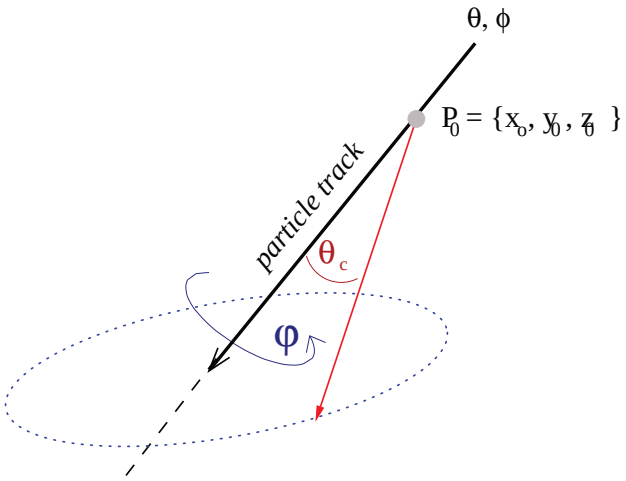

Figure 4.2: *Scheme of the tracing in particle's frame.*

4.2 Photon Direction in Detector's Frame

The transformation matrix elements are defined as $T_{i,j} = \vec{e_i} \cdot \vec{e}_{j'}$, where $\vec{e}_{i,j'}$ are the basis unitary vectors giving the directions of the two frames axis (see Figure 4.3 for the two frames definition). Explicitly, these directions can be written as:

$$\vec{e_z} = (0,0,1) \qquad \vec{e'_z} = (\sin\theta\cos\phi, \sin\theta\sin\phi, \cos\theta)$$
$$\vec{e_y} = (0,1,0) \qquad \vec{e'_y} = (\sin\phi, -\cos\phi, 0)$$
$$\vec{e_x} = (1,0,0) \qquad \vec{e'_x} = \vec{e'_y} \times \vec{e'_z} = (-\cos\theta\cos\phi, -\cos\theta\sin\phi, \sin\theta)$$

Thus, the photon's direction is transformed in the detector's frame as follows:

$$\vec{g} \equiv \begin{pmatrix} g_x \\ g_y \\ g_z \end{pmatrix} = \begin{pmatrix} -\cos\theta\cos\phi & \sin\phi & \sin\theta\cos\phi \\ -\cos\theta\sin\phi & -\cos\phi & \sin\theta\sin\phi \\ \sin\theta & 0 & \cos\theta \end{pmatrix} \cdot \begin{pmatrix} g'_x \\ g'_y \\ g'_z \end{pmatrix} \tag{4.2}$$

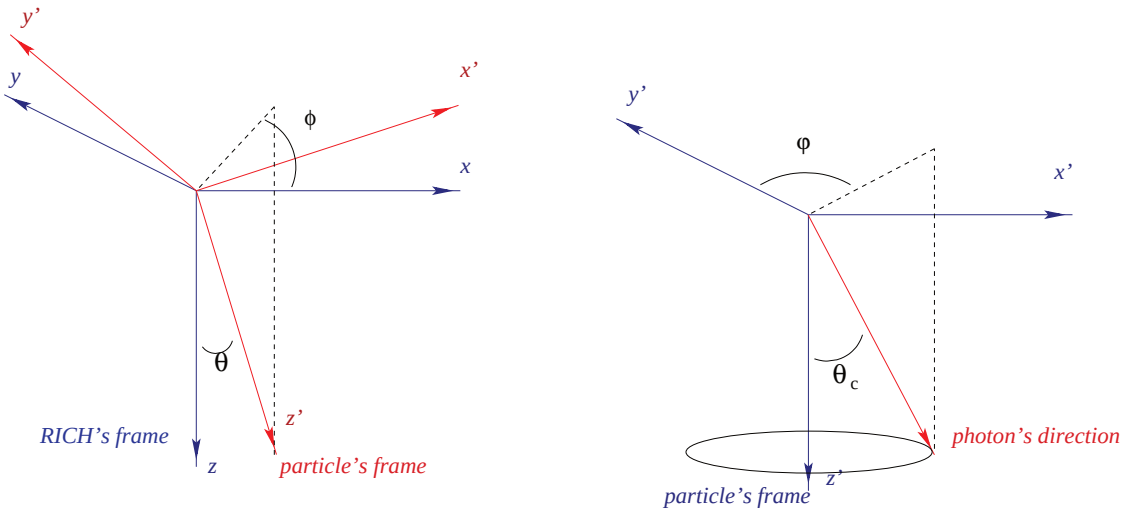

Figure 4.3: *Illustration of the two frames: particle's frame and detector's frame* (left). *Photon direction in the particle's frame* (right).

4.3 Photon Intersections

In the following paragraphs, the intersection points of the Čerenkov photons with each part of the RICH detector will be calculated. A intersection point, P(x,y,z), is given by the azimuthal angle, φ, of the photon that intersects the part of the detector in study.

4.3.1 Radiator intersections

In the radiator, the photon can either be absorbed at the lateral walls or suffer refraction at the basis or suffer total reflection, depending on its incident angle.

Photon intersection point with radiator lateral walls

It can occur absorption of the emitted photon in the lateral walls of the radiator since they aren't made of a reflective material. The φ of the intersection point can be easily found as being the solution of the intersection of the photon, with the cylindrical surface that represents the radiator surface (see Figure 4.4). The equation it should obey is the following:

$$(z-z_0)^2\left[\left(\frac{g_x}{g_z}\right)^2+\left(\frac{g_y}{g_z}\right)^2\right]+2(z-z_0)\left[x_0\frac{g_x}{g_z}+y_0\frac{g_y}{g_z}\right]+(x_0^2+y_0^2-\mathrm{Rt}_\mathrm{M}^2)=0, \tag{4.3}$$

where $\mathrm{Rt_M}$ is the top radius of the mirror. This equation is obeyed by each photon

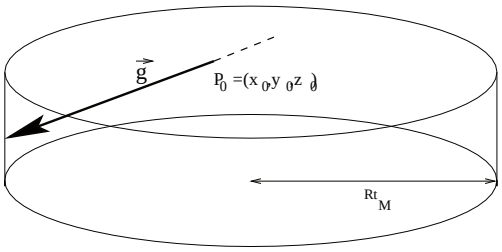

Figure 4.4: *Illustration of the intersection of the photon with the radiator lateral wall.*

that intersects the lateral walls of the radiator. From eq. 4.3, the photon azimuthal limits (φ) corresponding to the two points where the curve intersects the radiator bottom plane, are given by replacing z=$\mathrm{H_R}$.

Photon refraction at radiator boundary

According to the transformation 4.2, the photon's incident angle (θ_i) on the radiator bottom is obtained as:

$$\cos\theta_i=\sin\theta\sin\theta_c\cos\varphi+\cos\theta\cos\theta_c. \tag{4.4}$$

Full reflectivity of photons for radiator-air or radiator-foil and foil-air transitions will exist, depending on the incident angle and on the radiator's refractive index (n), i.e., if the condition $n \sin\theta_i > 1$ is fulfilled. Otherwise, (if $n \sin\theta_i < 1$), they will suffer refraction at the exit of the radiator at a point R, whose coordinates are given by $R(x, y, z) = P_0(x_0, y_0, z_0) + \frac{(\mathrm{H_R} - z_0)}{g_z}\vec{g}$ where $\mathrm{H_R}$ is the radiator height (see Figure 4.5).

The new photon's direction can be expressed in terms of the normal to the radiator plane pointing upward, $\vec{n} \equiv (0, 0, -1)$, and the incident direction $\vec{g}$:

$$\vec{g}_t = \frac{\sin\theta_t}{\sin\theta_i}\vec{g} + \frac{\sin(\theta_t - \theta_i)}{\sin\theta_i}\vec{n} = n\vec{g} + \frac{\sin(\theta_t - \theta_i)}{\sin\theta_i}\vec{n}, \tag{4.5}$$

where θ_t is the angle of the transmitted photon with respect to the normal and is obtained from Snell's law: $\sin\theta_t = n \sin\theta_i$.

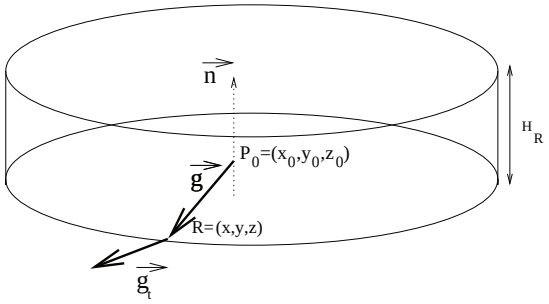

Figure 4.5: *Illustration of the intersection of the straight line defined by the photon's direction with the radiator basis.*

4.3.2 Photon reflection on the mirror

After refraction, photons can suffer reflections in the conical mirror wall. The reflected photon's direction can be expressed in terms of the normal to the mirror wall, $\vec{n}_m$, computed from the gradient of the conical surface and pointing inward and the photon incident direction $\vec{g}_t$,

$$\vec{g}_r = \vec{g}_t + 2\cos\theta_i \vec{n}_m. \tag{4.6}$$

Photon reflection will only happen for those photons which intersect the photomultiplier's plane (X) with a distance to the center greater than the mirror bottom

radius. This is also schematically represented in Figure 4.1. This distance can be easily computed from the coordinates of the intersection point, X which are given by:

$$X = R + \frac{\mathrm{H_M}}{g_{t_z}}\vec{g}_t, \tag{4.7}$$

where $\mathrm{H_M}$ is the mirror high.

Definition of the conical surface

The mirror can be described with a conical geometry which analytically means that it is represented by the following equation:

$$x^2 + y^2 - \tan^2\alpha(z - z_c)^2 = 0, \tag{4.8}$$

where α is the aperture of the cone and $(0, 0, z_c)$ are the coordinates of the vertex. The relevant geometrical parameters are represented in Figure 4.6.

According to the geometry, $\tan\alpha$ and z_c can be expressed as

$$\tan\alpha = \frac{\mathrm{Rb_M} - \mathrm{Rt_M}}{\mathrm{H_M}} \tag{4.9}$$

$$z_c = \frac{\mathrm{Rt_M} \times \mathrm{H_M}}{\mathrm{Rb_M} - \mathrm{Rt_M}} - \mathrm{H_R}. \tag{4.10}$$

Determination of the intersection point of the photon with the mirror

The required point is given by the intersection of the line

$$M(x, y, z) = R(x_r, y_r, z_r) + (z - z_r)/g_{tz}\vec{g}_t \tag{4.11}$$

with the conical surface. Therefore, the z-coordinates of each intersection point obey the following equation:

$$\begin{aligned}(z - z_r)^2 \left[\left(\frac{g_{tx}}{g_{tz}}\right)^2 + \left(\frac{g_{ty}}{g_{tz}}\right)^2 - \tan^2\alpha\right] + \\ 2(z - z_r)\left[\frac{g_{tx}}{g_{tz}}x_r + \frac{g_{tx}}{g_{tz}}y_r - \tan^2\alpha(z_r - z_c)\right] \\ - \tan^2\alpha(z_r - z_c)^2 + {x_r}^2 + {y_r}^2 = 0.\end{aligned} \tag{4.12}$$

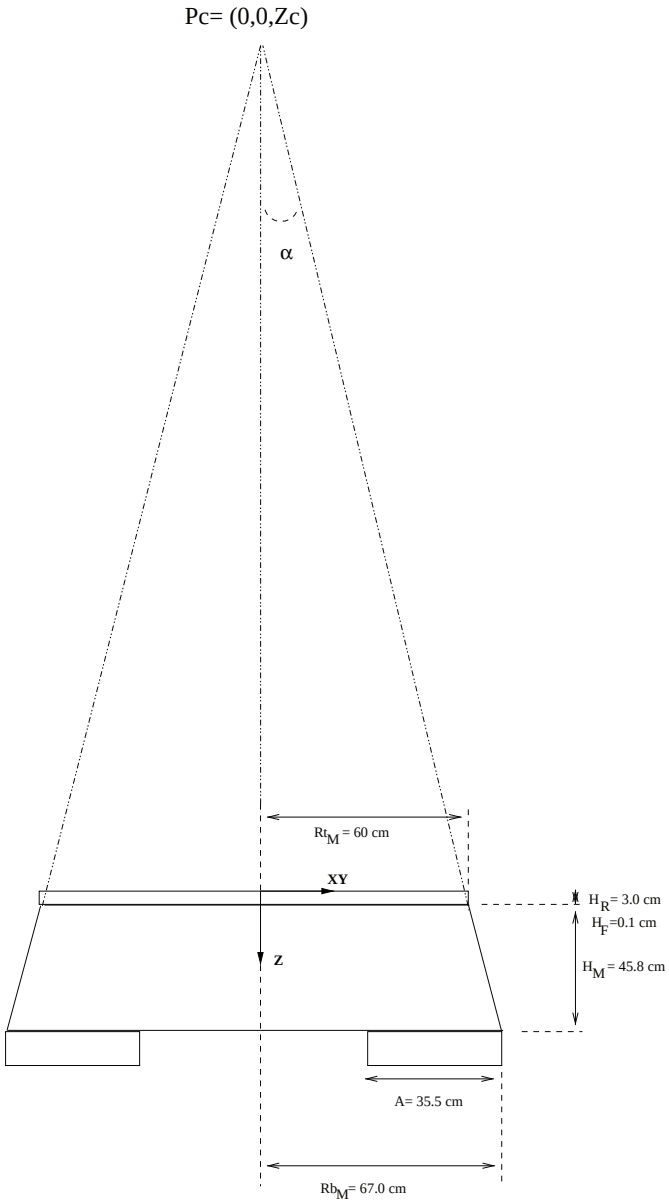

Figure 4.6: *Scheme with the geometry of the RICH detector and the corresponding geometrical parameters.*

The x and y coordinates are obtained from the expressions:

$$x = x_r + (\frac{g_{tx}}{g_{tz}})(z - z_r) \tag{4.13}$$

$$y = y_r + (\frac{g_{ty}}{g_{tz}})(z - z_r). \tag{4.14}$$

The azimuthal limits of the two extreme photons belonging to the Čerenkov cone that intersects the mirror are obtained by replacing the z-coordinate of intersection

by z=($H_R + H_M$), in the equation 4.12 and solving it. Another alternative is to find the solutions of the equation $x^2 + y^2 - Rb_M^2 = 0$.

4.3.3 Photon hitting the detection plane

At last, photons will either reach the PMTs at the detection plane, or will fall in the non-active regions of the matrix (the squared hole above the electromagnetic calorimeter (ECAL) and the gaps between PMT modules). For the geometry visualization see Figure 3.14. The coordinates of these points in the matrix are given by the intersection of the photon with the PMT plane. In order to identify if the photons are falling or not within an active area, the point coordinates x and y are compared to the limits of the active areas. Therefore, the boundaries of the detected photon pattern can be given in terms of the azimuthal angle φ.

4.4 Ring Acceptance Calculation

The Ring Acceptance measures the fraction of radiated photons that reach the photomultipliers matrix. It means the fraction of photons that:

- do not escape through the radiator lateral walls;
- are not totally reflected at the following interfaces: radiator-air, radiator-foil and foil-air;
- are not lost in the conical mirror (assumed 85% of reflectivity);
- do not fall in a non-active area of the detection plane (gaps in the PMTs, junctions or hole of the electromagnetic calorimeter).

Figure 4.7 shows a representation of the Čerenkov photon pattern generated by an incident particle, whose impact point in the radiator is (x,y) and direction is (θ,ϕ).

The photon pattern represented with a full line corresponds to the photons reaching directly the photomultipliers. Those photons which are reflected in the mirror produce a pattern represented by a dashed line. Finally, the photons which fall in non-active areas are represented by a dotted line.

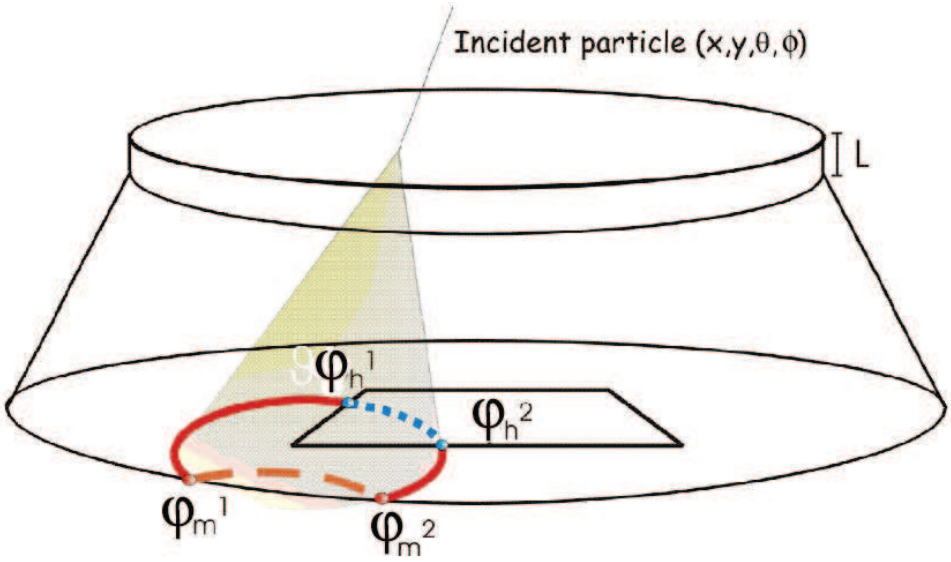

Figure 4.7: *3-dimensional view of photon pattern tracing in RICH detector, where φ_h^i are the limits of visibility of the Čerenkov pattern by intersection with the inactive detection region of the matrix and φ_m^i are the extreme intersection points of the Čerenkov pattern with the conical mirror.*

For a certain event, the photon ring acceptance is obtained by summing the different fractions of *visible* photons; namely, the fraction of photons hitting the PMTs matrix, directly (ε_{Dir}^{acc}), the fraction of incident photons in the mirror (ε_{Mir}^{acc}) weighted by the mirror reflectivity (ρ). Therefore the ring acceptance can be written as:

$$\varepsilon^{acc} = \varepsilon_{Dir}^{acc} + \rho\ \varepsilon_{Mir}^{acc} \tag{4.15}$$

Conversely, the ring *invisible* acceptance gives account of the fraction of photons lost in the calorimeter hole (ε_{Hol}^{acc}) and in the radiator interfaces.

Since Čerenkov photons are emitted isotropically in particle's reference frame the ε_{Dir}^{acc}, ε_{Hol}^{acc} and ε_{Mir}^{acc} are easily obtained by taking into account the differences between the azimuthal angles (φ) corresponding to the extreme intersection points of the Čerenkov cone with the non-active regions of the detector, φ_h, and with the mirror, φ_m.

$$\varepsilon_{Dir}^{acc} = \frac{|\varphi_m^1 - \varphi_h^1| + |\varphi_m^2 - \varphi_h^2|}{2\pi}; \varepsilon_{Mir}^{acc} = \frac{|\varphi_m^2 - \varphi_m^1|}{2\pi}; \varepsilon_{Hol}^{acc} = \frac{|\varphi_h^2 - \varphi_h^1|}{2\pi}. \tag{4.16}$$

4.5 Results

4.5.1 Events and its acceptances

The previous calculations where applied to several events and two of them are showed below in Figure 4.8. The aerogel event has a ring acceptance ε^{acc}=88.4%. The NaF event has a ring acceptance ε^{acc}=21.7%.

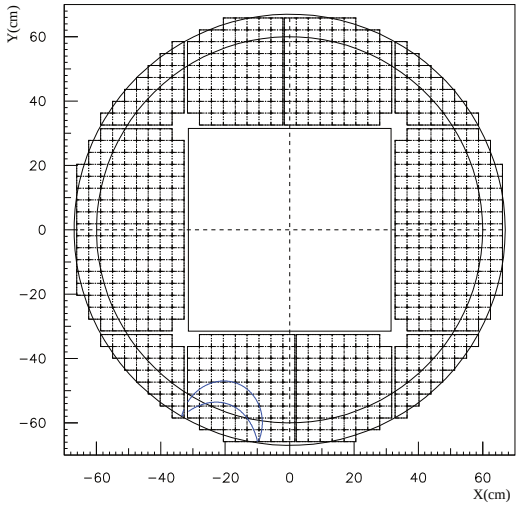

	ε^{acc}_{Dir}=0.535
Impact point=(-13.4;-39.0;0.0)	ε^{acc}_{Mir0}=0.410
$\theta = 23.1^o$ $\phi = 250.2$	ε^{acc}_{Mir1}=0.000
$\beta = 0.999$ $\theta_c = 13.63^o$	ε^{acc}_{Hol}=0.055
	ε^{acc}_{Inv}=0.055

Figure 4.8: *An event detected in the PMT matrix, generated in aerogel radiator, n=1.030, together with an expansion volume height of 45.8 cm. (ε^{acc}_{Mir0} refers to 1st order reflections and ε^{acc}_{Mir1} to more than one reflection, this is explained in Subsection 4.5.2.)*

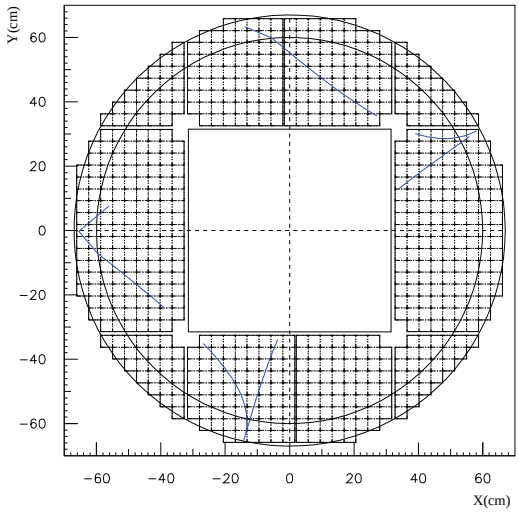

	ε^{acc}_{Dir}=0.120
Impact point=(27.1;-27.9;0.0)	ε^{acc}_{Mir0}=0.106
$\theta = 23.2^o$ $\phi = 324.9$	ε^{acc}_{Mir1}=0.008
$\beta = 0.999$ $\theta_c = 41.38^o$	ε^{acc}_{Hol}=0.169
	ε^{acc}_{Inv}=0.766

Figure 4.9: *An event detected in the PMT matrix, generated in sodium fluoride radiator, n=1.334, together with an expansion volume height of 45.8 cm. (ε^{acc}_{Mir0} refers to 1st order reflections and ε^{acc}_{Mir1} to more than one reflection, this is explained in Subsection 4.5.2.)*

4.5.2 Acceptances distributions

Based on the method described before, the various fractions of photons (acceptances) were computed for events generated in all the AMS acceptance and with a velocity close to the speed of light (β=0.999). Two different radiators, aerogel 1.030 and sodium fluoride were used together with an expansion volume height of 45.8 cm.

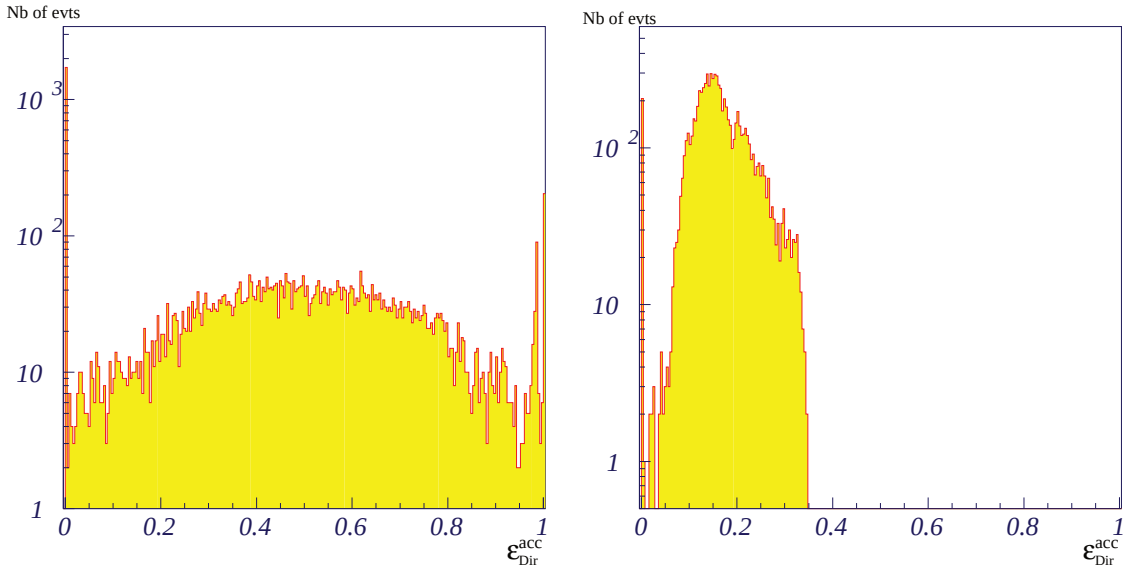

Figure 4.10: *Distributions of direct acceptance: for an aerogel radiator, n=1.030* (left)*; for a sodium fluoride radiator, n=1.334* (right)*; both setups with an expansion volume height of 45.8 cm. Particles generated in all the AMS acceptance, with β=0.999.*

Looking to the direct acceptance distribution (Figure 4.10) it is visible that aerogel has values ranging from 0 to 1, while sodium fluoride ends at 35%. This reflects not only the existence of a larger Čerenkov angle for NaF compared with aerogel (see left plot of Figure 3.7), but also the fact that a higher refractive index produces a larger refracted angle and consequently there are always photons leaving the NaF radiator with a wider angle, when compared with aerogel, that likely conducts them to the mirror.

The direct acceptance distribution, shows as well, for aerogel, a peak at 100% corresponding to events fully contained and that had not suffered any reflection. There are also events accumulated at 98%, which corresponds to fully contained patterns but with few lost photons in the module gaps.

There are events with no direct pattern in both direct acceptance distributions, for aerogel and NaF radiators. On aerogel, this corresponds either to events falling in the calorimeter hole or events fully reflected in the mirror. While on NaF, it corresponds to events where all the photons are either lost through the radiator lateral walls or totally reflected at the radiator transition. The amount of events with no direct acceptance is much more important on aerogel distribution than in NaF.

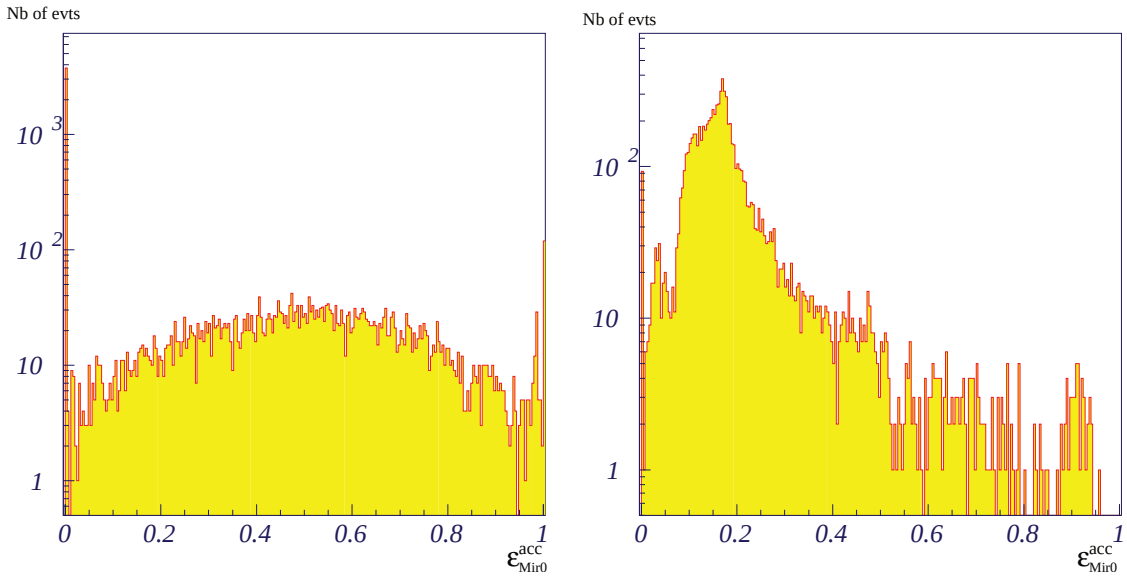

Figure 4.11: *Distributions of mirror acceptance computed from first reflection patterns in: an aerogel radiator, n=1.030* (left)*; a sodium fluoride radiator, n=1.334* (right)*; both setups with an expansion volume height of 45.8 cm. Particles generated in all the AMS acceptance, with β=0.999.*

Figure 4.11 presents the mirror ring acceptance distributions. The fraction of reflected photons in the mirror, in every event, depends strongly on the radiator kind. In aerogel, around 53% of the events have reflected photons, while for NaF, almost all the events (98%) have reflections. On the other hand, aerogel has a small amont of events (∼1.5%) fully reflected in the mirror while no event is seen in NaF. This still reflects the much larger Čerenkov angle with which photons are emitted in NaF.

Beyond the singly reflected photons, there can also be multiple reflections in the mirror. Such a photon scheme is shown in Figure 4.12. The distributions of the fraction of photons with more than one reflection are shown in Figure 4.13, for

aerogel and NaF radiators. Aerogel shows a negligible amount of events having multiple reflections, while NaF has events up to 20% of multiple reflected patterns.

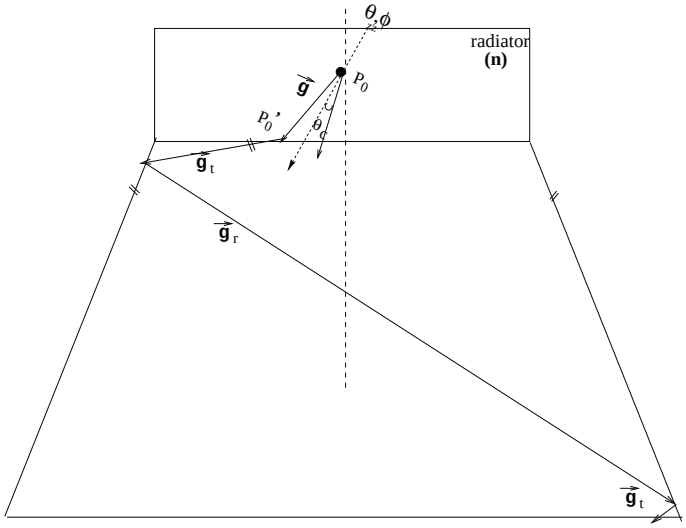

Figure 4.12: *Second reflection suffered by the photon. Situation verified mainly in the NaF radiator. Here, due to the higher refractive index, the θ_c reaches 41º, for particles with $\beta \sim 1$, so photons, after being reflected, have a high probability of reaching the other side of the mirror and suffer a second reflection (not drawn to scale).*

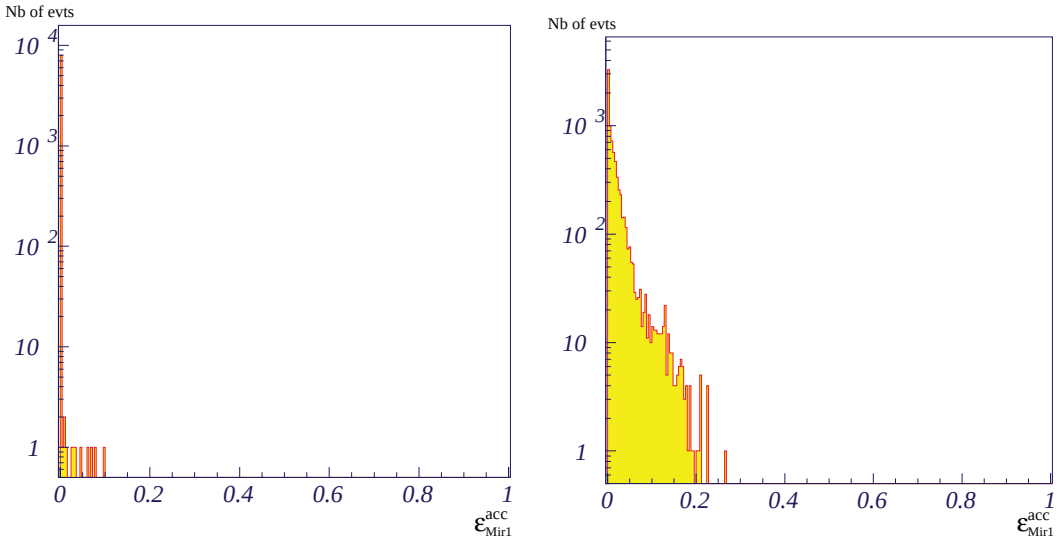

Figure 4.13: *Distribution of mirror acceptance computed from second reflection patterns for: an aerogel radiator n=1.030* (left)*; a sodium fluoride radiator, n=1.334* (right)*; both setups with an expansion volume height of 45.8 cm. Particles generated in all the AMS acceptance, with β=0.999.*

The fraction of photons falling in the calorimeter hole or generically being lost were also studied. Figure 4.14 and Figure 4.15 show the hole acceptance and the invisible acceptance distributions, that are closely related once the invisible acceptance includes the hole acceptance. As it was said before, the invisible acceptance takes also into account the photons lost before entering the expansion volume (radiator sides, total reflection).

For aerogel, there is a continuous range of ring acceptance values from 0 to 1 in both distributions, the same is not verified for NaF. For NaF, the maximum hole acceptance is nearly 60% and higher values are inexistent as a consequence of the larger rings. In NaF, the higher number of totally reflected photons and photons that escape through the lateral walls of the radiator, is notorious in the distribution of invisible acceptance, which is populated to higher values than the hole acceptance distribution. There are less than 1% of events with a pattern completely invisible in NaF, while in aerogel this value rises to 12%.

For the aerogel, 9% of the events fall completely in the hole. The peak at 100% of invisible acceptance includes the peak of 100% hole acceptance, in fact 75% of these events fall totally in the hole.

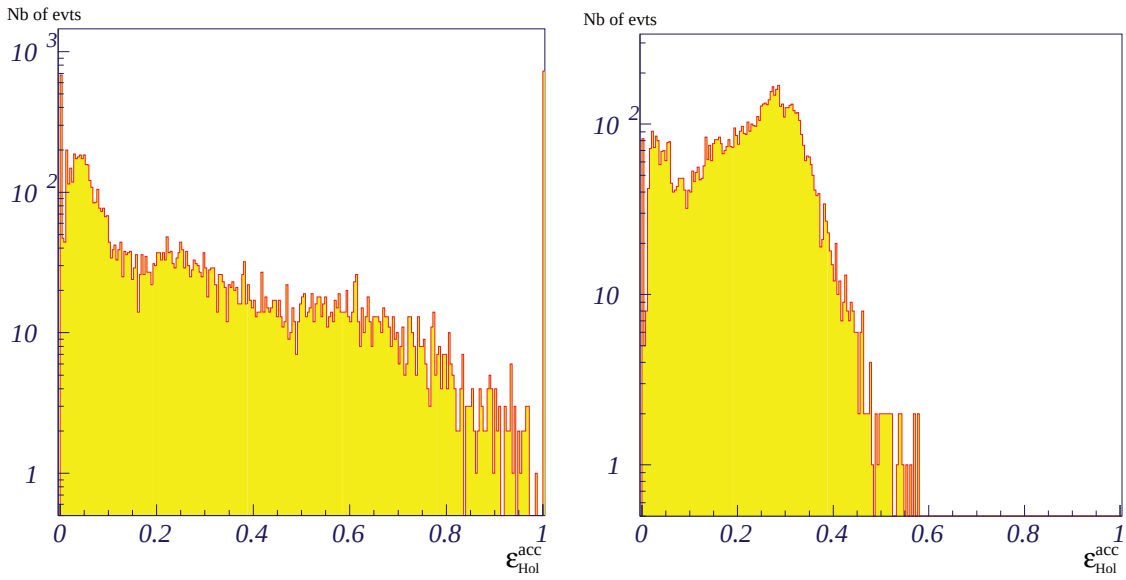

Figure 4.14: *Distribution of Hole Acceptance: for an aerogel radiator, n=1.030* (left)*; for a sodium fluoride radiator, n=1.334* (right)*; both setups with an expansion volume height of 45.8 cm. Particles generated in all the AMS acceptance, with β=0.999.*

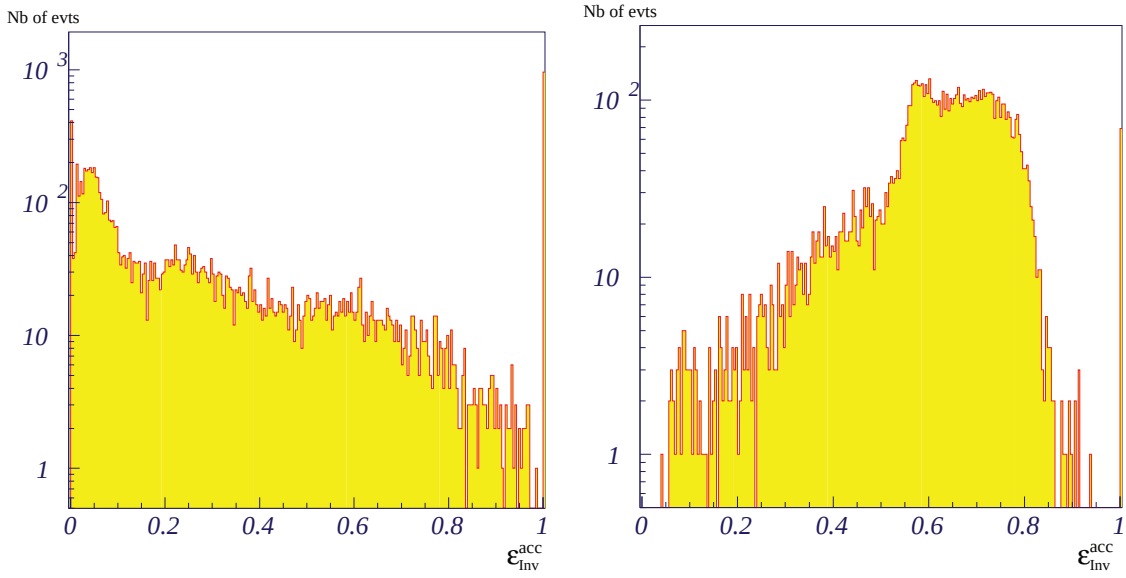

Figure 4.15: *Distribution of invisible acceptance: for an aerogel radiator, n=1.030* (left)*; for a sodium fluoride radiator, n=1.334* (right)*; both setups with an expansion volume height of 45.8 cm. Particles generated in all the AMS acceptance, with β=0.999.*

Finally are presented the photon ring acceptances (Figure 4.16) calculated as $\varepsilon_{Dir}^{acc} + \rho\ \varepsilon_{Mir}^{acc}$, with ρ=0.85.

For the aerogel, the peak at 100% represents the patterns fully contained in the matrix. As it was expected, this peak is populated with the same number of events as the corresponding peak in the direct acceptance distribution. There is a peak at 85% containing the events totally reflected. At 98% of ring acceptance, there is another peak corresponding to events almost all visible but with a portion in the module gaps. The percentage of invisible patterns is 12%, which is also explicit in the invisible acceptance distribution. 76% of the events with a null ring acceptance in aerogel are events with 100% of hole acceptance.

For NaF, a large fraction of events falls in the range from 20% to 40% and the maximum value reaches a value around 80%. The percentage of invisible patterns is less than 1%, which is agreement with the invisible acceptance distribution.

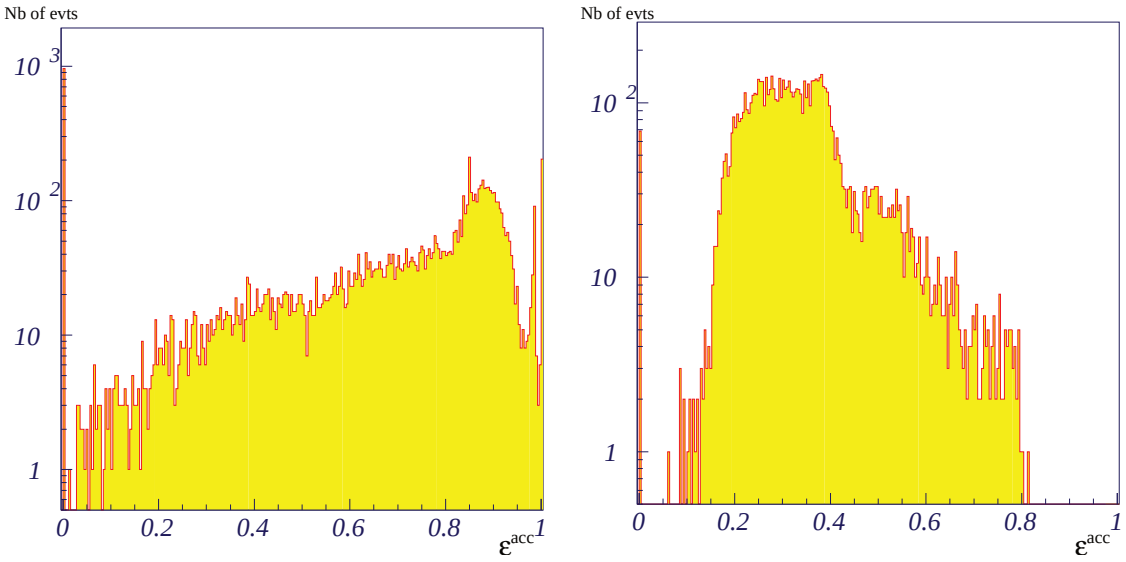

Figure 4.16: *Distribution of the photon ring acceptance given by* $\varepsilon^{acc}_{Dir} + \rho\ \varepsilon^{acc}_{Mir}$, *with* ρ=0.85: *for an aerogel radiator, n=1.030* (left)*; for a sodium fluoride radiator, n=1.334* (right)*; both setups with an expansion volume height of 45.8 cm. Particles generated in all the AMS acceptance, with* β=0.999.

4.5.3 Comparison with the simulation

To confirm the results of the analytical calculation for the ratio between the number of reflected photons and the number of detected photons, it was used the RICH simulation. There a photon generated in the radiator, interacts in the same radiator and is followed and registered, if detected by the photomultipliers. For every event, there were counted both the number of reflected photons absorbed and the total number of detected photons. Figure 4.17 compares the ratios between the number of reflected photons and the number of photons observed in the ring and the estimation based on the analytical calculation. There is a very good agreement between what is observed and calculated.

4.5.4 Applicability

This pattern tracing method is used in the θ_c reconstruction [5], briefly described in Section 3.5. In a RICH event, there are some hits detected which belong to a certain ring, characterized by a certain emission angle - Čerenkov angle (θ_c). The

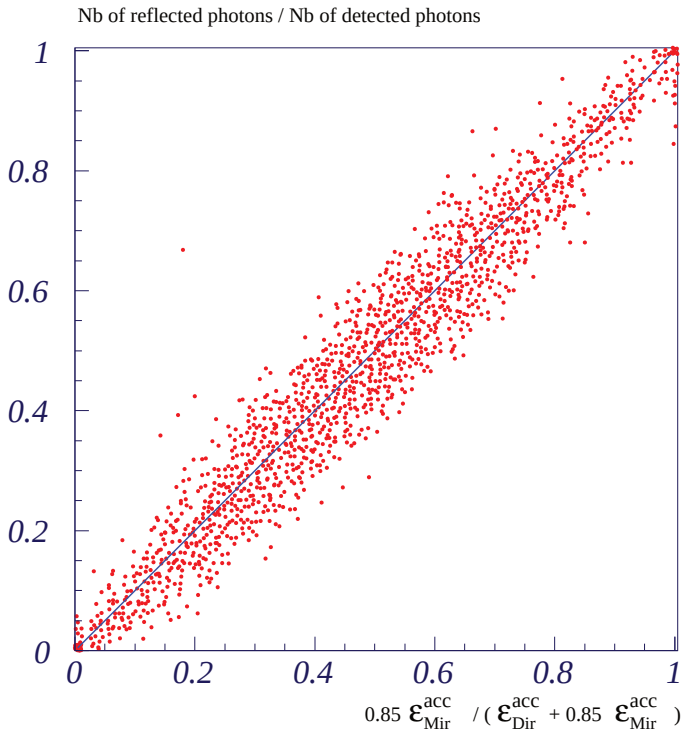

Figure 4.17: *Distribution of the ratio* $\frac{Nb\ of\ reflected\ \gamma's}{Nb\ of\ detected\ \gamma's}$ *obtained with a simulated event sample, versus the estimated ratio calculated through the expression* $\frac{\rho\varepsilon^{acc}_{Mir}}{\varepsilon^{acc}_{Dir}+\rho\varepsilon^{acc}_{Mir}}$, *with* ρ*= 0.85. The simulated sample corresponds to particles generated in all the AMS acceptance, with* β*=0.999, and crossing an aerogel radiator, n=1.030, together with an expansion volume height of 45.8 cm.*

reconstruction provides the best θ_c value which maximizes the probability of the hits belong to the expected ring. The pattern tracing developed, gives the knowledge of the expected ring for any hypothetical θ_c.

This is also applied to charge reconstruction [6], once here the method is based on the reconstruction of the total number of radiated Čerenkov photons obtained from integration of Equation 3.10 along all the particle's path and in all the energy range carried by the Čerenkov radiation:

$$Z^2 \propto \frac{N_\gamma^{radiated}}{\sin^2\theta_c}. \tag{4.17}$$

First it is necessary to do the counting of the number of photoelectrons, n_{pe}, close to the previously reconstructed photon pattern. The number of radiated photons is obtained by correcting the n_{pe} by the efficiency factors: ε_{rad}, that is the probability of a photon not to interact in the radiator material by Rayleigh scattering (in aero-

gel radiator) or absorption (both aerogel and sodium fluoride radiator), integrated along the radiator thickness and along the photon azimuthal angle φ; the photon ring acceptance accounts for photons lost through the radiator walls or totally reflected, photons absorbed by the mirror and photons that fall in the non-active zones of the matrix, here can be called ε_{geo}. It is also necessary to correct it with the light guide efficiency, ε_{lg}, and with the PMTs quantum efficiency, ε_{pmt}.

$$n_{pe} \sim N_{\gamma}^{radiated} \varepsilon_{rad} \varepsilon_{geo} \varepsilon_{lg} \varepsilon_{pmt} \tag{4.18}$$

It can also quantify eventual inefficient regions of the detector, such as a non-operational PMT or pixel.

Acceptances study also constitutes the basis of the radiator light yield mapping, where are identified the different regions of impact in the radiator, that combined with the different particle directions, originate patterns with a large or small acceptance (see Figure 5.3).

Chapter 5

Dual Radiator Configuration

5.1 Physical Motivations

The first design of the RICH detector included a solid low refractive index radiator made of aerogel tiles. The current aerogel characteristics elect an aerogel with a refractive index of 1.030 or 1.050, as described in Section 3.2.1. The detection of Čerenkov photons in the RICH is performed by a pixelized photomultiplier matrix, located 45.8 cm below the radiator. Constraints on the amount of heterogeneous matter in front of the downstream electromagnetic calorimeter, located below the detection matrix, made it necessary to reduce the readout area in the detection plane, decreasing considerably the photon detection efficiency for particles crossing the central radiator region. The implementation of a double radiator setup constituted by sodium fluoride (NaF), with a refractive index of 1.334, in the center and aerogel tiles surrounding the NaF, provides a larger acceptance and extends to lower values the particle momentum range covered. The extension of the RICH particle momentum range, overlapping with the TOF's, will impose further constraints on the propagation models of cosmic rays, based on the measurement of the ratios ^{3}He/^{4}He and ^{10}Be/^{9}Be.

A measurement of the isotopic composition of cosmic-ray beryllium nuclei will be extremely useful for determining the timescale for cosmic-ray escape (an estimative of τ_{esc}) and consequently the conditions of cosmic-ray propagation in the Galaxy, such as the average gas density of the ISM in the confinement region. Three isotopes

of beryllium are produced by nuclear fragmentation of heavy cosmic-ray particles: ^{7}Be, which only decays by electron capture (half life $\tau_{1/2}$=53 days), and consequently is stable in cosmic rays; ^{9}Be which is stable; and ^{10}Be, which is unstable to beta decay (β^{-}) with a half-life of 1.6 Myr [3].

AMS will be able to do an analysis of those isotopes from approximately 0.5 GeV/nucleon to 10 GeV/nucleon. This wide energetic range is mostly unexplored except for the low statistics data from SMILI-II and ISOMAX experiments. As can be seen from Table 5.1, for beryllium measurements, the data from SMILI-II extend up to 1.70 GeV/nucleon [57] and the data from ISOMAX extends up to 1.57 GeV/nucleon [58]. The use of a sodium fluoride radiator in the RICH of AMS will make it possible to cover the upper end of SMILI-II and ISOMAX data and accumulate a much larger statistics. The aerogel radiator will allow the coverage of higher energy values up to 10 GeV/nucleon, where the distinction between the predictions of the *Leaky Box* model and the *Diffusion* model is clearer [58].

Period	Experiment	Nb of Be evts	Energy Range (GeV/nucleon)	Moment. Range (GeV/nucleon)
1973-1974	IMP 7,8 [59]	906	0.031 - 0.151	0.250 - 0.570
1977-1991	Voyager 1,2 [60]	256	0.035 - 0.113	0.267 - 0.47
1978-1979	ISEE-3 [61]	345	0.060 - 0.185	0.352 - 0.650
1990-1997	Ulysses [62]	1525	0.068 - 0.135	0.375 - 0.537
1991	SMILI-II [57]	26	0.10 - 1.70	0.400 - 2.50
1997-1999	ACE [63]	6552	0.070 - 0.145	0.381 - 0.558
1998	ISOMAX [58]	91	0.64 - 1.57	1.27 - 1.91
2006-2009/11	AMS-RICH	$\sim 10^{7}$	$\sim$(0.5 - 8.3)	$\sim$(1.09 - 8.4)

Table 5.1: *Beryllium isotopic measurements. Data are taken from the given references.*

Figure 5.1 shows a collection of measurements of the isotopic ratios of ^{10}Be/^{9}Be made by different experiments. The prediction of the Strong & Moskalenko model [64], that provides the theoretical ratios based on the diffusive reacceleration, is also presented. The measurements obtained until now are insufficient and affected by large

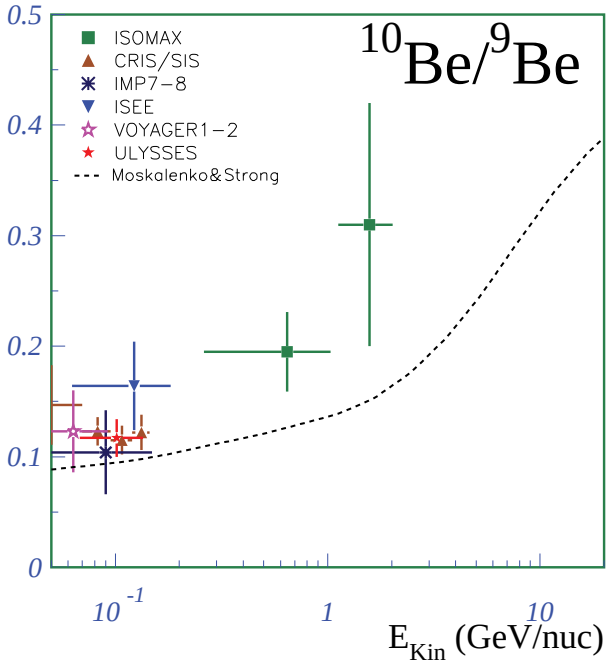

Figure 5.1: *Measurements of beryllium isotopic ratios ($^{10}Be/^{9}Be$) by different experiments: ISOMAX (Isotope Magnet Experiment)* [58], *CRIS (Cosmic-Ray Isotope Spectrometer)* [65], *IMP7-8* [59], *ISEE (International Sun-Earth Explorer 3)* [61], *Voyager1-2* [66], *Ulysses* [62]. *The prediction of the Strong & Moskalenko model* [64] *is also shown.*

errors, mainly due to statistical limitations. Once more it is visible that a double configuration of the RICH radiator will provide measurements in an unexplored region of energies with larger statistics.

^{3}He is a product of spallation of ^{4}He in the interstellar medium (ISM). Therefore, it can be used as a tracer to determine the mean matter path length of ^{4}He in the ISM and its energy spectra, particularly at low energies.

Table 5.2 shows the statistics of helium nuclei acquired by different experiments and their range of detection energies. The statistics of AMS will be higher than these reached until now, covering an extended energy region.

Period	Experiment	Nb of He evts	Energy Range (GeV/nucleon)	Moment. Range (GeV/nucleon)
1977	Voyager 1 [67]	1817	0.0076 - 0.069	0.12 - 0.37
1991	SMILI-II [57]	4899	0.1 - 1.7	0.40 - 2.50
1993-2002	BESS [68]	29937	0.2 - 1.0	0.64 - 1.70
1996	IMAX [69]	10390	0.2 - 3.7	0.64 - 4.54
2006-2009	AMS-RICH	$\sim 2 \times 10^9$	$\sim$(0.5 - 10.0)	$\sim$(1.09 - 9.10)

Table 5.2: *Helium isotopic measurements. Data are taken from the given references.*

Figure 5.2 shows the isotopic ratios of ^{3}He/^{4}He as function of the kinetic energy per nucleon measured by some of the previous experiments. The larger energy reached was 4.9 GeV/nucleon. The prediction of the Seo model [64], a reacceleration model, is also shown. Although there are more measurements than in beryllium experiments, there are still insufficient statistics visible from the large error bars.

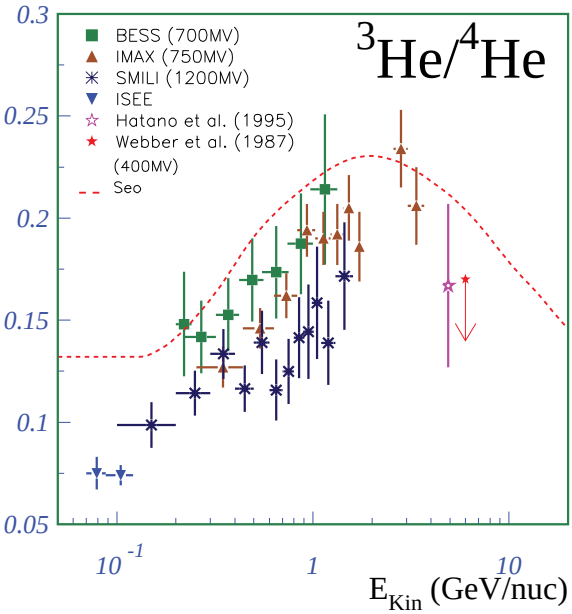

Figure 5.2: *Measurements of helium isotopic ratios (^{3}He/^{4}He) by different experiments: BESS (Balloon Borne Experiment with a Superconducting Solenoid Spectrometer)* [68], *IMAX (Isotope Magnet Experiment)* [69], *SMILI (Superconducting Magnet Instrument for Light Isotopes)* [70], *ISEE (International Sun-Earth Explorer 3)* [71] *and by Hatano* [72] *and Webber* [73] *experiments. The prediction of the Seo model* [74] *is also shown.*

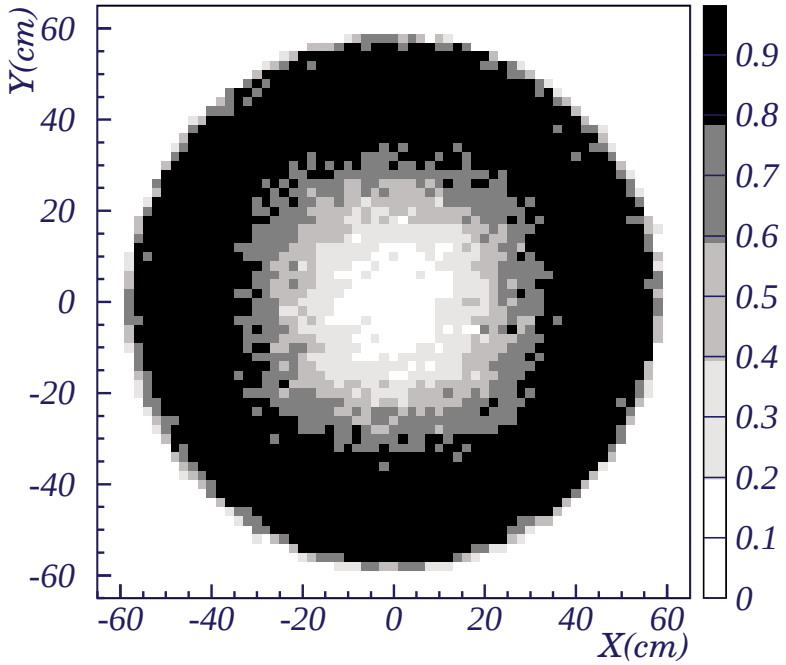

Figure 5.3: *Distribution of the Čerenkov ring acceptance as function of the the coordinates of the particle impact point in the 1.030 aerogel radiator, for a set of events simulated within RICH acceptance.*

5.2 Simple Aerogel Radiator

5.2.1 Photon ring acceptances with aerogel

A set of events crossing the RICH detector were simulated within the AMS acceptance, for the case of an aerogel radiator with a refractive index of 1.030, a thickness of 3 cm, and for an expansion volume height of 45.8 cm. The average ring acceptance was calculated for each event and is represented as function of the X and Y coordinates of the particle impact point in the radiator, in Figure 5.3. Events passing close to the radiator center, have low photon ring acceptances since most of radiated photons fall within the non-active detection region.

Particles reaching the radiator within 15 cm of its center have ring acceptances lower than 20%. Moving on from the radiator center, the ring acceptance increases. Close to the radiator borders, the photon ring acceptance decreases again due to the photons escaping through the radiator edges.

5.2.2 Event reconstruction efficiencies using an aerogel radiator

The reconstruction of events with a small number of hits in the PMT matrix, due to low ring acceptance and/or low Z can be critical, given the request of at least three hits for velocity reconstruction. This can be seen in Figure 5.4, where a proton left only one hit in the PMT matrix.

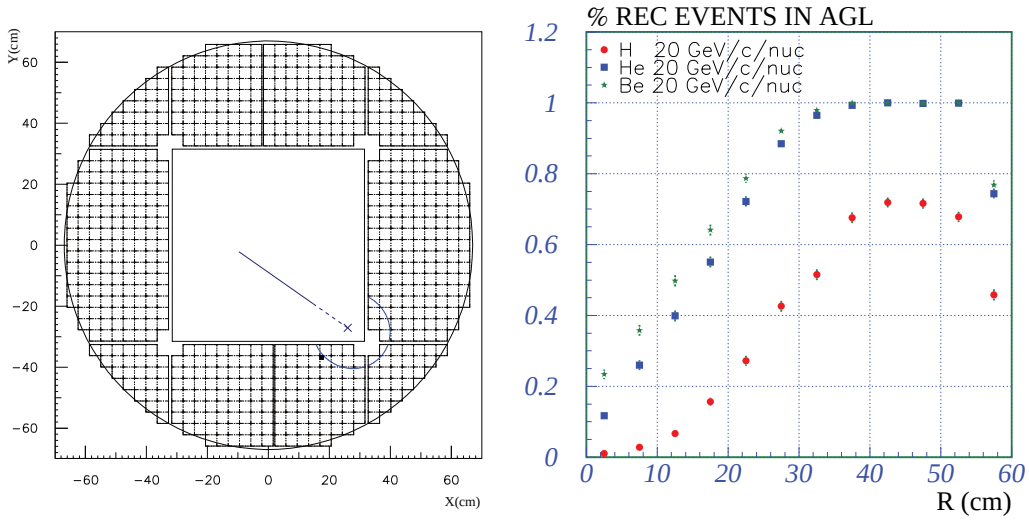

Figure 5.4: *RICH event display of a proton pattern partially falling in the hole, with only one hit (this is for an aerogel radiator, n=1.030, 3 cm thick)* (left).
Čerenkov angle reconstruction efficiency for 20 GeV/c/nucleon protons, heliums and berylliums as function of the particle impact radius in the aerogel radiator (n=1.030, 3 cm thick) (right).

On the right, in Figure 5.4, the reconstruction efficiency for protons, heliums and berylliums of 20 GeV/c/nucleon is shown as function of the impact radius on the radiator. This is the reconstruction efficiency expected using the three hits criterion for a n=1.030 aerogel radiator, 3 cm thick. The reconstruction efficiency is less then 10% for protons impacting closer than 15 cm to the center of the radiator. For heavier nuclei, in the same incidence region, the reconstruction efficiency reaches 50%, since the number of hits scales roughly with Z^2.

5.3 Dual Radiator Configuration

The geometrical acceptance in the region close to the radiator center can be increased by replacing the central aerogel tiles by a radiator with a higher refractive index. This idea was proposed for the first time in reference [75], using sodium fluoride (NaF) as a radiator.

Particles crossing a NaF radiator of n=1.334 will radiate photons with a Čerenkov angle, $\theta_c \sim 42^o$ for $\beta \sim 1$, whereas for the 1.030 refractive index aerogel the corresponding Čerenkov angle is of $\sim 12^o$. Given the wider Čerenkov cone in NaF, the fraction of photons falling in the inactive detection region is minimized. This is illustrated in Figure 5.5, where the Čerenkov patterns produced in NaF and aerogel are represented for a particle reaching the radiator top at (X,Y)=(-3,-4) cm with a polar angle of $\theta \sim 20^o$, the mean polar angle for the RICH acceptance. Using aerogel, all the Čerenkov ring would be contained in the ECAL hole while for NaF the ring acceptance achieved is of 26% (17% for the direct portion of the pattern and 11% for the reflected one, assuming a mirror reflectivity of 0.85).

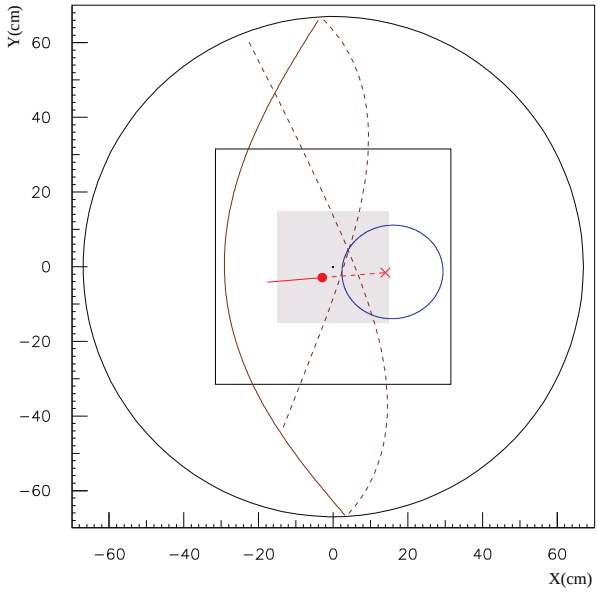

Figure 5.5: *Top view of the double radiator configuration. A NaF radiator is placed in the central region* (shaded region). *The particle track for a* central event *is also represented. On top of it, the symbols* • *and* × *indicate the positions at the radiator top level and at the detection matrix level, respectively. In the NaF case, direct photons* (full line) *and reflected photons* (dotted line) *are present.*

5.3.1 Comparison between the geometrical ring acceptances of aerogel and sodium fluoride

As it was shown in topic 4.5.2, Agl and NaF have different geometrical ring acceptance distributions. A set of events was simulated through the RICH detector and their geometrical acceptances calculated. It was calculated an average ring acceptance for the different polar angles (θ) and azimuthal angles (ϕ) of the particles, impacting within a given radius. Figure 5.6 shows the calculated acceptance for events passing in an aerogel radiator (left) and in a sodium fluoride radiator (right).

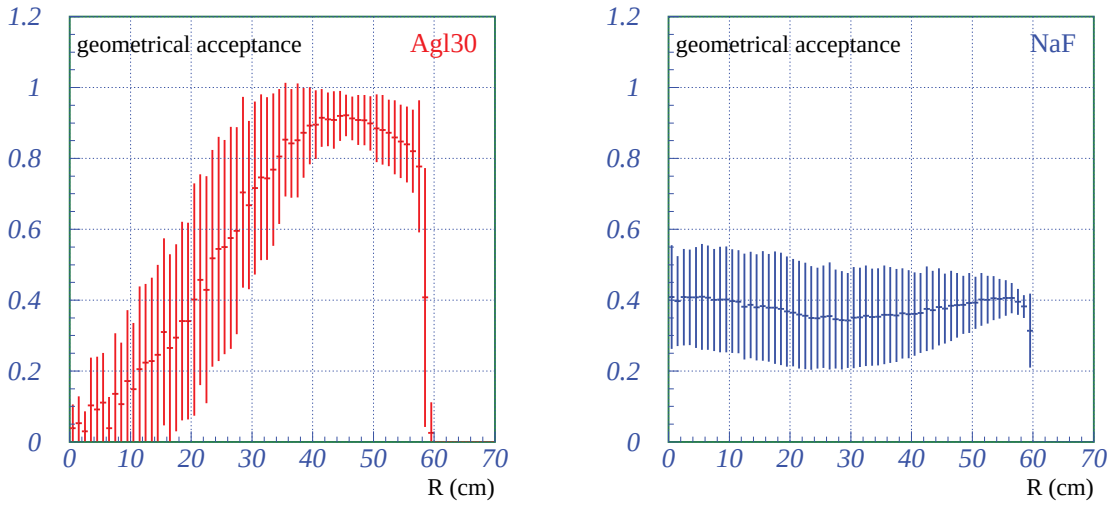

Figure 5.6: *Average ring acceptance for events crossing an aerogel* (left) *and NaF* (right) *radiator as function of the particle impact radius.*

The spread accounts for the variation of the acceptance within a certain radius. The fraction of Čerenkov photons detected for small impact radius is higher for NaF and remains in average essentially constant and around 40%, while for aerogel it increases with the radius, decreasing for impact radius greater than 50 cm, corresponding to events leaving the sides of the radiator. The small values of the average geometrical acceptance are associated with events that typically fall in the ECAL hole.

5.3.2 Dimensions of the sodium fluoride radiator

The study of the reconstruction efficiencies using NaF and Agl radiators, as function of the particle impact radius, can be a guide in the choice of the NaF dimension.

The reconstruction efficiencies depend on the number of radiated photons (a function of the radiator thickness), on their interactions inside the radiator (which depend on the aerogel clarity coefficient, see Subsection 3.2.1) and on the geometrical acceptance for each event.

A minimal number of 3 hits is required for velocity reconstruction. The ratio of events reconstructed in NaF to those reconstructed in aerogel, as function of the incident particle distance to the radiator center, is presented in Figure 5.7 for protons, helium and beryllium nuclei. The NaF and aerogel radiator thicknesses used were 0.5 cm and 3 cm, respectively.

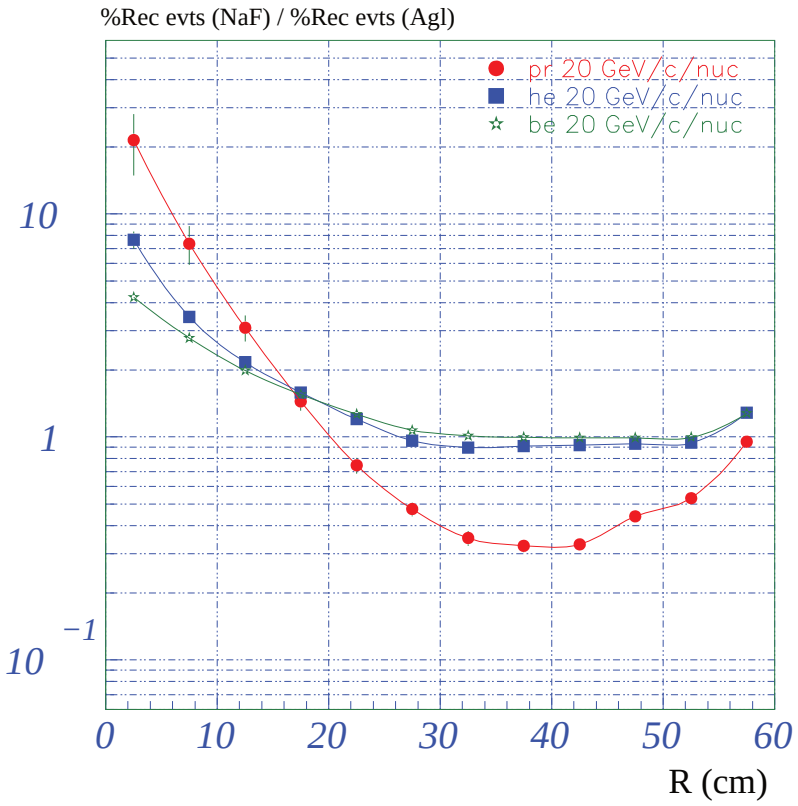

Figure 5.7: *Ratio of reconstructed efficiencies in NaF and aerogel for 0.5 cm and 3 cm of radiator thickness, respectively, as function of the particle impact radius.*

For the three types of nuclei the number of reconstructions using the NaF radiator

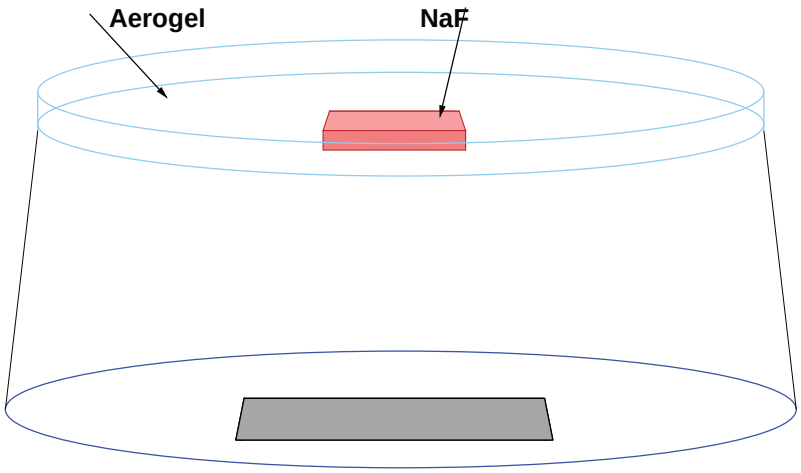

Figure 5.8: *Dual radiator configuration.*

dominates up to a particle impact radius of about 20 cm. Above this distance, the numbers of reconstructed helium and beryllium nuclei are of the same magnitude for both materials. For protons the ratio decreases because of the three hits requirement.

If the NaF radiator thickness were increased, the ratio of reconstructed proton events would rise independently of the impact radius, while for heavier nuclei the ratio is not affected since there are enough hits (≥ 3) to perform the velocity reconstruction. However, an increase on the NaF radiator thickness would increase the weight of the radiator and the amount of matter crossed by the particles, originating more energy losses.

Therefore, the proposed configuration for the RICH radiator shown in Figure 5.8 will include a basic low refractive index solid material together with a high refractive index solid radiator in the center. The former being made of 1.030 refractive index, 3 cm thick aerogel tiles, and the latter consisting of a square of sodium fluoride (NaF) of 1.334 refractive index, with a side length of 34.5 cm and a thickness of 0.5 cm. The size of the sodium fluoride radiator square was chosen to fit the side length of three aerogel tiles (11.5 cm each), in the center of the radiator.

The geometrical acceptance covered by the sodium fluoride, can be easily calculated. Assuming that particles are uniformly impacting on the radiator, the number of particles per unit area is $\frac{dN}{dA} = K$. The number of particles falling in a circular

region of radius r is given by:

$$N(r) = \int \frac{dN}{dA} dA = \int K r dr d\theta = \pi K r^2. \tag{5.1}$$

Therefore, the fraction of particles falling within the region of radius r, is:

$$f(r) \equiv \frac{N(r)}{N(R)} = \frac{\pi K r^2}{\pi K R^2} = \left(\frac{r}{R}\right)^2, \tag{5.2}$$

where R is the radius of the full radiator. The fraction of particles falling inside a square of size ℓ is given by:

$$f(l) = \frac{1}{\pi}\left(\frac{l}{R}\right)^2. \tag{5.3}$$

According to expression 5.3, the number of particles seen within a square with a side length of 34.5 cm is computed to be 11% of the total number of particles crossing the RICH radiator. This is also visible from comparing the distribution of the polar angle of the particles crossing the central square and the polar angle distribution for all particles within the RICH acceptance, both represented in Figure 5.9.

Keeping the amount of matter in front of the electromagnetic calorimeter as small as possible was one of the goals in mind for the dual radiator configuration. Table 5.3 provides some characteristics for aerogel and NaF.

Material	*Refractive index*	*Light transparency*	*Density* (g/cm^3)	*Radiation Length* X_0 (cm)
Aerogel	1.030	L_{scatt} ∼3.5 cm for λ=400 nm (clarity coefficient∼ 0.0074 $\mu m^4 cm^{-1}$; for the sample in study) L_{absor} ∼100 cm (negligible absorption)	0.120	136.0
NaF	1.334	$L_{scatt} \sim \infty$ (negligible clarity coefficient) (negligible scattering) L_{absor} ∼15 cm for λ=400 nm	2.558	11.68

Table 5.3: *Some characteristics of aerogel and NaF (L_{scatt} is the scattering interaction length and L_{absor} is the absorption length)* [8].

The presence of a sodium fluoride radiator in the way of a particle contributes with 4.6% of radiation length, while aerogel contributes with 2.3%. From the point of view of the weight of the detector, a critical point in objects to be sent to the space, the sodium fluoride will contribute with 1.5 Kg, while the aerogel occupying the same space had a weight of 0.4 Kg.

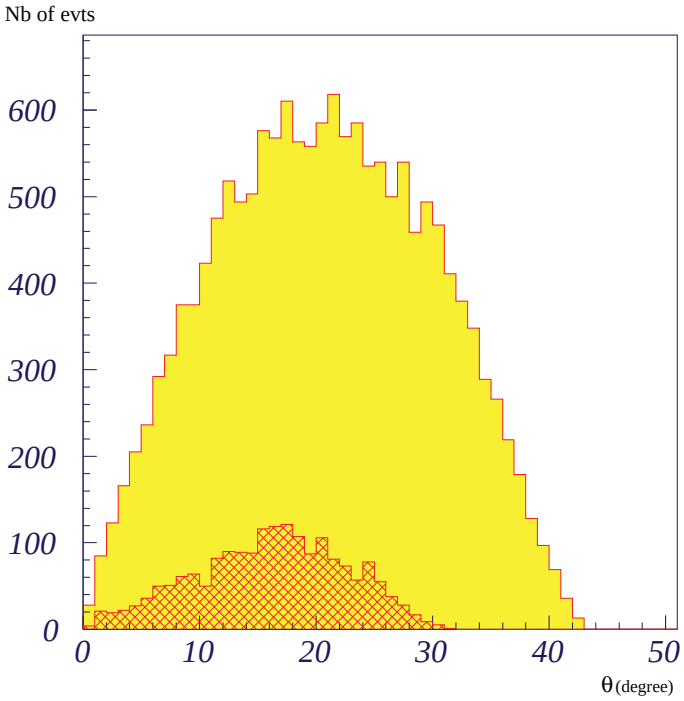

Figure 5.9: *The NaF square, placed at the center, covers 11% of the RICH acceptance. The RICH accepted polar angles are represented in the continuos region and the accepted polar angles in the central square of 34.5 cm side length are in the shaded region.*

5.3.3 Comparison between the reconstruction efficiency of aerogel and sodium fluoride

Sets of events with different momenta and crossing a central radiator square with a typical size of $30\times30\,\mathrm{cm}^2$ were simulated both for NaF, 0.5 cm thick and Agl (1.030), 3 cm thick. The reconstruction efficiencies for both simulated sets, based on the 3 hits criterion, are compared in Figure 5.10. For the whole momentum range, the reconstruction efficiency for the NaF radiator is higher than for the aerogel. The maximum efficiency value increases with the charge, as the number of detected hits increases. For protons, the reconstruction efficiency in NaF is twice the aerogel's, reaching 20%. It reaches 85% and ∼100% for helium nuclei and beryllium nuclei, respectively.

It is notable that using a NaF radiator will extend the kinetic energy range covered by the RICH detector, down to values around 0.5 GeV/nucleon, due to its lower Čerenkov threshold. This enables the detection of isotopes with a kinetic

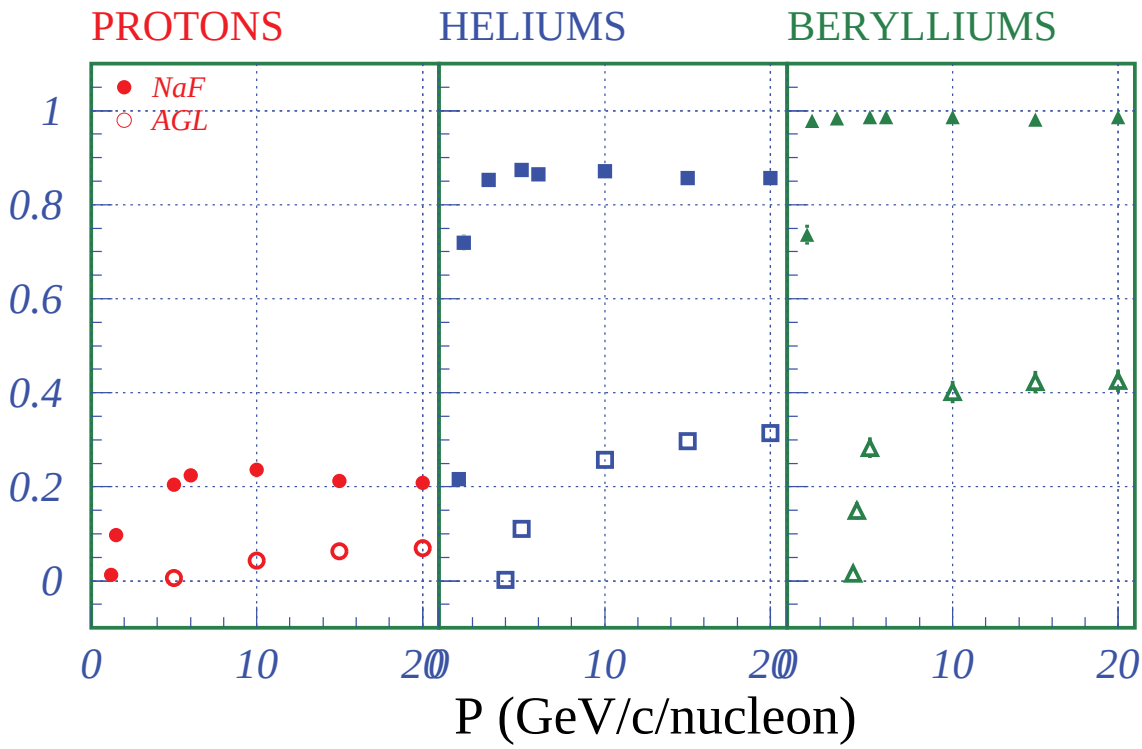

Figure 5.10: *Reconstruction efficiency versus the momentum per nucleon for different nuclear charges and for the two studied radiators for a central squared region of 30×30 cm^2.*

energy within a larger range than the one of a simple aerogel radiator.

Next the different factors involved in the quality of the Čerenkov angle reconstruction will be discussed in a qualitative way for both radiator materials.

5.3.4 Velocity measurement accuracy

The accuracy of the velocity measurement made with the RICH depends on the accuracy of the Čerenkov angle reconstruction. Aerogel and sodium fluoride show intrinsically different sensitivities to the Čerenkov angle as is explicit in the following relation derived from the Čerenkov angle relation 3.2:

$$\frac{\Delta\beta}{\beta} = \tan\theta_c \Delta\theta_c. \tag{5.4}$$

The uncertainty in θ_c deals with:

- pixel size of PMT readout matrix;

- radiator thickness;
- chromaticity.

Consequently the θ_c uncertainty is given by:

$$\Delta\theta_c = \Delta\theta_c^{pixel} \oplus \Delta\theta_c^{thick} \oplus \Delta\theta_c^{chrom} = \Delta\theta_c^{geom} \oplus \Delta\theta_c^{chrom}; \tag{5.5}$$

where $\Delta\theta_c^{geom}$ accounts for the uncertainty sources of geometrical nature (pixel size and radiator thickness) and $\Delta\theta_c^{chrom}$ accounts for the intrinsic chromaticity.

As a first appoximation the Čerenkov angle uncertainty estimation can be obtained from particles with $\beta \sim 1$ inciding perpendicularly on the detector and neglecting refraction at the radiator transition. The photon ring width detected can be related to the photon arm (d) and to the effective ring width (ΔR_{eff}) through:

$$\tan(\Delta\theta_c) \sim \frac{\Delta R_{eff}}{d} \sim \frac{\Delta R \cos\theta_c}{H/\cos\theta_c} = \cos^2\theta_c \frac{\Delta R}{H}. \tag{5.6}$$

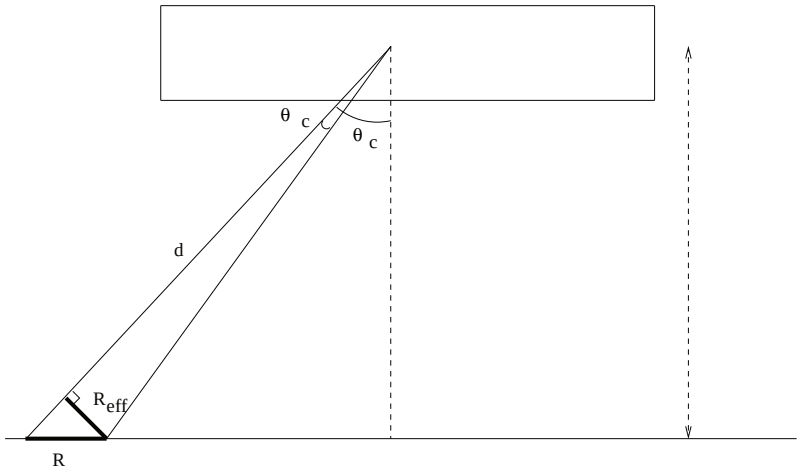

Figure 5.11: *Uncertainty of the reconstructed θ_c due to the photon ring width uncertainty.*

Given the small uncertainty in θ_c ($\Delta\theta_c \ll 1$), the error on the Čerenkov angle is obtained,

$$\Delta\theta_c \sim \cos^2\theta_c \frac{\Delta R}{H}. \tag{5.7}$$

Pixel Size

The pixel granularity (8.5 mm), brings an error to the measurement of the hits coordinates used in the reconstruction of the ring, consequently the Čerenkov angle is also affected. The pixel size contribution to the geometrical error is taken as being the previous value divided by the factor $\sqrt{12}$, characteristic of the uniform probability density function (p.d.f), giving a contribution of 2.5 mm. However what has interest is the effective pixel size, in the sense that it corresponds to the pixel size seen in the photon's direction. This is the pixel size affected by $\cos\theta_c$, a factor that also affects the previous error. In NaF there are photons hitting the pixels with greater incident angles than in aerogel, consequently the effective pixel size is lower is NaF (6.4 mm) than in aerogel (8.3 mm). The photon arm (d) is longer in NaF than in aerogel, which also means a smaller contribution to the θ_c uncertainty reconstructed in NaF than in aerogel. These estimatives are the upper limit contributions from pixel size since refraction is being neglected. If it were considered, the photon arm would even be greater and consequently the Čerenkov angle uncertainty would be inferior.

Radiator Thickness

In the NaF case the radiator thickness is smaller (0.5 cm) than in aerogel (3 cm) which means a smaller contribution to the ring width. For a vertical incidence (see Figure 3.6) of a particle with $\beta \sim 1$ the ring width obtained for a 3 cm thick, 1.030 aerogel radiator is 0.74 cm, while for a 0.5 cm thick sodium fluoride radiator the ring width obtained with the same particle is of 0.44 cm.

Chromaticity Dispersion

Any refractive index is characterized by a chromatic dispersion law, which means that the refractive index depends on the wavelength λ of the photons that cross the medium, according to a relation $n(\lambda)$. Consequently for θ_c comes:

$$\cos(\theta_c) = \frac{1}{\beta n(\lambda)}. \tag{5.8}$$

As a result there is a dispersion from the expected value of θ_c calculated using the reference value for n. This is more remarkable for the NaF radiator than for

Agl, as it is shown in Figure 5.12.

$$\begin{aligned} \Delta\theta_c &= \frac{1}{\tan\theta_c}\frac{\Delta n}{n} \\ &= \frac{1}{\sqrt{(n\beta)^2-1}}\frac{\Delta n}{n}. \end{aligned} \tag{5.9}$$

According to the expression 5.9, for a particle with $\beta \sim 1$ crossing the NaF radiator, the dominant factor producing a larger chromatic effect in the emitted photons in NaF is $\frac{\Delta n}{n}$, since θ_c would be higher than in aerogel for the same β. In fact from Figure 5.13 the variation amplitude of the refractive index in NaF is $\Delta n \sim 0.024$ (right), nearly 10 times greater than in the aerogel case (left), that is $\Delta n \sim 0.0027$. For $\beta \sim 1$, in aerogel $\theta_c \sim 13.86^o$ and in NaF $\theta_c \sim 41.4^o$, which conjugated with previous factor, brings a factor of 1.8 for $\Delta\theta_c$ higher in NaF than in aerogel, observed in the width of the range of $\Delta\theta_c$ values covered in the plots of Figure 5.12.

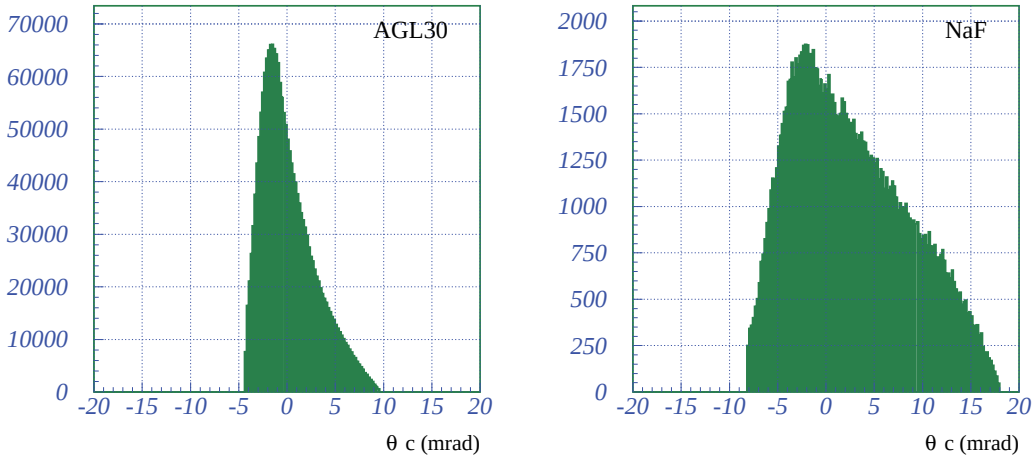

Figure 5.12: *Uncertainty of the reconstructed θ_c due to the chromaticity effect for an Agl radiator* (left) *and for one of NaF* (right) [5]. *Reconstruction for particles with $\beta \sim 1$.*

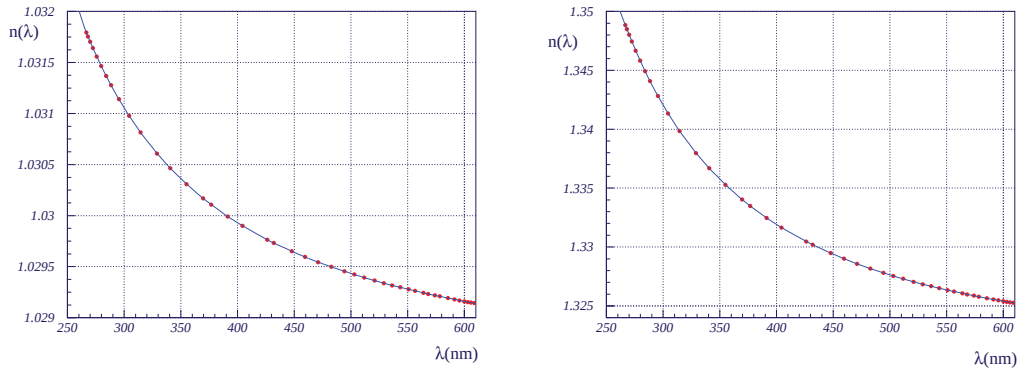

Figure 5.13: *Chromatic dispersion, used in simulation, in the Agl radiator* (left) *and in the NaF radiator* (right).

As the Čerenkov reconstructed angle is a sort of average on the individual reconstructions based on each detected photon of the Čerenkov pattern, the final error will be lower than the single hit contribution. Having N_{hits} detected on the reconstructed pattern, the expected resolution of the θ_c calculated for a pattern with N_{hits} scales from the single hit resolution as:

$$\Delta\theta_c = \frac{\Delta\theta_c(\text{single hit})}{\sqrt{N_{\text{hits}}}} \tag{5.10}$$

At radiator level, the Čerenkov signal, related to the number of hits, depends on the refractive index of the radiator and on the interactions with the media (scattering for aerogel and absorption for sodium fluoride). It is also dependent on the ring geometrical acceptance, on the light guide efficiency and on the PMT quantum efficiency. The distributions of the number of hits associated to a reconstructed pattern generated by helium nuclei of 10 GeV/c/nucleon are shown in Figure 5.14 for events passing through the aerogel and NaF radiators. In average, the number of hits obtained in aerogel is larger than in NaF.

The single hit resolution is estimated by multiplying the factor $\sqrt{N_{hits}}$ by the variable $\Delta\theta_c = \theta_c^{rec} - \theta_c^{exp}$, in order to deconvolve from the total resolution the number of hits. This is because for any random variable the error on the determination of its average scales with the number of used measurements (N), according to the factor $\frac{1}{\sqrt{N}}$.

The single hit θ_c resolutions for helium nuclei 10 GeV/c/nucleon are shown in dis-

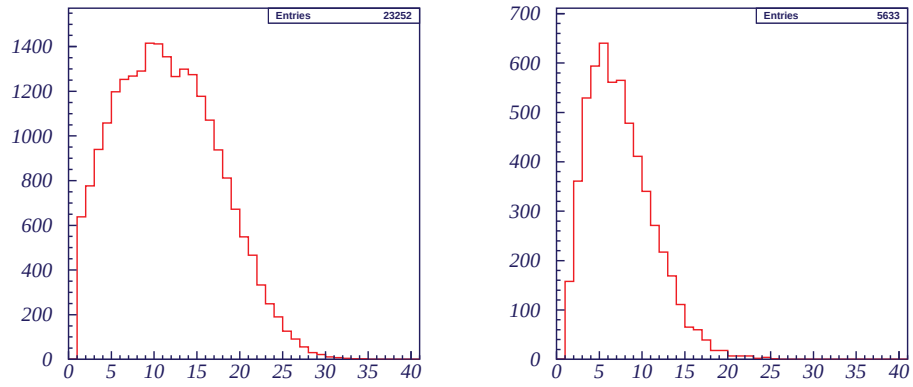

Figure 5.14: *Number of hits on the reconstructed pattern generated by helium nuclei, 10 GeV/c/nucleon (counting criterion: hits with residuals $< 4\sigma$ of the residuals Gaussian signal distribution): generated in aerogel 1.030, 3 cm thick* (left) *and in the NaF radiator 0.5 cm* (right).

tributions of Figure 5.15. These plots give the intrinsic resolution for each radiator. The single hit resolution in aerogel is 7.7 mrad and in NaF is 8.7 mrad.

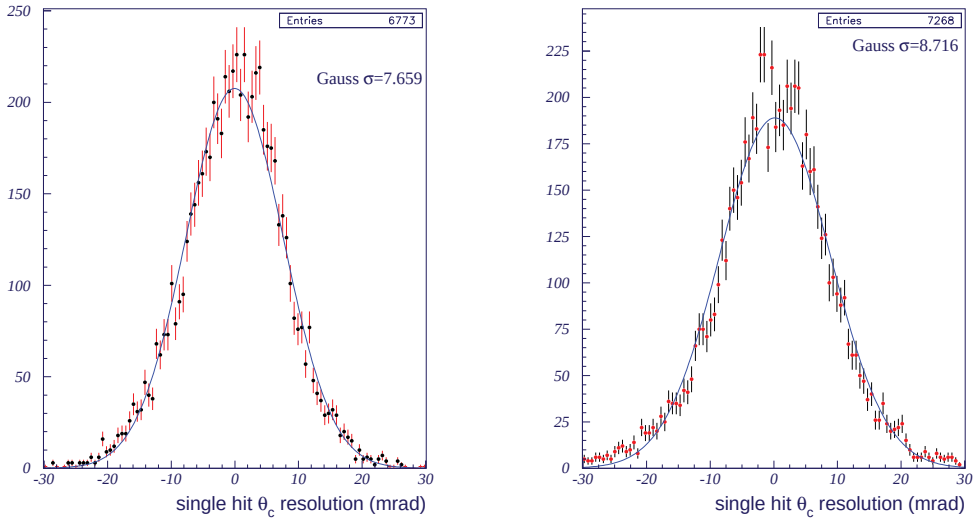

Figure 5.15: *Single hit θ_c resolutions for helium nuclei, 10 GeV/c/nucleon in aerogel 1.030, 3 cm thick* (left) *and in NaF, 0.5 cm thick* (right). *The scale is in miliradian.*

The velocity resolution is given by:

$$\frac{\Delta\beta}{\beta} = \tan\theta_c \frac{\Delta\theta_c(\text{single hit})}{\sqrt{N_{\text{hits}}}} = \frac{\frac{\Delta\beta(\text{single hit})}{\beta}}{\sqrt{N_{\text{hits}}}}. \tag{5.11}$$

In Figure 5.16 are shown the evolution of the single hit velocity reconstruction resolution in NaF and Agl radiators as function of the momentum per nucleon. The asymptotic values for the velocity single hit resolution are 0.2% and 0.7%, respectively for Agl and NaF.

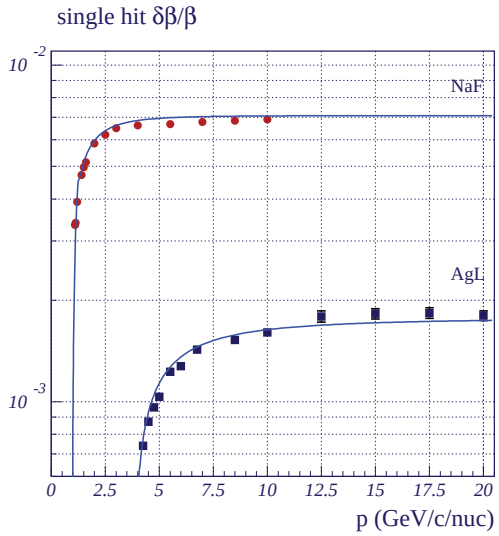

Figure 5.16: *Single hit velocity resolution for NaF and Agl.*

From eq. 5.11, it is estimated for the velocity resolution on the reconstruction of the helium nuclei 10 GeV/c/nucleon, crossing the aerogel radiator and the NaF radiator, 0.4×10^{-3} and 3.0×10^{-3}, respectively.

5.4 Summary

A possible dual configuration for the RICH detector radiator was studied. The optimal setup found consists of a central square of sodium fluoride (NaF) with a side length of 34.5 cm and a thickness of 0.5 cm, surrounded by aerogel 1.030.

Among the important implications of the proposed setup, there is not only the increment on the acceptances resulting on larger reconstruction efficiencies, but also the extension of the kinetic energy range covered by the RICH detector, down to values around 0.5 GeV/nucleon, due to the lower Čerenkov threshold for NaF. This enables the detection of isotopes with a kinetic energy within a larger range than

that of a simple aerogel radiator. This issue will be explored in the next chapter.

Chapter 6

Isotopic Element Separation

Isotopic separation and particularly the ratios ^{3}He/^{4}He and ^{10}Be/^{9}Be is a major part of the physics goals where the RICH plays a fundamental role within AMS. The presence of a mixed radiator with a NaF radiator at the center will allow AMS to cover a kinematic energy range from 0.5 GeV/nucleon up to around 10 GeV/nucleon.

6.1 Simulation of Helium and Beryllium Isotopes

Samples of helium and beryllium nuclei corresponding to 1 day and 1 year of data taking, respectively, were simulated[1]. The statistics of the simulated samples are shown in Table 6.1.

	Helium		*Beryllium*	
	^{3}He	^{4}He	^{9}Be	^{10}Be
Statistics	3.4×10^5	1.7×10^6	7.0×10^5	1.5×10^5
Obs Time	1 day	1 day	1 year	1 year

Table 6.1: *Helium and beryllium nuclei simulated statistics.*

These were generated according to a kinetic energy spectrum obtained from Seo model [74] for helium nuclei and Strong & Moskalenko model [64], for beryllium nuclei.

[1]The simulation was done by the Madrid group at CIEMAT (Centro de Investigaciones Energeticas Medioambientales y Tecnologicas)

The nuclei fluxes were simulated assuming the following:

- the particles were required to fall within the RICH acceptance;
- a solar modulation of 1000 MV;
- the geomagnetic field modulation of the nuclei energy with the ISS location was taken to be identical for different isotope species.

The fluxes were simulated assuming an uniform logarithmic kinetic energy scale from 0.1 GeV/nucleon up to 100 GeV/nucleon. The values for the simulated ratios are represented in Figure 6.1, which corresponds to the number of events shown in Figure 6.2, for helium and beryllium nuclei.

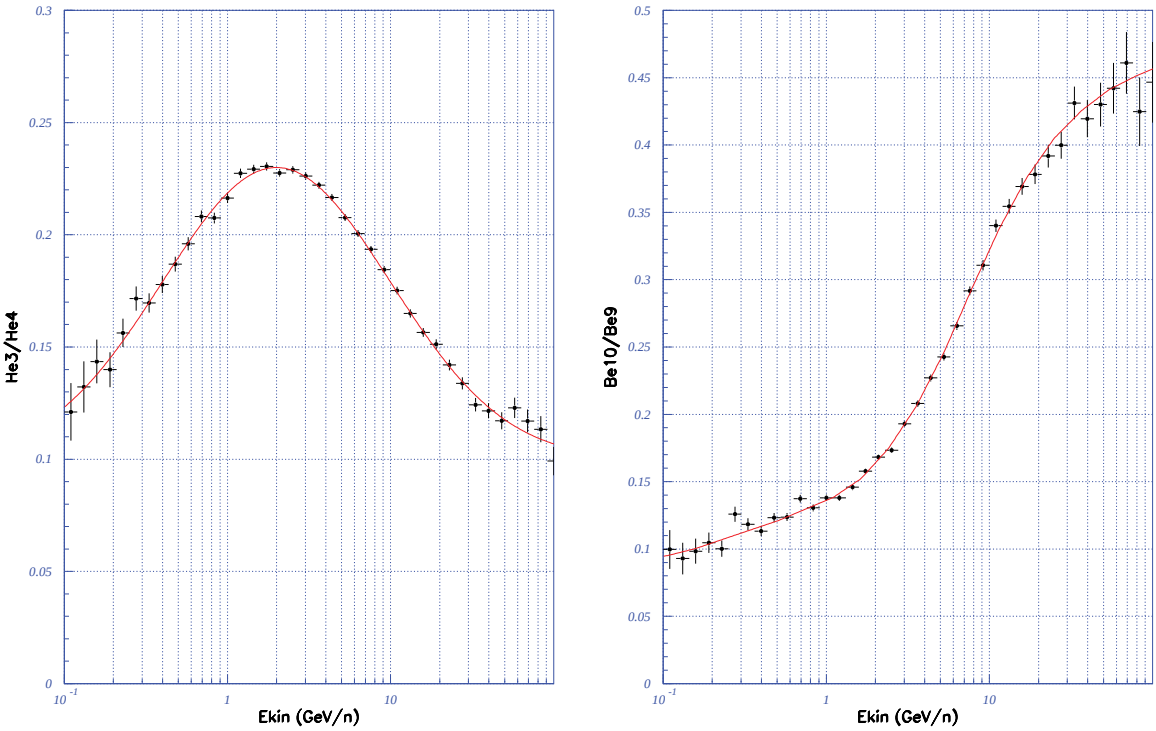

Figure 6.1: *$^{3}He/^{4}He$* (left) *and $^{10}Be/^{9}Be$* (right) *ratios in the kinetic energy range from 0.1 GeV/nucleon up to 100 GeV/nucleon, according to Seo* [74] *and Strong & Moskalenko models* [64], *respectively.*

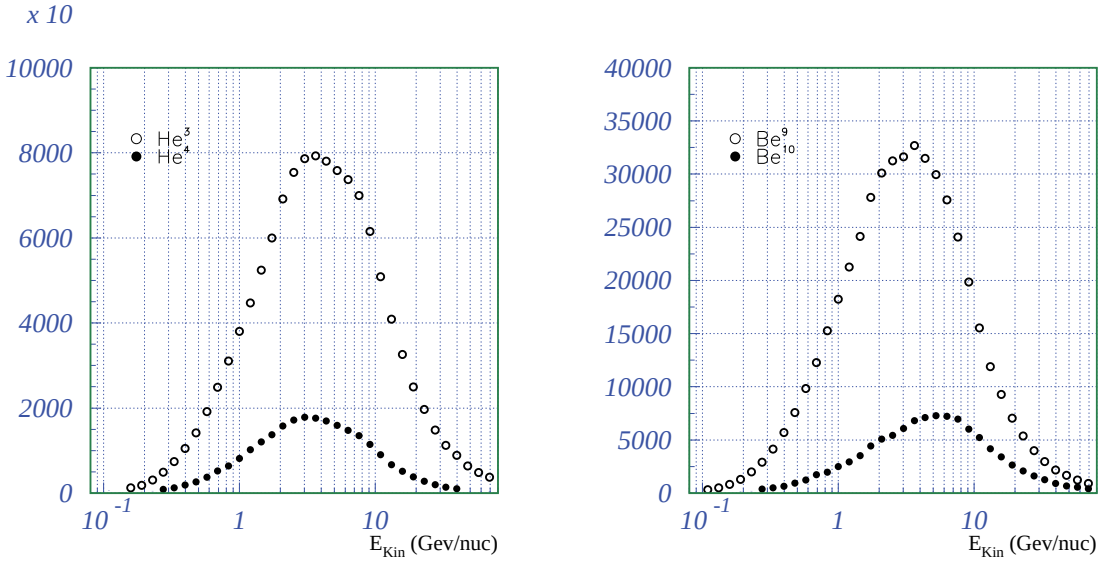

Figure 6.2: *Fluxes of* ^3He *and* ^4He (left)*;* ^{10}Be *and* ^9Be (right) *in the kinetic energy range from 0.1 GeV/nucleon up to 100 GeV/nucleon, according to Seo* [74] *and Strong & Moskalenko models* [64]*, respectively.*

6.2 Mass Fit

Event masses were reconstructed taking into account the velocity reconstruction made with the RICH and the tracker momentum measurement whose uncertainty is of $\sim 2\%$ for the energy region in study.

The reconstructed masses were fitted with a sum of two Gaussian functions:

$$f(m) = \frac{N_1}{\sigma_1\sqrt{2\pi}} \exp\left(-\frac{1}{2}\left(\frac{m-M_1}{\sigma_1}\right)^2\right) + \frac{N_2}{\sigma_2\sqrt{2\pi}} \exp\left(-\frac{1}{2}\left(\frac{m-M_2}{\sigma_2}\right)^2\right), \quad (6.1)$$

where N_i, σ_i and M_i are respectively the number of events for each isotope, its mass width and the central mass value.

The number of fit parameters can be varied from six to four, depending whether the two mass central values and uncertainty relations are constrained.

The reconstructed mass has an uncertainty which is related to the velocity and momentum uncertainties through the following relation:

$$\frac{\sigma_i}{M_i} = \gamma^2 \frac{\Delta\beta}{\beta} \oplus \frac{\Delta p}{p}, \qquad i = 1, 2; \quad (6.2)$$

Therefore, the constraint relative to the isotope mass uncertainties is given by:

$$\frac{\sigma_1}{M_1} = \frac{\sigma_2}{M_2} \Leftrightarrow \sigma_1 = \frac{M_1}{M_2}\sigma_2, \tag{6.3}$$

allowing to reduce the mass fit to five parameters. The isotope masses have been allowed to vary freely.

Figure 6.3 shows the mass relative uncertainties for ^{3}He and ^{4}He isotopes in terms of the kinetic energy per nucleon T_{rec}. This kinetic energy is calculated from the reconstructed velocity by:

$$T_{rec} = m(\gamma_{rec} - 1), \tag{6.4}$$

where m is the nucleon mass. The resolution obtained in the mass reconstructions is approximately the same for both isotopes.

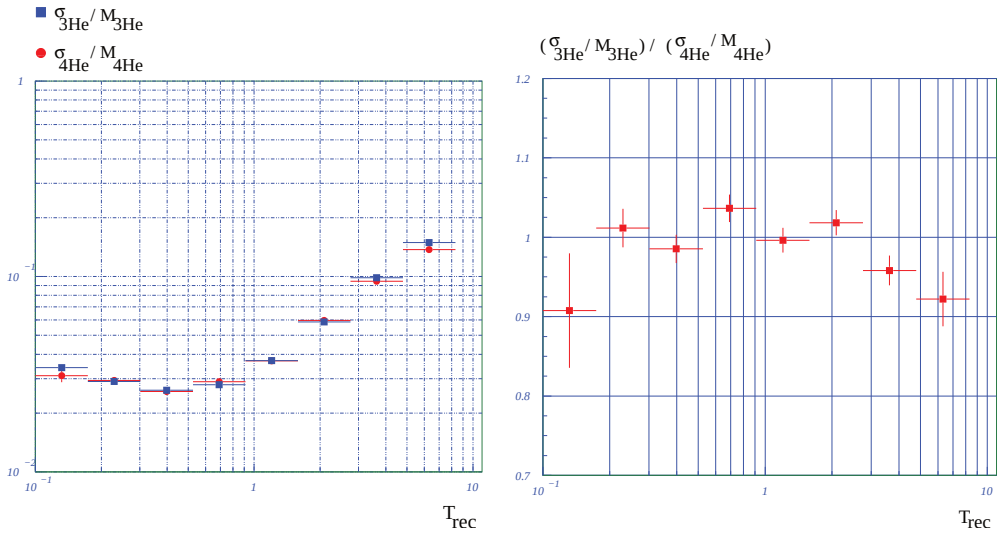

Figure 6.3: *Constancy of the mass resolution for both isotopes* (left). *The ratio of the mass resolutions is around 1* (right).

6.3 The Effect of the Plastic Foil below the NaF Radiator

The effect of introducing or excluding an acrylic plastic foil, with a thickness of 1 mm and a refractive index of 1.49, below the sodium fluoride radiator in the mass reconstruction was studied using helium and beryllium nuclei.

The presence of this foil a source of additional photons radiated with a different Čerenkov angle.

In Figure 6.4, the simulated kinetic energy is represented as a function of the reconstructed kinetic energy, including the plastic foil (left) and suppressing it (right), both for helium and beryllium nuclei. In the case of the reconstructions in the presence of the plastic foil, there are events distributed near the threshold energy bin reconstructed with a higher kinetic energy than the simulated one.

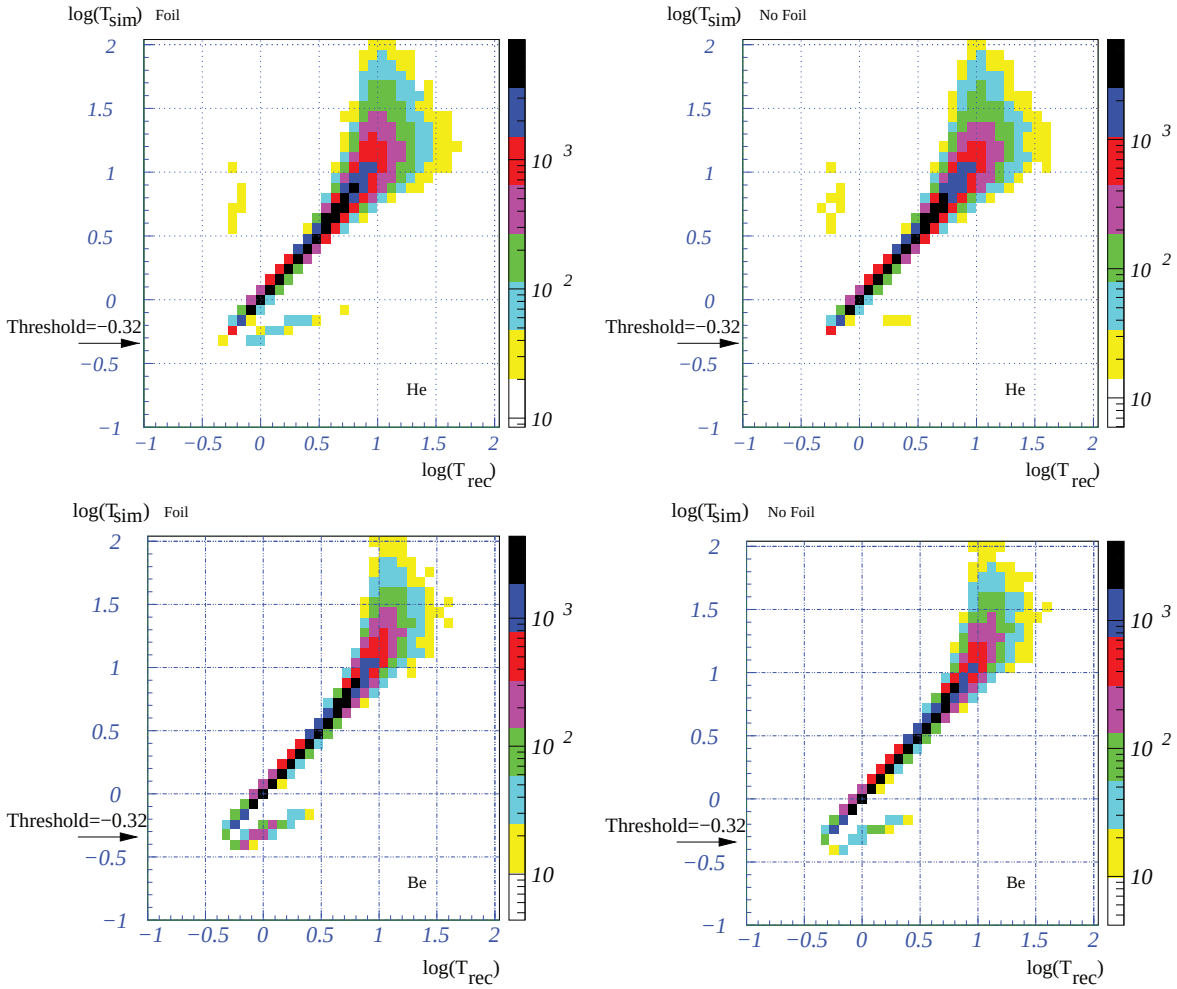

Figure 6.4: *Occupancy of reconstructed events using a* **NaF** *radiator according to the kinetic energy simulated and the kinetic energy reconstructed: with foil, 1 mm thick,* (left)*; without foil* (right)*. Helium nuclei* (top)*; beryllium nuclei* (bottom)*.*

That is a notorious migration effect which is highly suggestive of reconstructions using hits originating from the foil. In fact, this energy region is near the NaF threshold where not only few hits are radiated but also the Čerenkov angle is small. A small Čerenkov angle implies a higher number of events with a lower ring accep-

tance due to the probability of photons, totally or partially, fall in the ECAL. As a consequence there will be less NaF events obeying the 3 hits criterion established for accepting the velocity reconstructions (see method described in Section 3.5). On the other hand the foil material has a refractive index of 1.49, which translates into a kinetic energy threshold lower than that of NaF (T_{th}=0.48 GeV/nucleon), $T_{sim} \sim 0.33$ GeV/nucleon. Reconstructions of the Čerenkov angle using hits from foil radiated photons but assuming the NaF refractive index will produce wider reconstructed angles, and higher velocity values than those expected. These reconstructions will appear with a reconstructed kinetic energy larger than the simulated.

The elimination of the foil causes the disappearance of the migration effect in a large fraction of events.

For aerogel the presence of the plastic foil will be discussed in Subsection 6.4.2.

6.4 Isotopic Mass Reconstructions

6.4.1 ^{3}He/^{4}He separation

Figure 6.5 shows the reconstructed masses for helium events passing through the NaF radiator, for different kinetic energy ranges with and without foil.

A peak of events from fake reconstructions made with hits from photons radiated in the plastic foil can be observed below the true mass peaks. It peaks at certain mass values depending on the particle energy. Removing the foil the referred region is cleaned.

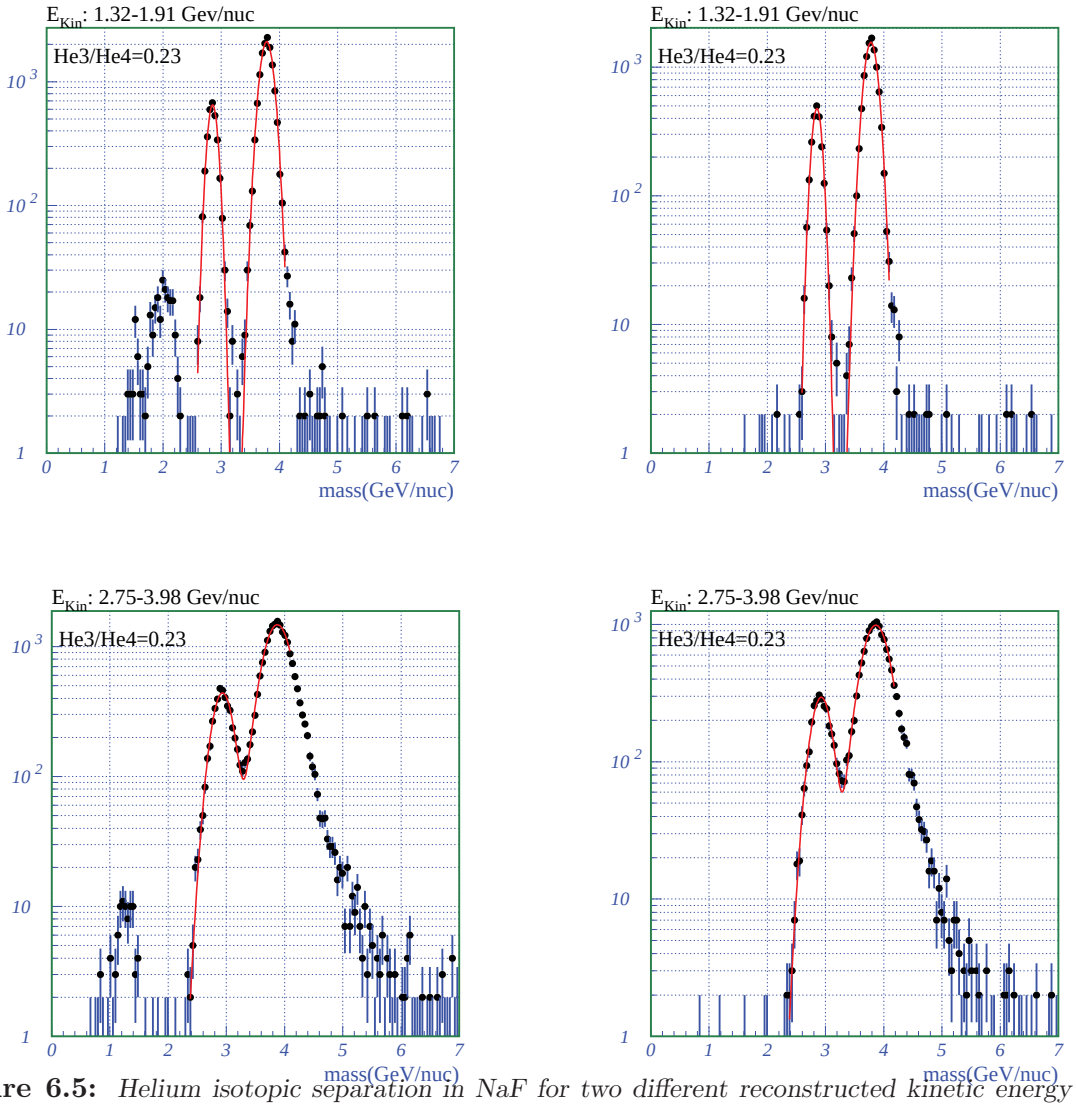

Figure 6.5: *Helium isotopic separation in NaF for two different reconstructed kinetic energy ranges: with foil, 1 mm thick,* (left) *and without foil* (right).

Figure 6.6 shows the corresponding distributions for the aerogel radiator. For aerogel, the background events are flatly distributed and suppressing the foil doesn't have a background reduction effect similar to the NaF case. This shows that the fake reconstructions aren't only due to the hits produced in the foil. This was expected since there is a limit for the maximum reconstructed Čerenkov angle established by our reconstruction method. This limit is 10% of the maximum expected value. For aerogel it corresponds to 15^o, a value below the minimal Čerenkov angle (27^o) hypothetically reconstructed with photons originating on foil, for particles just above

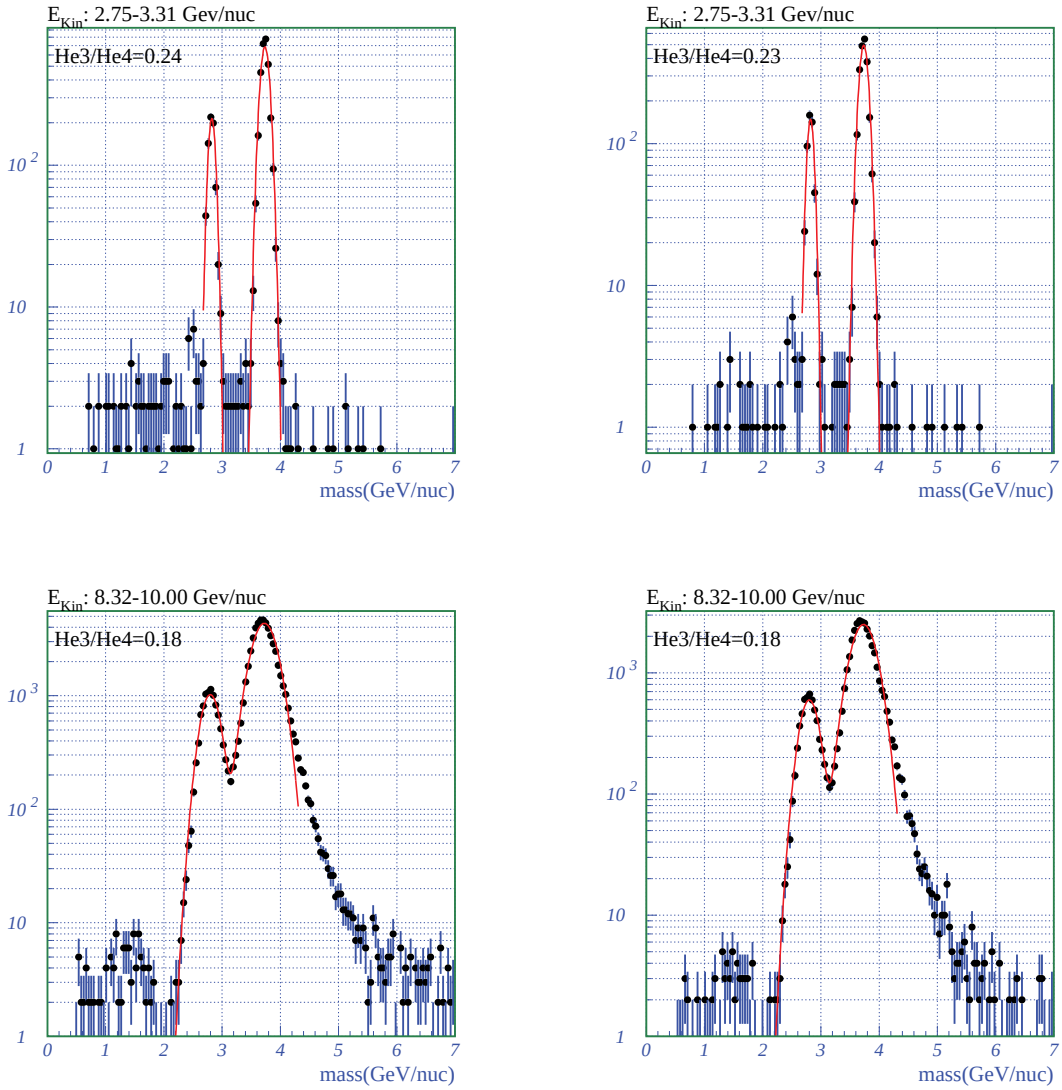

Figure 6.6: *Helium isotopic separation in Agl for two different reconstructed kinetic energy ranges: with foil, 1 mm thick,* (left) *and without foil* (right).

the aerogel threshold.

Observing events from that flat region, it is verified that they correspond to events from below the threshold. In this case noise hits are used to perform the reconstruction producing a fake reconstruction. An example is shown in Figure 6.7 where the event is reconstructed in aerogel with a Čerenkov angle θ_c^{rec}=11.4^o while the simulated energy T_{sim}=1.3 GeV/nucleon is below the kinetic energy threshold which is of 2.97 GeV/nucleon. The reconstructed kinetic energy is 5.84 GeV/nucleon. The

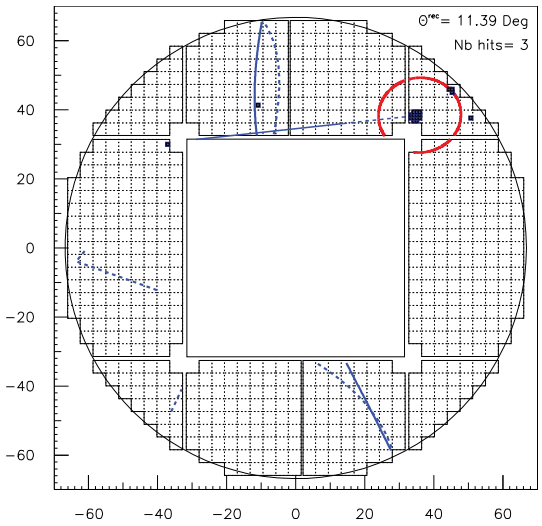

Figure 6.7: *Fake reconstruction as an aerogel event: the small pattern is the pattern reconstructed as generated in aerogel; the larger one is the foil reconstruction.*

same particle, crossing the plastic foil, generated a larger Čerenkov photon pattern with an expected Čerenkov angle, θ_c^{sim} of 42.3^o, distinct from the pattern reconstructed as generated in aerogel.

In order to get rid of the fake reconstructions different procedures can be applied:

- exclusion of the RICH recontructions based on clustered hits;
- comparison of the velocity measurements made on the RICH and TOF;
- comparison of the reconstructed event signal with the predicted one, using an external to RICH charge measurement (Tracker or TOF).

6.4.2 ^{10}Be/^{9}Be separation

Figure 6.8 shows the beryllium mass reconstructions for events passing through the NaF radiator, for different kinetic energy ranges, with foil and without foil. In the presence of the foil there is also a peak of events below ^{9}Be coming from fake reconstructions made with detected hits from the plastic foil. This is the region

near the ^{7}Be that should be cleaned, avoiding contamination. Removing the foil the background events strongly reduce.

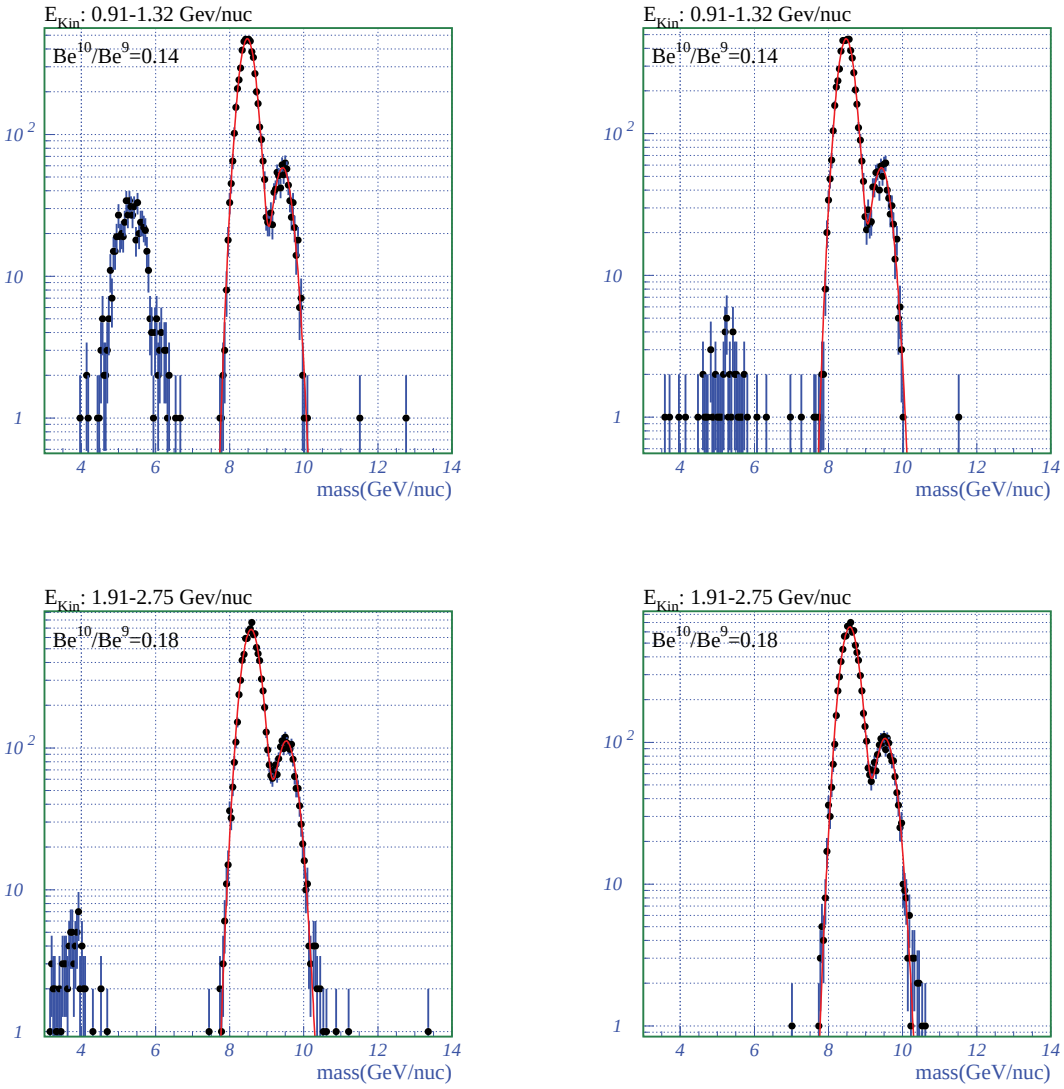

Figure 6.8: *Beryllium isotopic separation in NaF for two different reconstructed kinetic energy ranges: with foil,1 mm thick,* (left) *and without foil* (right).

Figure 6.9 presents the corresponding distributions for the aerogel radiator, for different kinetic energy ranges with and without foil. Here, like in the helium reconstructions in aerogel, the background events are flatly distributed and suppressing the foil doesn't eliminate the source of fake reconstructions. In this case, the fake reconstructions are also reconstructions with noise hits appearing in events below

the threshold. Eliminating reconstructions using clustered hits would reduce these background events in the mass reconstructions.

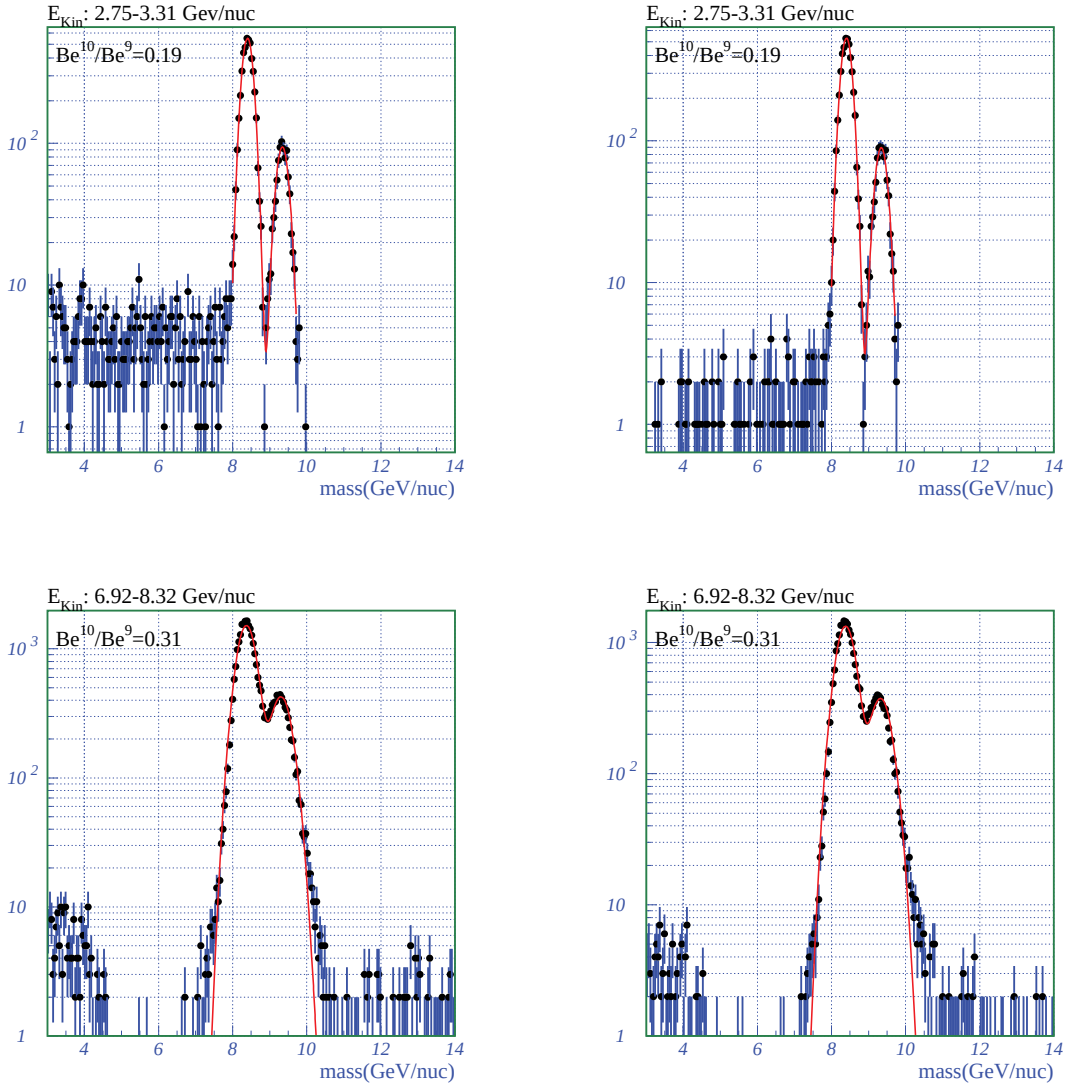

Figure 6.9: *Beryllium isotopic separation in Agl for two different reconstructed kinetic energy ranges: with foil,1 mm thick,* (left) *and without foil* (right).

6.5 Reconstructed Isotopic Ratios

Figure 6.10 represents the isotopic ratios obtained from the fits as function of the kinetic energy per nucleon for both family of isotopes, using a foil or suppressing it.

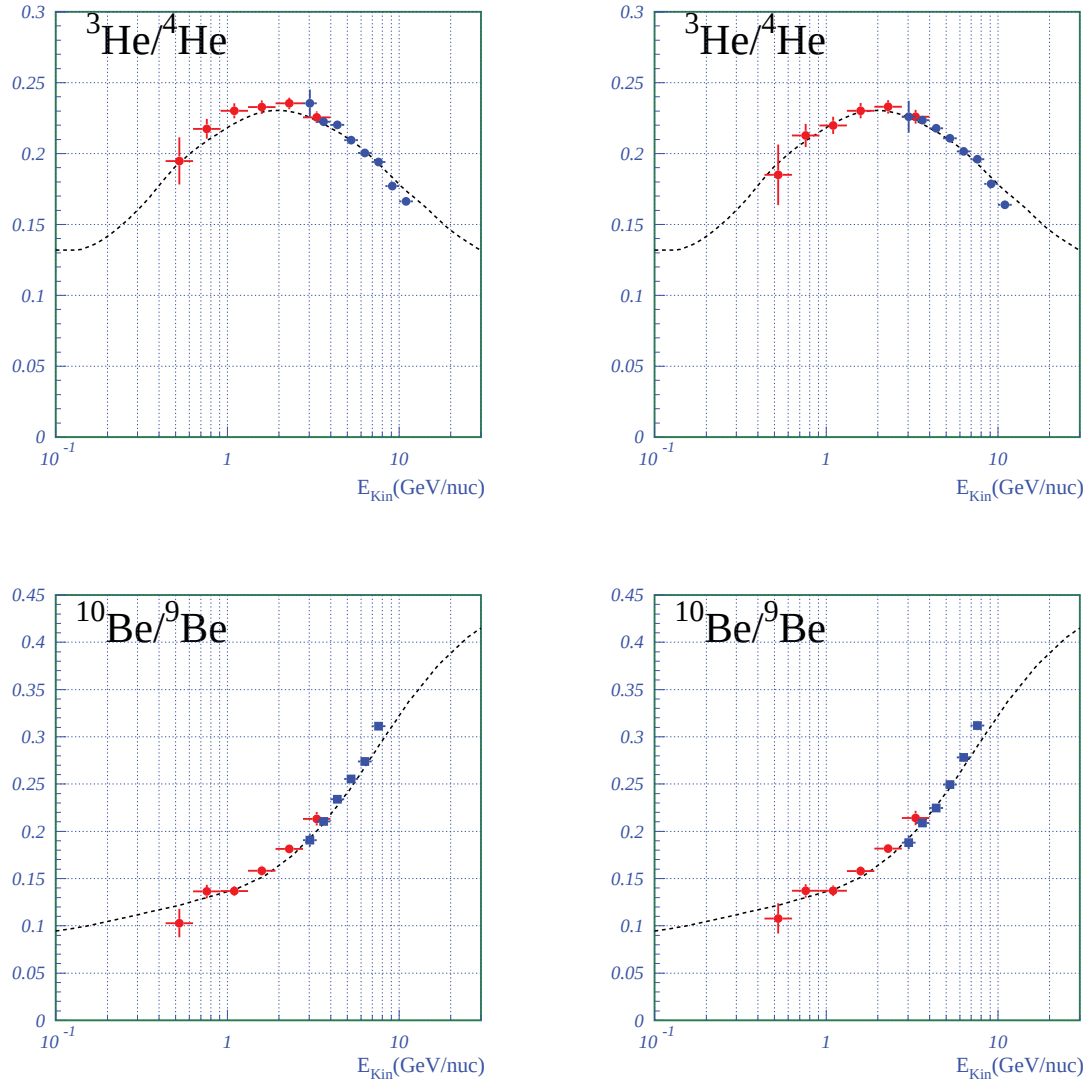

Figure 6.10: *Relative differences between expected and reconstructed isotopic ratios of helium* (top) *and beryllium* (bottom) *simulated events versus the kinetic energy per nucleon. With foil,1 mm thick*, (left) *and without foil* (right).

Isotopic ratios from events crossing the sodium fluoride are fairly measured up to the aerogel threshold, from 0.5 GeV/nucleon up to around 3.0 GeV/nucleon. From there on, the aerogel allows to measure the isotopic ratios up to around 10.0 GeV/nucleon in helium nuclei and up to around 8.30 Gev/nucleon in beryllium nuclei. Above these kinetic energy values the two peaks are mixed and the result of the mass fit doesn't provide us the correct ratio between the number of two

isotopes in both cases. The mass separation is better until larger values of energy in isotopes of lower Z, the helium case, than in higher Z nuclei since $\sigma_M \propto M$.

For helium nuclei the removal of the foil improves the agreement between the expected and reconstructed results in the NaF region. In Agl the effect is not notorious. In beryllium nuclei the removal of the foil doesn't provoke a notorious effect on the ratios.

The comparison between AMS isotopic ratios and the experiments before AMS-02 is done in Figure 6.11. As it was said in Chapter 5, AMS-02, with the velocity resolution provided by the RICH, and the tracker momentum resolution will allow to separate helium and beryllium in a more extended kinetic energy range than the previous experiments. The farther measure for helium ratios was performed by Webber and his group and is at a kinetic energy per nucleon of 6 GeV/nucleon. In the beryllium case the farther measure was done by ISOMAX, a balloon experiment, and it is at a kinetic energy per nucleon of 1.57 GeV/nucleon. In both cases measurements were based on rather poor statistics bringing large uncertainties to the isotopic ratio measurements, specially in berylliums.

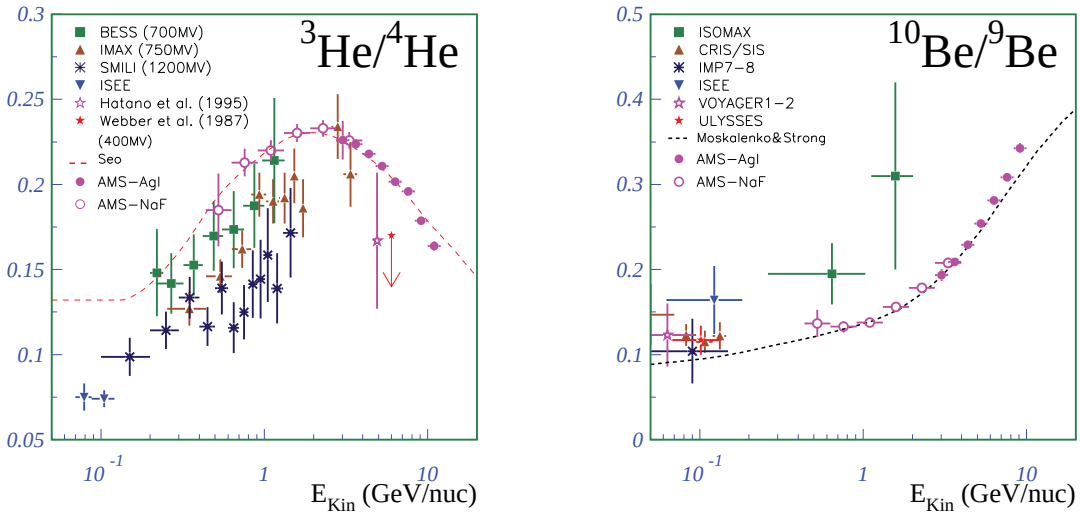

Figure 6.11: *Comparison between AMS isotopic ratios for helium* (left) *and beryllium* (right) *and other previous experiments. Reconstruction in the absence of the plastic foil.*

If AMS-02 wasn't equipped with the RICH detector a mass separation could still be done using the TOF's velocity measurement. However, due to the lim-

ited velocity resolution (∼3%) it would separate helium isotopes only up to around 0.8 GeV/nucleon and it would be hard to separate beryllium isotopes.

6.6 Conclusions

A dual radiator configuration for the RICH detector, made of sodium fluoride (NaF) and aerogel (Agl) allows a wider range of kinetic energy values to do the helium and beryllium isotopic separation. This is extended down to values of 0.5 GeV/nucleon (NaF threshold energy) up to around 8 GeV/nucleon in beryllium nuclei and up to around 10 GeV/nucleon in helium nuclei.

The presence of an acrylic plastic foil with a refractive index of 1.49, 1 mm thick affects the NaF reconstructions mainly at energy values around the threshold in both elements. In aerogel bad mass reconstructions can't be so easily discriminated as being from foil, as it happens in NaF. There is a flat contamination mainly due to reconstructions done with noise hits in energy values below the aerogel threshold.

Before advancing with a drastic measure of removing the foil, whose presence seems to be a wise choice from the mechanical point of view, there are some tools to explore. There could be analyzed the accordance between the charge measured by the TOF or tracker and the reconstructed mass. The reconstructions using clustered hits could be eliminated. The velocity measurements made with ToF and RICH can be compared. The foil thickness can also be reduced but assuring the mechanical stability of the radiator.

Conclusion

AMS is a high energy particle detector developed to measure cosmic ray fluxes outside the Earth's atmosphere. It will be installed on the International Space Station and will stay there collecting data for at least 3 years. The instrument will be equipped with a proximity focusing RICH detector.

In this thesis it was calculated the geometrical acceptance of the Čerenkov pattern of each portion in the different elements of the detector (radiator, mirror, photomultipliers matrix). This is essential for the determination of the electric charge of the cosmic particles and also to correct inefficient regions of the detector.

Based on these acceptance calculations it was studied a new configuration for the RICH radiator. It points to a main radiator of a low refractive index: aerogel 1.03, 3 cm thick replaced at the center by a square of sodium fluoride, with 34 cm of side length and 0.5 cm of thickness. Such configuration not only increases the RICH acceptance but also extends the linear momentum covered by the detector to lower values 0.5 GeV/nucleon up to around 8 GeV/nucleon in beryllium nuclei and up to around 10 GeV/nucleon in helium nuclei.

It allows to introduce more constraints on the cosmic rays propagation models based on a measurement of the ratios $^{3}He/^{4}He$ and $^{10}Be/^{9}Be$.

Bibliography

[1] S. M. Ting. The Alpha Magnetic Spectrometer, A Particle Physics Experiment on the International Space Station, May 1998.

[2] AMS Collaboration. The Alpha Magnetic Spectrometer (AMS) on the International Space Station: Part I - results from the test flight on the space shuttle. *Physics Reports*, (366):331–405, 2002.

[3] Krane. *Introductory Nuclear Physics*. John Wiley, 1988.

[4] V.S. Berezinskii et al. *Astrophysics of Cosmic Rays*. North Holland, Amsterdam, 1990.

[5] J. Borges. Velocity Reconstruction with the RICH detector of the AMS experiment. Master's thesis, Instituto Superior Técnico, March 2003.

[6] A. Keating. Reconstrução da carga eléctrica de partículas cósmicas no detector RICH da experiencia AMS. Master's thesis, Instituto Superior Técnico, May 2002.

[7] Gaisser. *Cosmic Rays and Particle Physics*. Cambridge University Press, 1^{st} edition, 1990.

[8] Particle Data Group. Particle Physics Booklet, 2002.

[9] H.V. Klapdor-Kleingrothaus et al. *Particle Astrophysics*. Institute of Physics Publishing, 1997.

[10] I. Usoskin et al. Heliospheric Physics and Cosmic Rays. Lecture Notes, Fall term 2000, January 2001.

[11] M. Cristinziani. *Search for Heavy Antimatter and Energetic Photons in Cosmic Rays with the AMS-01 Detector in Space*. PhD thesis, Faculté des Sciences de l'Université de Genève, 2002.

[12] F. Barão. Results from the AMS precursor flight and prospects of AMS2. Presentation at Third International Workshop on New Worlds in Astroparticle Physics, September.

[13] V.S. Ptuskin. Cosmic Rays: Origin, Propagation, and Interaction. In *Third International Workshop on New Worlds in Astroparticle Physics*, pages 46–65. World Scientific, 2000.

[14] V.L. Ginzburg and S.I. Syrovatskii. *The Origin of Cosmic Rays*. Pergamon Press, 1964.

[15] D.C. Jones F.C., Ellison. The Plasma Physics of Shock Acceleration. *Space Science Rev.*, 58:pp. 259–346, 1991.

[16] V.L. Ginzburg. On the origin of cosmic rays: some problems of high-energy astrophysics. *Rev. Mod. Phys.*, 48:161–189, 1976.

[17] V.S. Ptuskin and A. Soutoul. Cosmic-Ray Clocks. *Space Science Reviews*, 86:225–238, 1998.

[18] D. Casadei. Esperimento AMS: problemi teorici e sperimentali nella ricerca di antimateria in raggi cosmici. Master's thesis, Univ. di Bologna, March 1998.

[19] L.J. Gleeson and W.I. Axford. Solar modulation for galactic cosmic rays. *ApJ*, 168:1011–1026, December 1968.

[20] http://www.ngdc.nasa.gov/seg/potfld/geomag.stml.

[21] M. Walt. *Introduction to Geomagnetically Trapped Radiation*. Cambridge University Press, 1^{st} edition, November 1994.

[22] A.G. Cohen et al. A Matter-Antimatter Universe. *ApJ*, 495:539–549, March 1998.

[23] E.A. Bogomolov et al. In *Proc. 16th Int. Cosmic Ray Conf.(Kyoto)*, volume 330, 1979.

[24] A. Buffington et al. A Mesurement of the Cosmic-Ray Antiproton Flux and a Search for Antihelium. *ApJ*, 248, September 1981.

[25] F.W. Stecker et al. In *Proc. 17th Int. Cosmic Ray Conf. (Paris)*, volume 9, page 211, 1981.

[26] F.W. Stecker and A.W. Wolfendale. *Nature*, 309:37, 1984.

[27] J. Silk. Cosmic-Ray Antiprotons as a Probe of a Photino-Dominated Universe. *Phys. Rev. Lett.*, 53(6):624–628, August 1984.

[28] Th. Kirn. Antimatter & Dark Matter Search. Trento meeting, November 2001.

[29] BESS Collaboration. Measurement of Low-Energy Cosmic-Ray Antiprotons at Solar Minimum. *Phys. Rev. Lett.*, 81:4052–4055, 1998.

[30] BESS Collaboration. Precision Measurement of Cosmic-Ray Antiproton Spectrum. *Phys. Rev. Lett.*, 84:1078–1081, 2000.

[31] BESS Collaboration. Precision Measurement of Cosmic-Ray Proton and Helium Spectra with the BESS Spectrometer. *ApJ*, 545:135, 2000.

[32] J.W. Bieber. Antiprotons at Solar Maximum. *Phys. Rev. Lett.*, 83(4):674–677, July 1999.

[33] S.C. Kappadath. *Measurement of the cosmic diffuse gamma-ray spectrum from 800 KeV to 30 MeV*. PhD thesis, University of New Hampshire, 1998.

[34] P. Sreekumar. EGRET Observations of the Extragalactic Gamma-Ray Emission. *ApJ*, 494:523–534, February 1998.

[35] Chong-Ming Xu. *Phys. Lett*, 15:232, 1999.

[36] Yu V. Galaktionov. Antimatter in cosmic rays. In *Reports on Progress in Physics*, volume 65, page 1258. Institute of Physics Publishing, August 2002.

[37] M. Aguilar et al (AMS Collaboration). *Phys. Rep*, 366:331–404, 2002.

[38] M. Buénerd. AMS, a particle spectrometer in space. In *XXIV Symposium on Nuclear Physics*, Tasco, Mexico, January 2001.

[39] R. Battiston. Astro Particle Physics with AMS on the International Space Station. *Nuc. Phys. B (Proc. Suppl.)*, (113):9–17, 2002.

[40] J. Varela. *O Século dos Quanta*. Gradiva, 1st edition, Novembro 1996.

[41] L. Mosca. An Introduction to the direct detection of particle Dark Matter (WIMPS). In *Third International Workshop on New Worlds in Astroparticle Physics*, pages 189–200. World Scientific, 2000.

[42] N. Bahcall. Dark Matter. preprint Princeton Observ-P-693, November 1996.

[43] Alcaraz J. et al. AMS collaboration. Leptons in Near Earth Orbit. *Phys. Lett.B*, 484:10–22, June 2000.

[44] M. Huang et al. New results from AMS cosmic ray measurements. In *Proceedings of The First NCTS Workshop on Astroparticle Physics, Kenting, Taiwan*. World Scientific Pub., December 2001.

[45] F. Donato. Antideuterons as a Signature of Supersymmetric Dark Matter. *Phys. Rev. D*, 62, April 2000.

[46] http://ams.cern.ch/ams/ams homepage.html.

[47] Th. Siedenburg et al. A Transition Radiation Detector for AMS. *Nuc. Phys. B (Proc. Suppl.)*, (113):154–158, 2002.

[48] D. Casadei et al. The AMS-02 Time of Flight System. *Nuc. Phys. B (Proc. Suppl.)*, (113):133–138, 2002.

[49] B. Blau et al. The Superconducting Magnet of AMS-02. *Nuc. Phys. B (Proc. Suppl.)*, (113):125–132, 2002.

[50] W.J. Burger. The AMS Silicon Tracker. *Nuc. Phys. B (Proc. Suppl.)*, (113):139–146, 2002.

[51] F. Cadous et al. The AMS-02 electromagnetic calorimeter. *Nuc. Phys. B (Proc. Suppl.)*, (113):159–165, 2002.

[52] M. Buénerd. The RICH counter of the AMS experiment. In *Fourth Workshop on RICH Detectors, Pylos*, 2002.

[53] M. Boezio. *Positrons and Electrons in the Cosmic Radiation Measured by the CAPRICE94 Experiment*. PhD thesis, Kungl Tekniska Högskolan, 1998.

[54] M. Buénerd. The RICH counter of the AMS experiment. *Nucl.Instrum.Meth.A*, 350:158–162, 2003.

[55] Hamamatsu photonics (http://www.hamamatsu.com).

[56] http://wwwae.ciemat.es/∼delgadom/richsim/.

[57] S.P. Ahlen et al. Measurement of the Isotopic Composition of Cosmic-Ray Helium, Lithium, Berylium, and Boron up to 170 MeV per Atomic Mass Unit. *ApJ.*, 534:757–769, May 2000.

[58] G.A. de Nolfo et al. A measurement of the ^{10}Be/^{9}Be ratio above 1.0 GeV/nucleon: Results from the 1998 flight of ISOMAX. In *Proceedings of ICRC 2001*, 2001.

[59] M. Garcia-Munoz. The age of the Galactic Cosmic Rays derived from the abundance of ^{10}Be. *ApJ.*, 217:859, November 1977.

[60] A. Lukasiak. The Isotopic Composition of Cosmic-Ray Beryllium and its implication for the Cosmic Rays's age. *ApJ*, 423:426–431, March 1994.

[61] M.E. Wiedenbeck. A Cosmic-Ray Age based on the abundance of ^{10}Be. *ApJ*, 239:L139–L142, August 1980.

[62] J. J. Connell. Galactic Cosmic-Ray confinement time: *Ulysses* high energy telescope measurements of the secondary radionuclide ^{10}Be. *ApJ*, 501:L59–L62, July 1998.

[63] W.R. Binns. In *26th ICRC (Salt Lake City)*, 1999.

[64] A.W. Strong and I.V. Moskalenko. Propagation of Cosmic-Ray Nucleons in the Galaxy. *ApJ*, 509:212–228, December 1998.

[65] N.E. Yanasak. Measurement of the Secondary Radionuclides ^{10}Be, ^{26}Al, ^{36}Cl, ^{54}Mn, and ^{14}C and implications for the Galactic Cosmic-Ray Age. *ApJ*, 563:768–792, December 2001.

[66] A. Lukasiak et al. In *Proceedings of 25th ICRC 1997*, page 389, 1997.

[67] W.R. Webber. A Measurement of the Energy Spectra and relative abundance of the Cosmic-Ray H and He Isotopes over a broad energy range. *ApJ*, 275:391–404, December 1983.

[68] J.Z. Wang. Measurement of Cosmic-Ray Hydrogen and Helium and their Isotopic Composition with the BESS Experiment. *ApJ*, 564:244–259, January 2002.

[69] O. Reimer. The Cosmic-Ray ^{3}He/^{4}He ratio from 200 MeV per nucleon to 3.7 GeV per nucleon. *ApJ*, 496:490–502, 1998.

[70] J.J. Beatty. The Cosmic-Ray ^{3}He/^{4}He ratio from 100 to 1600 MeV amu^{-1}. *ApJ*, 413:268–280, August 1993.

[71] R. Kroger. Measurements of Hydrogen and Helium Isotopes in Galactic Cosmic Rays from 1978 through 1984. *ApJ*, 303, April 1986.

[72] Y. Hatano. Relative abundance of ^{3}He and ^{4}He in cosmic rays near 10 GV. *Phys. Rev. D*, 52(11):6219–6223, December 1995.

[73] W.R. Webber. A Reeaxamination of the Cosmic-Ray Helium Spectrum and the ^{3}He/^{4}He Ratio at High Energies. *ApJ*, 312:178–182, January 1987.

[74] E.S. Seo. Stochastic Reacceleration of Cosmic Rays in the Interstellar Medium. *ApJ*, 431, August 1994.

[75] M. Buénerd. Note on the radiator configuration for the RICH of AMS. *AMS internal note*, May 2000.